Monitoring and Measurements with the ATLAS Inner Detector and Search for Supersymmetry using ATLAS data

Konstantinos A. Kastanas

Dissertation for the degree philosophiae doctor (PhD)

at the University of Bergen

2014

Dissertation date: 12.12.2014

Abstract

This thesis was completed in the ATLAS experiment at the Large Hadron Collider at CERN. The work presented here spans from detector monitoring to the early collision physics and finally to the analysis of 7 TeV collisions data in search for New Physics. Three main topics are presented in the thesis. The first one is the monitoring and data quality of the ATLAS Inner Detector. The measurements of charged particle spectra in p-p collisions with energies of 900 GeV, 2.36 TeV and 7 TeV are shown in Paper I attached in the thesis and the cross-check that was carried out on the analysis 7 TeV dataset is presented. A search for Supersymmetric events in the 7 TeV data is presented and the results are summarised in Paper II attached in the thesis.

Acknowledgements

First of all I want to thank my supervisors Anna Lipniacka, Heidi Sandaker and Pippa Wells. You have been very helpful during the course of this PhD and above all patient. My biggest thanks for everything I have learnt from you over the years.

Thanks to all of my coworkers in the Inner Detector and the Data Quality groups. In particular I would like to thank Gaetano Barone and Per Johansson for working with me on the monitoring even long after they had to. My thanks to Steve McMahon, Saverio D'Auria and Dave Robinson for their input and useful discussions. And of course all the great people I met in the 007 office at CERN, it was a pleasure sharing an office with you all.

Thanks to the Bergen group for giving me a good environment to work in. I am grateful to Wolfgang Liebig and Therese Sjursen in particular for reading this thesis and providing valuable input. I also want to thank Ørjan for being good company over skype during the days and nights of finalising the SUSY analysis.

Many thanks to Prafula Behera and Remi Zaidan, who introduced me to Minimum Bias physics. It was great working with you and I learned a lot.

I would like to mention Kostas, Christos, Eleni, Thodoros and Fanouria; it would not have been the same without you there. And a big thanks to Kostas for his philosophical advice, even if I did not always follow it.

Many thanks to Øystein and Therese for being around this entire process. You have always made things interesting and kept me going. My friends outside of physics, particularly Nina, Sebastian, Fedon and Filippas; thank you for being there for me even though you were far away and for often giving me the perspective I needed.

My family, whether in Iceland, Athens or Chalkidona, I am grateful for your constant support and enouragement. Last but not least my deepest gratitude to Alicia for her support and love, this would not have been possible without you. This PhD has to a large extent defined our life so far, now it is time for new adventures.

Contents

Chapter 1

Introduction

The Large Hadron Collider (LHC) is a state of the art proton-proton collider built at CERN. It has a 27 km circumference and is designed to reach Center of Mass (CoM) energies of 14 TeV. This is the highest energy ever achieved in a collider, and by analysing the output of its collisions the physics at these high energies can be studied. To this end there are four major experiments at the LHC, built to record the particles produced in collision at the LHC. These experiments are ATLAS, ALICE, CMS and LHCb; I participated in the ATLAS experiment.

The physics investigated covers many different areas. The most important goal for the ATLAS experiment was to find the Higgs particle, the discovery of the Higgs particle was indeed announced by both ATLAS and CMS on July 4th 2012. In addition, searching for physics beyond the Standard Model (SM), such as supersymmetry, is an important topic. The detector is also suited for doing more refined measurements of SM properties, taking advantage of the very high event output of the LHC, as well as probing SM physics at the higher energy of the LHC.

I had the privilege of doing my PhD during the time when the first LHC run took place, starting in 2009 and ending in 2013. This allowed me to participate in the detector commissioning for collisions, the start of the run, as well as the gradual improvements in the understanding of the detector and the machine.

During the entire run I worked on the Inner Detector Global monitoring, a monitoring package responsible for assessing the status and performance of the ATLAS Inner Detector as a whole. Throughout this I worked closely with the ATLAS Inner Detector and Data Quality communities, which was greatly aided by being stationed at CERN as a Technical PhD Fellow. In the years 2009-2014 I was responsible for the Inner Detector Global Monitoring package as well as day-to-day operations; assessing the quality of data as well as maintaining the system for running the monitoring package during data-taking.

I got the opportunity to participate in the 7 TeV minimum bias analysis in 2010. This analysis produced the first 7 TeV minimum bias result for ATLAS and combined them with the results from the analysis of the 900 GeV and 2.36 TeV data collected in the first months of operation in 2009. In this paper I was responsible for the cross-check analysis performed on the 7 TeV dataset, leading to the same distributions as those published. This was very interesting as it was the first chance to see how the work on monitoring comes into play in a physics analysis and getting a better understanding of the impact of tracking on physics analyses. The work on this is published in Paper I included in the thesis, entitled "Charged-particle multiplicities in pp interactions measured with the ATLAS detector at the LHC".

Paper II, entitled "Search for supersymmetry in events with large missing transverse momentum, jets, and at least one tau lepton in 7 TeV proton-proton collision data with the ATLAS detector", presents a search for supersymmetric events in the 7 TeV data collected in 2011 with tau leptons as a signature. Supersymmetry is an extension of the Standard Model that predicts a relatively light Higgs boson and solves the so called hierarchy problem, stabilizing the Higgs boson mass. There are also good Dark Matter candidates among supersymmetric particles. In many supersymmetric models a partner of the tau lepton, the stau, is the so called Next to Lightest Supersymmeric Particle (NLSP). This leads to tau lepton signatures in the detector. My role in Paper II was to develop methods to estimate backgrounds from W and top production. In addition, I have been responsible for large parts of the developement of the framework used for the analysis. The framework relies on so called "skims and slims", to produce subsets of interests from the ATLAS data with preselected information which is important for the analysis. I have continued my active analysis support also for the analysis based on 8 TeV data from 2012, which resulted in a conference note [1] and a paper [2].

I got the opportunity to present results on behalf of ATLAS, including my work, on two occasions, once at the *2nd International Workshop on Multiple Partonic Interactions at the LHC* in Glasgow with a talk titled "Minimum bias measurements at ATLAS" and in the *First Large Hadron Collider Physics Conference* in Barcelona with a talk titled "Inclusive searches for squarks and gluinos with the ATLAS detector".

Chapter 2

LHC and ATLAS

The work presented in this thesis has been performed at the ATLAS detector situated at the Large Hadron Collider (LHC), both presented in this chapter. This chapter discusses the relevant accelerator parameters as well as ATLAS detector technologies, operation, data taking and reconstruction of physics objects and quantities used in the analysis. This forms the background needed for the work presented in the following chapters. All ATLAS information in this chapter is based on the ATLAS detector reference paper [3], unless otherwise stated.

2.1 LHC

The LHC [4] is a new collider built at CERN. It is a proton-proton collider nominally operating at a 14 TeV CoM energy. It is built within the old Large Electron Positron Collider (LEP) tunnel and has a 27 km circumference, see figure 2.1. The entire collider is operated with superconducting magnets, which are cooled down to 1.9 K to keep the dipoles superconducting and providing the necessary 8.3 T field to bend the protons.

The accelerator has four interaction points, where collisions take place. There are the four main experiments of the LHC, ATLAS (Point 1), ALICE (Point 2), CMS (Point 5) and LHCb (Point 8).

Luminosity is a very important collider parameter, allowing us to calculate expected event rates given a process cross-section. It can be approximated as

$$L = \frac{f \times N^2}{4\pi\sigma_x\sigma_y} \tag{2.1}$$

where f is the rotation frequency of particles in the beam, N is the number of particles and σ_x and σ_y are the spread of the beam in the directions orthogonal to the beam. Nominally the LHC could be filled with 2808 bunches

with a 25 ns bunch spacing between them, each containing 1.1×10^{11} protons, to reach a design luminosity of $10 \times 10^{34}\,\mathrm{cm}^{-2}\,\mathrm{s}^{-1}$. The resulting interaction rate at the detectors is about one billion collisions per second, putting a heavy strain on the detector readout and trigger systems. As the luminosity is very high and the bunch spacing is tight there is more than one interaction in each bunch crossing. These additional additional interactions are referred to as pileup. At such high luminosity and tight bunch spacing pileup becomes a significant problem.

The results presented in this thesis use data collected during the years 2011-2012. During this time the LHC underwent commissioning towards increasingly higher CoM energies and luminosity. The CoM energy was 7 TeV and 8 TeV in 2011 and 2012 respectively, with 1368 bunches at 50 ns spacing. The integrated luminosity and average number of interactions per bunch crossing for the 2011 and 2012 runs can be found in figure 2.2.

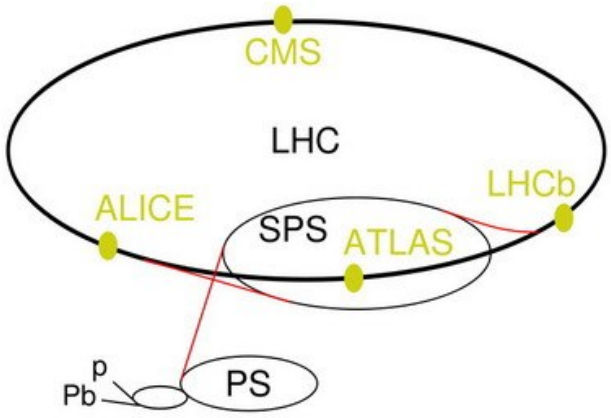

Figure 2.1: Overview of the LHC accelerator chain. The proton beam enters the LHC from the SPS with an energy of 450 GeV, with collisions happening at four interaction points around the ring, one for each of the main experiments; ATLAS, ALICE, CMS and LHCb. The interaction point where ATLAS is located is referred to as Point-1.

2.2 ATLAS

The ATLAS detector is a general purpose detector, situated in one of the four LHC interaction points, as indicated in figure 2.1. The detector is built with a broad physics programme in mind, ranging from searches for the Higgs boson and physics beyond the Standard Model to top physics and precision Standard Model measurements. It is a 44 m long and 25 m tall detector, built with three primary components: the Inner Detector (ID), the calorimeters

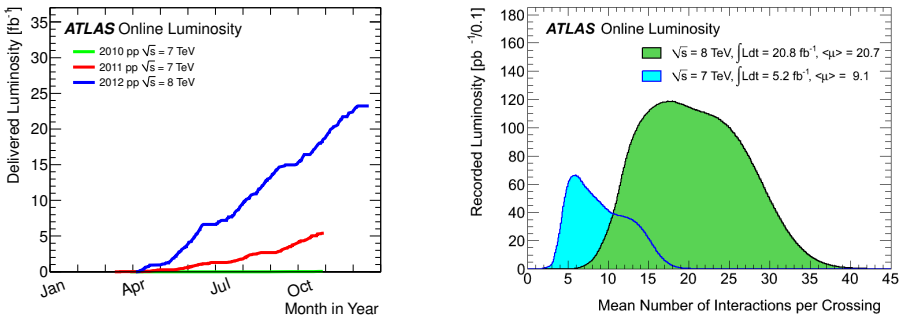

Figure 2.2: Total integrated luminosity delivered by the LHC as a function of time as measured by ATLAS (left) and average number of interactions per bunch crossing, weighted by luminosity (right) for the 2011 and 2012 runs.

and the Muon Spectrometer; the overall structure of the detector is shown in figure 2.3. All of these components are built for providing excellent hermiticity as well as giving reliable measurements of particle properties under the conditions of the LHC. These include very high event rates, large event multiplicities and a high radiation environment.

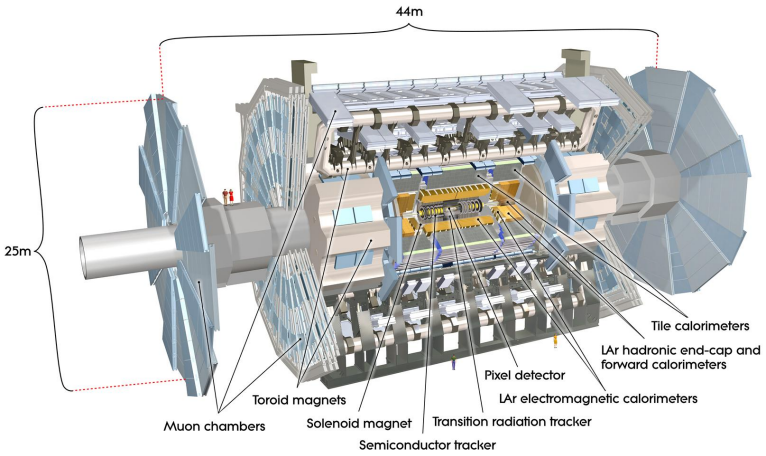

Figure 2.3: Overview of the ATLAS detector. Shown are the main detectors of ATLAS and the magnet system [5].

2.2.1 Coordinate system

The ATLAS coordinate system is oriented such that the x-axis points towards the center of the LHC ring and the y-axis points upwards. Thus the z-axis is along the beam pipe, pointing counter-clockwise. The azimuthal

angle ϕ is defined as $\phi = \arctan(y/x)$ and the polar angle, θ between the particle and the z-axis. Pseudorapidity is commonly used instead of θ, defined as $\eta = -\ln\tan\theta/2$. The transverse momentum of a particle is defined as $p_{\mathrm{T}} = \sqrt{p_{\mathrm{x}}^2 + p_{\mathrm{y}}^2}$. Angular distances between objects, denoted ΔR, are defined as: $\Delta R = \sqrt{\Delta\eta^2 + \Delta\phi^2}$

2.3 Inner Detector

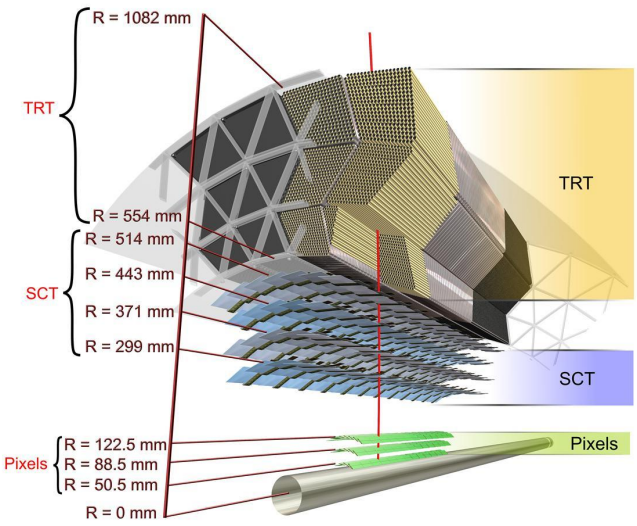

Figure 2.4: The ATLAS inner detector, showing a cutaway view of the barrel and end-caps. The Pixel detector is closest to the beampipe, followed by the SCT and the TRT. The dimensions of the entire ID are shown for perspective [5].

The ID is a tracking detector, comprised of three sub-detectors. These are two silicon detectors, the Pixel and the SemiConductor Tracker (SCT) and a straw tube detector, the Transition Radiation Tracker (TRT). An overview of the detector layout can be found in figure 2.4.

A solenoid magnet provides a 2 T magnetic field with the field aligned with the beampipe bending the tracks of charged particles in the x-y plane allowing for momentum measurements in the tracker, see figure 2.5.

An evaporative cooling system, using C_3F_8 as coolant, is used to keep the Pixel and SCT detectors at a $-7\,^{\circ}\mathrm{C}$ temperature. This ensures that the detector performance stays high even after irradiation. The TRT operates

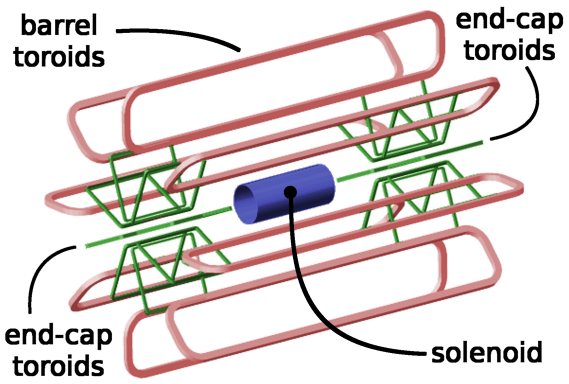

Figure 2.5: Overview of the ATLAS magnet systems, showing the solenoid, which provides the magnetic field to the ID and the toroid magnets providing magnetic field in the MS volume [6].

at room temperature, therefore heating pads are placed at the SCT-TRT boundary.

Pixel

The Pixel detector consists of three concentric cylindrical layers in the barrel and three disks for the endcap on each side with a total 1744 modules in the whole detector. The barrel and end-cap modules are identical, with nominal Pixel size of $50 \times 400\,\mu m^2$ and a sensor thickness of 250 µm. Each sensor has 46 080 independently read-out channels, resulting in more than 80 million readout channels for the whole detector. The Pixel sensors are built using an oxygenated n-type bulk material. One side is n^+ implanted where the sensors are placed. The detector is operated with a 150 V depletion voltage applied to the sensors. As charged particles traverse the sensor they produce electron-hole pairs that are then collected and read out as electric signal by the electronics. The position accuracy of the detector is 10 µm in the R-ϕ plane and 115 µm in the z direction (R in the endcap). The innermost layer of the Pixel detector is referred to as the b-layer and is very important for vertexing.

Semiconductor Tracker

The SCT is a silicon microstrip detector. It consists of four double sided concentric layers in the barrel and nine double-sided endcap disks on each side, with 15912 modules in total and more than six million readout channels. The sensors are made using a single sided p-in-n design with each sensor consisting of 768 strips with 12 cm length and 80 µm strip pitch. As charged particles traverse the detector they create electron-hole pairs that

are collected and read out by the electronics. The strips are aligned along the z-axis in the barrel and radially in the end-caps. In order to provide position information along the sensor strip direction the two modules in each layer have a stereo angle of 40 µrad, resulting in 580 µm accuracy along the strips. The detector is operated at 150 V bias voltage.

Transition Radiation Tracker

The TRT is a straw tube detector, placed outside the SCT. The detector is constructed from 4 mm diameter straw tubes with each tube made of two 35 µm layers, containing a gas mixture of 70% Xe, 27% CO_2 and 3% O_2. The straws are 144 cm long in the barrel. In order to cope with the high track multiplicities they are split in two sides, each side read out separately; this means there is no measurement of the z coordinate. In the end-caps the straws are arranged radially and are 39 cm long. As charged particles traverse the straws they create electron-ion pairs, that drift to the cathode and anode respectively. The detector records the position of charged passing particles by measuring the drift time of the electrons to the anode. The spatial accuracy for the drift radius is 130 µm. A distinction is made between low threshold minimum ionising particle hits and high threshold transition radiation hits. This is used to provide separation between pions and electrons. The TRT provides coverage for $|\eta| < 1.1$ in the barrel and $1.0 < |\eta| < 2.0$ in the end-cap. The total number of readout channels of the whole detector is 350 000.

The TRT provides an large number of additional hits from each straw, typically 36 per track. This significantly improves the transverse momentum resolution, by extending the lever arm for the measurement, while also enhancing the electron/pion separation via its coating that produces transition radiation for high p_{T} electrons.

2.4 Calorimeters

The ATLAS calorimetry system is built from five different sub-detectors, split into electromagnetic and hadronic calorimetry. Electromagnetic calorimetry is done using liquid argon as active material and lead as absorber. Behind the electromagnetic calorimeters are the hadronic calorimeters. In the barrel this is done by the tile calorimeter and in the end-caps by the Hadronic Endcap Calorimeter (HEC). At high pseudorapidities the Forward Calorimeter (fCal) provides both electromagnetic and hadronic calorimetry. In the barrel the cryostat houses the Liquid Argon Calorimeter (LAr) while in the end-caps the LAr, HEC and fCal share a common cryostat. An overview of the calorimetry system can be found in figure 2.6 and it is described as follows:

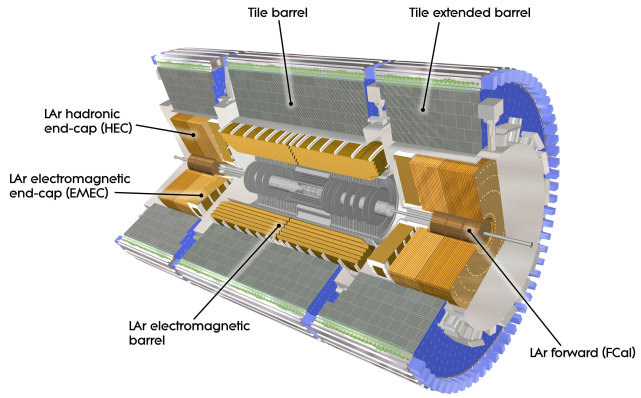

Figure 2.6: Overview of the ATLAS calorimeters [5].

Electromagnetic calorimetry

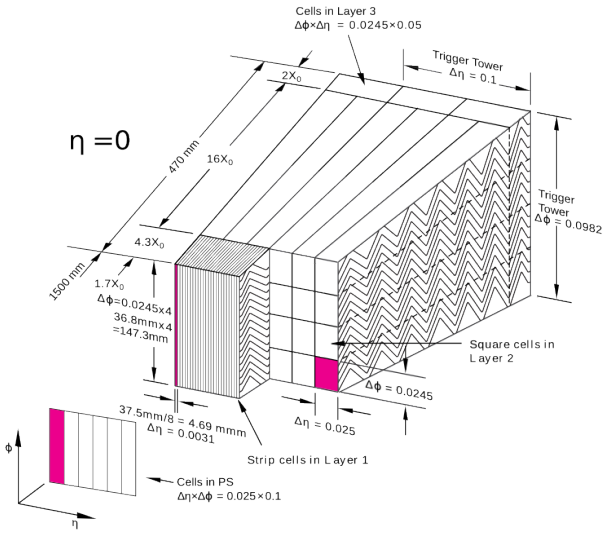

Figure 2.7: Structure of the ATLAS electromagnetic calorimeter, showing the accordion shape of the detector as well as the different layers and their granularity [5].

The ATLAS electromagnetic calorimeter is a sampling calorimeter using lead absorbers and liquid argon as the active material. A schematic view of the calorimeter can be seen in figure 2.7. The calorimeter is built using an accordion structure covering the $|\eta| < 2.5$ region in the barrel and $2.5 < |\eta| < 3.2$ in the end-caps. The detectors are segmented in three (two) regions in depth in the barrel (end-cap) with varying granularity in η. The first

layer is very finely segmented in η in order to provide accurate direction determination. Starting from the innermost, each layer provides 4.3, 16 and 2 radiation lengths respectively. The accordion ridges run along ϕ (R) in the barrel (end-cap). Between the absorbing layers there is an electrode mesh, consisting of three copper layers, the first and third layer at 2 kV potential and the second layer is used to read out the signal. This results in a 450 ns charge collection time. The energy resolution of the calorimeter can be parametrised as:

$$\frac{\sigma(E)}{E} = \frac{\mathrm{a}}{\sqrt{E\ (\mathrm{GeV})}} \oplus \mathrm{b} \tag{2.2}$$

where the stochastic term is $a = 10\% \cdot \sqrt{\mathrm{GeV}}$ and the constant term is $b = 0.17\%$.

Hadronic calorimetry

The hadronic calorimeter of ATLAS sits outside the LAr calorimeter and is used to provide measurement of energy for hadronically interacting particles that will punch through the LAr calorimeter. It is built from iron absorber tiles and plastic scintillator tiles covering the $|\eta| < 1.7$ region. The tiles are arranged azimuthally.

The detector is split into three layers. The layers are segmented into areas of $\Delta\phi \times \Delta\eta = 0.1 \times 0.1$ in the first two layers and $\Delta\phi \times \Delta\eta = 0.1 \times 0.2$ in the third layer. On average the active detector spans 8 interaction lengths.

As hadrons transverse the detector they interact with the iron tiles, initiating showers. As the resulting shower goes through the scintillating tiles ultraviolet light is emitted, which is collected at the edge of each scintillating tile through wavelength shifting fibers connected to PhotoMultiplier Tubes (PMTs) at the outer surface of the detector. The collected light is converted into electric signal and read out.

The relative resolution of the Tile calorimeter can be parametrised as in eq. 2.2 with parameters $\mathrm{a} = (56.4 \pm 0.4)\% \cdot \sqrt{\mathrm{GeV}}$ and $\mathrm{b} = (5.5 \pm 0.1)\%$.

In the end-caps, the HEC is used, which is a liquid argon calorimeter with copper plates as the absorber material, covering the $1.5 < |\eta| < 3.2$ region. The detector is built from two wheels with the innermost having 24 layers and the outer 16 layers. The absorbing copper layers are flat and a nominal voltage of 1.8 kV is applied between the absorbers and the electrodes.

Forward Calorimeters

In the forward region ($3.1 < |\eta| < 4.9$) the fCal is used to provide calorimetry for both electromagnetically and hadronically interacting particles. The detector uses liquid argon as the active material. It is further segmented into

three regions in depth, the one closest to the interaction point using copper as the absorber and specialising for electromagnetic calorimetry, with the next two using tungsten absorbers and meant to provide hadronic calorimetry and limit punch through to the muon systems.

Calorimeter calibration

The calorimeter response is different depending on the type of particle traversing it. In ATLAS two different calibration schemes are used:

Electro-Magnetic Energy Scale (EMES) is a calibration based on the calorimeter response to electrons and photons. This calibration was performed using test beam data. It is the baseline calibration applied to calorimeter clusters.

Jet Energy Scale (JES) is a calibration appropriate for Quantum Chromodynamics (QCD) jets. It is applied as a correction to the EMES calibration.

2.5 Muon spectrometer

The muon spectrometer makes up the largest part of the detector and is composed of four detector systems with two different purposes:

- Precision measurements
  - Monitored Drift Tubes (MDT) ($|\eta| < 2.7$)
  - Cathode Strip Chambers (CSC) ($2.0 < |\eta| < 2.7$, in the innermost layer)
- Triggering
  - Resistive Plate Chambers (RPC) ($|\eta| < 1.05$)
  - Thin Gap Chambers (TGC) ($1.05 < |\eta| < 2.4$)

MDTs are used for precision measurements throughout most of the detector, providing coverage for $|\eta| < 2.7$. These are 30 mm diameter drift tubes, filled with a 93%/7%Ar/CO_2 mixture under 3 bar pressure. At the center of the tube is a 50 µm thick tungsten-rhenium wire at a 3080 V potential difference compared to the tubes. The passage of muons triggers ionisation of the gas mixture and the readout of the resulting electrons at the wire.

CSCs are used for the innermost muon wheel, covering $2.0 < |\eta| < 2.7$, as they have very good granularity and timing resolution. The detector is a multi wire proportional chamber, with wires running in the radial direction at a 1900 V potential. Cathode strips run both parallel and perpendicular to the wires. Based on the charge collected at each strip it is possible to pinpoint the position of the track in both dimensions.

RPCs are built using electrode plates only, and no wires, with a 2 mm gap. A 4.9 kV mm^{-1} electric field leads to electron avalanches as muons pass between the plates.

TGCs are multi wire proportional chambers. Their defining feature is that the distance between the wires is larger than between the wire and the cathode. They have excellent timing resolution for the detector.

RPCs and TGCs are used for providing input to the Level one (L1) trigger, owing to their high readout speed, as well as additional hits for muon tracking.

An air-core superconducting toroid magnet provides magnetic field in the muon spectrometer volume, as indicated in figure 2.5. The magnet system consists of eight toroid coils in the barrel and two magnets in the endcaps built of eight coils, see figure 2.8. The coils in each endcap are housed inside a common cryostat. Due to the low number of coils building up the field there is considerable variation in the magnetic field, with values between 2 to 4 T m.

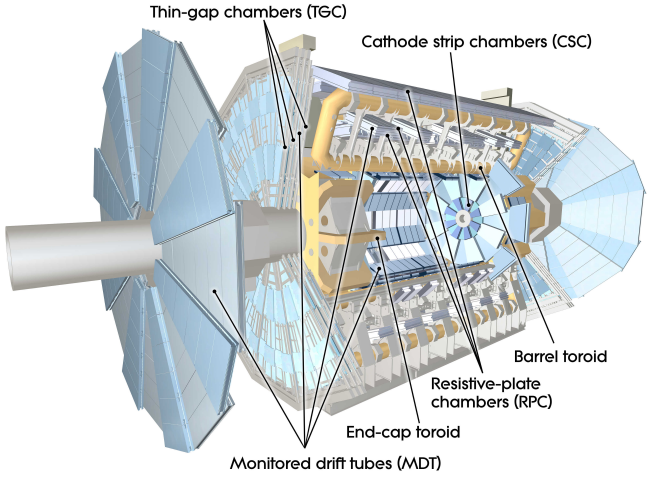

Figure 2.8: Overview of the ATLAS Muon Spectrometer. Shown are the MDTs and CSCs as well as the TGCs and RPCs. The barrel toroid magnets are also visible as are the end-cap magnets [5].

2.6 Reconstruction

Reconstruction is the process of going from the raw detector output to objects which are closer to the particles that were produced in the collision. In the ID and the MS the hits are combined to form tracks, recording the passage of charged particles. In the calorimeters, nearby energy deposits are combined to form clusters, representing possibly related energy deposits. From this point, they can be further combined to produce composite objects.

Tracks are the object of interest both in chapter 3 and 4 that follow. For the analysis presented in chapter 5 taus and jets are the main focus, as well as $E_{\mathrm{T}}^{\mathrm{miss}}$, which is very important in the characterisation of Supersymmetry (SUSY) events.

Below follows a brief summary of the physics objects reconstructed in ATLAS with focus on the most important ones for the work presented in the following chapters.

Tracks

Tracks are reconstructed particle trajectories using data from the ID and the muon spectrometer (for muon tracking). The following track parametrisation is used in ATLAS (see section 2.2.1 for coordinate system summary):

d_0 The transverse distance of the particle to a reference at the point of closest approach.

z_0 The longitudinal distance of the particle to a reference at the point of closest approach.

η The η direction of the particle.

ϕ_0 The ϕ direction of the particle.

p_{T} The transverse momentum of the particle.

Primary tracks, those originating from p-p interactions, are found using the so-called "inside-out" track reconstruction. This is the principal step in the track reconstruction and is seeded by hits in the Pixel and SCT. The track seeds are constructed by finding three hits in the Pixel and/or SCT that are compatible with a charged particle trajectory. These seeds are then propagated outwards through the Pixel and SCT detector using a Kalman filter to find compatible hits and update the track parameters at each layer of the detector. At this stage any ambiguities in the hit association to tracks are resolved and following this the track candidates are propagated to the TRT. Finally, the tracks are scored, in order to select the candidates that correspond most likely to primary charged particles. This procedure is done for tracks with momenta down to a certain minimal p_{T}threshold. This

threshold is typically set at 500 MeV but can go down to as little as 100 MeV for minimum bias event reconstruction.

For handling secondary charged particles, an additional tracking mode is in place using TRT hits as seeds to construct TRT-only tracks, these are then propagated inwards towards the interaction point adding extra Pixel and SCT hits to the track [7].

Finally, tracks are also built with Pixel hits alone. This is done in the very forward region, where Pixel alone provides coverage. These tracks are combined with muon hits to produce forward muons.

During the hit collection phase the tracking is aware of disabled modules in the detector, such that if a disabled module is passed by a track, the resulting missing hit is treated like a properly associated hit in the requirements applied during event reconstruction and physics analyses. On the other hand, active modules that did not add a hit to the trajectory count against the track hypothesis, and only a limited number of such occurrences is allowed per track. This allows the tracking to handle the large hit multiplicities in the detector, where fake tracks can easily arise from combinatorics. The exact quality requirements for a successful track fit and suppression of fakes depend on the luminosity, becoming tighter as the luminosity increases [8].

Vertexing and Beamspot

Vertex reconstruction uses primary tracks to determine the location of interaction and decay vertices in the event. This is made more difficult in the high-pile-up LHC environment, requiring many separated vertices to be found. For the LHC runs in 2011 and 2012 the mean number of interactions per bunch crossing (μ) was 9.1 and 20.7 respectively and the distribution of μ can be seen in figure 2.2.

Vertex reconstruction uses an iterative χ^2 fit of tracks to a common vertex. The z_0 parameter of the tracks is used to produce seeds, by combining nearby tracks, and then tracks are added and scored according to their contribution to the χ^2. Tracks that are more than $7\,\sigma$ away are taken out and used to seed a new vertex candidate [9].

The beamspot is reconstructed by taking the vertices found during reconstruction and fitting an ellipsoid to contain them. The determination is done in shorter time intervals of data taking, roughly ten minutes, letting the software track changes in beamspot position. When available, the beamspot is used as a three dimensional constraint on the vertex parameters. The procedure terminates when no more seeds are available [8].

Jets

Jets are reconstructed using the anti-k_T algorithm [10] where the distance parameter is set to 0.4. The calorimeter inputs to the jet reconstruction

are topological calorimeter clusters. Energy determination is done in two different ways. One scheme relies on cluster energy being evaluated with the EMES calibration with the JES correction factor applied [11] while the other method relies on a direct calibration of the cluster energy using a local calibration scheme. This correction factor is meant to correct for the different calorimeter response to hadrons compared to the electron beams that the EMES calibration is based on.

B-tagging Jets originating from b-quark hadronisation can be distinguished from jets originating from other quarks. This is due to the relatively long lifetime of b-hadrons. To identify these jets a secondary vertex is reconstructed from the charged tracks belonging to the jet.

In order to provide b-tagging, several algorithms are used in ATLAS. `IP3D` [12] which relies on the impact parameter of the tracks to identify b-jets. `SV0` [12] uses secondary vertex information to identify such decays. `JetCombNN` [13] does more sophisticated identification, exploiting the topology of the decays in the b-jet. Finally, the `MV1` [12] algorithm uses the output of all the above algorithms and combines them using a neural network, to produce one combined output from all of these, and thus achieving the highest discrimination power.

Taus

Tau leptons, due to their larger mass, can decay into a large variety of states. In all decays there is a tau-neutrino, an odd number of charged particles and possibly neutral mesons are produced. Classified by the type of the charged particles, the possible decay modes include decays through electrons or muons as well as hadronic decay modes. The goal of tau reconstruction is to be able to correctly reconstruct and identify hadronically decaying taus, since it is very hard to distinguish taus decaying through leptonic modes from primary electrons or muons.

The main challenge of identifying hadronic tau decays is that they are very similar to QCD jets. Hadronic decay modes include charged and neutral hadrons, primarily pions. The decay modes are split by the number of charged particles, most commonly one or three, referred to as one- and three-prong decays respectively. These charged hadrons are detected in the tracking and as hadronic energy. The neutral pions in the decay are seen as electromagnetic energy, as they promptly decay into photons. An example of a hadronic tau decay is shown in figure 2.9. The neutrino produced in tau decays escapes detection, which means that some information about the four-momentum of the original tau is lost. The combined four momentum of the hadronic decay products of the tau is referred to as the visible tau momentum ($p_{\mathrm{T}}^{\mathrm{vis}}$).

Hadronic tau reconstruction in ATLAS is seeded by jets coming from jet reconstruction, anti-k_T jets with radius $R = 0.4$ which satisfy the requirements $|\eta \leq 2.5|$, to be within the acceptance of the ID, and $|p_T| > 10\,\text{GeV}$. During tau reconstruction this region is further split into the core ($R < 0.2$) and the isolation annulus ($0.2 < R < 0.4$). As the decay products of taus are more collimated than QCD jets these two regions are used to differentiate hadronic tau decays from jets. These regions can be seen schematically in figure 2.9. Additionally, each of these jets is associated to a vertex where the tau is most likely to originate from.

The tau four-momentum is determined at this stage. First, the barycenter of the clusters that form the seed jet is calculated; the four-momentum of all clusters within $\Delta R < 0.2$ of this barycenter are then summed to form the tau four-momentum. The energy of the clusters in this last step is calibrated using the so-called Tau Energy Scale (TES) calibration schema, reflecting the particular mixture of electromagnetic and hadronic energy found in tau decays.

Once the tau four-momentum has been determined, tracks can be associated to the tau candidate. Tracks falling within the core cone are associated provided they satisfy the following criteria:

- $p_T \geq 1\,\text{GeV}$
- At least two Pixel hits
- At least seven Pixel and SCT hits
- $|d_0| \leq 1.0\,\text{mm}$
- $|z_0 \sin\theta| \leq 1.2\,\text{mm}$,

where the last two criteria are defined with the tau vertex as reference point. Tracks inside the isolation annulus are not associated to the tau candidate but are still used for producing discriminating variables for identification.

In order to identify taus, a number of variables are used to discriminate between taus and other objects (e.g. jets, electrons or muons). One important distinction comes from the number of tracks associated with the tau and three variables use this information during identification:

- Track radius, the p_T weighted angular distance of associated tracks and tracks in the isolation annulus to the tau axis (R_{track})
- Invariant mass of associated tracks, if more than one (m_{tracks})
- Fraction of total transverse momentum carried by the leading associated track (f_{track})

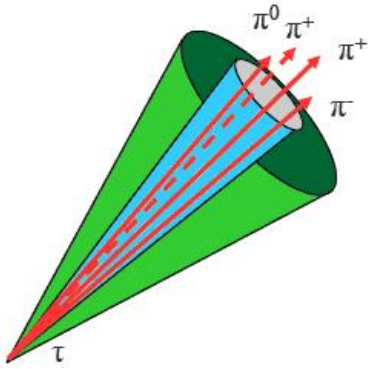

Figure 2.9: An example of a hadronic tau decay. The region within the inner cone is called the core and between the two cones is called the isolation annulus.

In addition to the lower track multiplicities of tau decays compared to jets, the energy deposits of taus are also more focused, compared to the larger spread of QCD jets. This gives rise to a second set of discrimination variables:

- Maximum ΔR (ΔR_{max}) between clusters
- Fraction of total energy carried by clusters in the core (f_{core})
- Number of tracks in isolation annulus ($N_{trk}^{0.2<R<0.4}$)

Finally, taus have a non-negligible lifetime of $(2.906 \pm 0.010) \times 10^{-13}$s [14], the following variables that depend on the flight distance are used to characterise tau candidates:

- Leading associated track Impact Parameter (IP) significance ($S_{leadtrack}$)
- Transverse flight path significance (S_T^{flight})

These are combined using multivariate techniques to produce the final discriminant. Three different identification discriminants are used; these are used for rejection of fakes originating from jets (the biggest contribution), electrons and muons (including electrons and muons originating from leptonic tau decays). Three selection types are provided, each presenting a different compromise of efficiency versus purity for the identified taus. These are referred to as the loose, medium and tight selections, each having progressively higher purity at the expense of lowered efficiency [15].

The analysis presented in chapter 5 uses the Boosted Desicion Tree (BDT) based method for identification. The following selection is applied:

- BDT based jet rejection (Tight selection)

- BDT based electron rejection (Tight selection)
- Muon veto

Missing E_{T}

The $E_{\mathrm{T}}^{\mathrm{miss}}$ observable is the momentum imbalance of the event in the transverse plane. It is reconstructed from calorimeter clusters and reconstructed muons.

In order to provide as accurate an energy measurement as possible the energy of each cluster is evaluated depending on the kind of physics object it is associated with, if any. When an association is possible the energy scaling of the appropriate object type is used. The full $E_{\mathrm{T}}^{\mathrm{miss}}$ is built from the following components [16]:

- Jets are taken into account and the JES is used to calibrate the energy of the associated clusters.
- Electrons are accounted for and the EMES is used for energy calibration.
- Taus are not given special treatment in the $E_{\mathrm{T}}^{\mathrm{miss}}$ calculation, their clusters are therefore treated as jets or electrons depending on how they are reconstructed.
- Muons are added in using muons reconstructed in the muon spectrometer alone. The reason for this is that the clusters of deposited energy in the calorimeters are already taken into account in the $E_{\mathrm{T}}^{\mathrm{miss}}$ reconstruction. Using standalone muons ensures that these are not double counted due to energy corrections.
- Calorimeter energy deposits around an identified muon are also added to account for the remaining muon momentum. In this case calorimeter cells are directly used to build up this contribution instead of clusters.
- The soft energy term covers all calorimeter clusters not otherwise associated with an object. They get added to the $E_{\mathrm{T}}^{\mathrm{miss}}$, with the EMES energy calibration.

Useful discrimination variables

A few variables are of particular importance in the work presented further, these are:

- The transverse mass, m_{T}, is defined between a lepton in the event and the $E_{\mathrm{T}}^{\mathrm{miss}}$:

$$m_{\mathrm{T}} = \sqrt{2(|E_{\mathrm{T}}^{\mathrm{miss}}||p_{\mathrm{T}}^{\tau}| - \vec{E}_{\mathrm{T}}^{\mathrm{miss}} \cdot \vec{p}_{\mathrm{T}}^{\tau})}$$

- The effective mass, m_{eff} is the scalar sum of the $E_{\text{T}}^{\text{miss}}$ and the transverse momenta of all jets and taus in the event

$$m_{\text{eff}} = \sum_i p_{\text{T}}^{\tau} + \sum_j p_{\text{T}}^{\text{jet}} + E_{\text{T}}^{\text{miss}}$$

- H_{T} is calculated as the scalar sum of the transverse momenta of selected jets and taus in the event

$$H_{\text{T}} = \sum_i p_{\text{T}}^{\tau} + \sum_j p_{\text{T}}^{\text{jet}}$$

These variables are useful for characterising events and are used particularly to discriminate between signal and background.

2.7 Trigger and DAQ

The trigger system is responsible for selecting events that are of interest for the physics programme of ATLAS. The computing time required to process those events and storage space to record them put stringent limits on the amount of events that can be stored offline for analysis. Additionally, while the event data is retrieved by the readout electronics there is dead time for the detector, no events can be recorded. Therefore it is important to select the most interesting events for readout. All the above issues are addressed by the trigger system.

The trigger system consists of three stages, each successively producing a more refined event selection with a lower output rate.

As collisions occur in the LHC the output of each detector is kept in memory on board the detector elements. This information is buffered there until a decision is received from the L1 trigger that the event should be read out. The L1 trigger uses information from the muon detectors to identify high p_{T} muons and calorimeter information to identify jets, electrons/photons, taus and events with large $E_{\text{T}}^{\text{miss}}$ or total transverse energy. In order to keep processing time within the small 2.5 µs latency window of the L1 trigger, reduced granularity information is used at the L1 stage. Furthermore, the calorimetry trigger is implemented in hardware in its entirety. After L1 selection the event rate is reduced down to 75 kHz. Events passing the L1 trigger are passed to the High Level Trigger (HLT).

The HLT is composed of two stages, the Level two (L2) trigger and the Event Filter (EF). Both use algorithms similar to those implemented in offline reconstruction and provide a more refined event selection, that further reduces the event rate.

The L2 trigger works on Regions Of Interest (ROI), defined by the features identified by the L1 trigger. Now the full granularity detector data in

this region as well as ID data are used, allowing for more refined reconstruction of the objects of interest. The L2 further pushes down the event rate to about 3.5 kHz.

Finally, in the EF the entire detector data is used at full granularity, producing the final decision on whether the event should be kept. Events selected at this stage are recorded for offline processing. The final event rate is about 200 kHz which is the maximum rate that can be handled by the offline computing resources. The overall structure of the triggering system of ATLAS can be seen in figure 2.10.

The events that are recorded in ATLAS are then split into streams. These streams classify events into sets with common characteristics. The streams typically used in data analysis are:

`JetTauEtmiss` which contains events passing triggers involving jets, taus or $E_{\mathrm{T}}^{\mathrm{miss}}$.

`Egamma` which contains events passing triggers involving electrons or photons.

`Muons` which contains events passing triggers involving muons.

`Express` which contains a mix of triggers intended for fast processing for the purposes of calibration and monitoring.

While the majority of events are only classified into one stream, it is possible for an event to satisfy the trigger requirements of more than one of the above categories, these streams are not exclusive. Additional streams are available for use in performance studies or more specialised analyses.

For the minimum bias study presented in chapter 4 the Minimum Bias Trigger Scintillator (MBTS) trigger is used (`L1_MBTS_1`), which requires at least one hit in one side of the scintillators. A looser trigger is used for tracking studies in the analysis, which triggers randomly on a filled bunch in the LHC.

For the SUSY analysis presented in chapter 5 the triggers used rely on jets and $E_{\mathrm{T}}^{\mathrm{miss}}$. The objects are selected in such a way that the analysis is limited to the trigger plateau. This is the region where the efficiency of the trigger is close to 100%. The cuts placed are on the primary jet p_{T} and the $E_{\mathrm{T}}^{\mathrm{miss}}$, at 130 GeV and 150 GeV respectively.

2.8 Offline processing

Events that are selected from the trigger are read out from the Data AQuisition (DAQ) system and are streamed to Tier-0 for storage and processing. The Tier-0 center is located at CERN and provides the computing capacity to promptly reconstruct the events coming out of ATLAS and the other

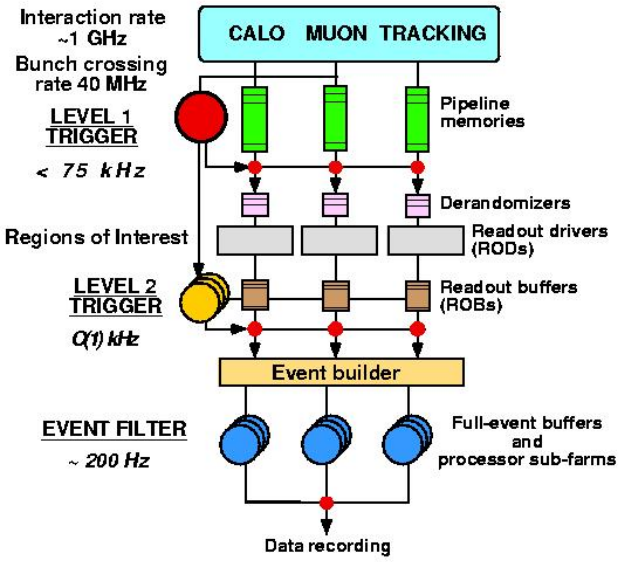

Figure 2.10: Overview of the ATLAS trigger system. Shown are the three trigger levels as well as the typical output rate. An overview of the readout system components at each level is also shown.

LHC experiments. Data taking in ATLAS is done in intervals known as Luminosity Blocks (LBs). These represent periods of stable running conditions from both the machine and the detector. During stable conditions a LB was switched every two minutes in the 2012 run.

The output of the offline processing is the Event Summary Data (ESD) format, which is the base format used for data analysis. These files contain the objects used in physics analysis. A second format, Analysis Object Data (AOD), is used as well, which contains the same information as the ESD but with fewer details, making for a smaller and more manageable set of information for physics analyses. These formats can be read in `ATHENA`. It is also common to convert these formats into flat `ROOT` [17] ntuples that can be used for `ROOT` based analyses, these are commonly referred to as D3PDs in ATLAS.

Chapter 3

ID Monitoring

In this chapter the ATLAS Inner Detector Global Monitoring is presented. It is a software package used to produce information to assess the Inner Detector performance and flag potential problems during data taking. The package is designed to provide a global overview of the performance of the three ID detectors combined and act as a bridge between the Data Quality (DQ) assessment of the ID sub-detectors and reconstructed objects that rely on tracking.

The overall structure of the monitoring and related processes can be seen in figure 3.1. These cover the production of the monitoring histograms as well as preparing the output used by the shifters to evaluate DQ.

The package runs after reconstruction, providing prompt feedback based on the data reconstructed. It is primarily used during data taking, including cosmic ray, p-p and p-Pb collisions. It is also used during reprocessing campaigns when all data taken is processed with a new release.

3.1 Software

All ATLAS monitoring packages based on `ATHENA` are implemented as a collection of `ATHENA` tools tied together by a manager. The packages are implemented in `C++` and the monitoring tools and manager are implemented as classes. The common ATLAS base classes for these are found in the `ManagedMonitoringBase ATHENA` package, which provides a consistent interface for all monitoring packages. The manager is responsible for setting up the monitoring tools and calling them for each event. The tools in turn initialise all histograms that are produced and retrieve the event and condition information needed to fill them. The base class for the monitoring tools defines methods for initialisation during the beginning of a run or the beginning of a Luminosity Block (LB), filling histograms as well as performing any necessary processing at the end of a run or LB. An overview of the structure of the ID global monitoring package in term of classes and their

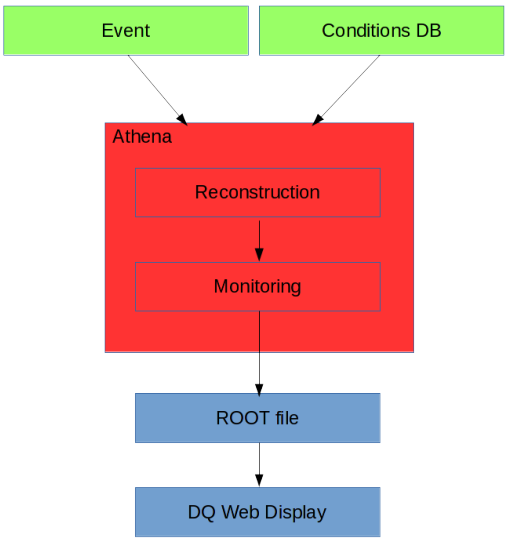

Figure 3.1: Functional diagram for the offline monitoring. Shown in green are the inputs, which are the event as well the detector conditions. In red is `ATHENA` which provides the framework for running reconstruction as well as monitoring. Finally, in blue, the output of the monitoring in `ROOT` format as well as the DQ Web Display which produces the web pages used by the DQ shifters.

inheritance structure can be found in figure 3.2.
The package consists of the following tools:

InDetGlobalHitsMonTool is responsible for retrieving the number of hits that make up each track and the number of dead modules traversed by the tracks. It can also check the distribution of holes on each track, which represents the number of detector elements crossed by the track without an associated measurement. This runs in the online environment to promptly spot issues but is disabled in offline running to reduce CPU time. These distributions are produced also as a function of the η-ϕ parameters of the track, to localise problems in the detector.

InDetGlobalTrackMonTool which produces distributions of the track parameters as well as the total number of tracks in each event. These distributions are produced for a number of track selections fulfilling different criteria in order to diagnose specific potential issues.

As there was much common code in the two tools described above, they were merged during the 2012 run in order to reduce CPU time and memory used by the monitoring.

InDetGlobalSynchMonTool checks the synchronisation of ID Read Out Drivers (RODs) as well as the number of hits and tracks in the event as

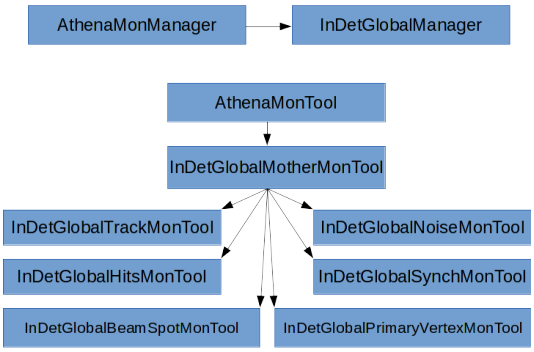

Figure 3.2: The inheritance diagram of the `ATHENA` tools used in the ID global monitoring. The tools inherit from a common base class, derived from the `ManagedMonitoringBase` package, which provides the basic monitoring interfaces. The last row of tools provide basic monitoring of beamspot and primary vertexing which were contributed to ID Global monitoring.

a function of Bunch Crossing IDentification (BCID). The BCID is the identification number given to each bunch in the accelerator. These checks were particularly useful during commissioning.

InDetGlobalNoiseMonTool checks the noise occupancy of the detectors and any correlation between them. The noise occupancy determination is very simple, using a direct subtraction of hits associated to tracks from the total detector occupancy. While this strategy works well in the low detector occupancies during cosmic ray data taking and low-pileup p-p collision runs, which it was designed for, it cannot cope with the occupancies seen in high luminosity LHC runs, deferring to the more advanced noise occupancy monitoring of the sub-detectors.

InDetGlobalPixelMonTool monitors the performance of the tracking with Pixels in mind. Information specific to the Pixel detector is shown for all hits on track in the Pixels.

InDetGlobalPrimaryVertexMonTool Monitors the performance of the primary vertexing in ATLAS. It provides basic information about the spatial distribution of primary vertices, track composition and the quality of fit.

These tools run for each event processed by `ATHENA`. During data taking these tools run in the end of event reconstruction, giving the monitoring access to both the raw detector data as well as to all reconstructed quantities that go into the ESD. It is also possible to produce the monitoring output from ESD files directly.

The package is primarily used in two different settings, during data taking at Point 1 as well as offline reconstruction at Tier-0.

3.1.1 Online monitoring

Within the Point 1 environment the monitoring runs on dedicated machines which sample events in real time, directly from the trigger. The purpose of the online monitoring is to provide feedback to the detector and data quality shifters about detector conditions and give an early alert for potential problems. The overall structure of the online monitoring and related processes can be seen in figure 3.3.

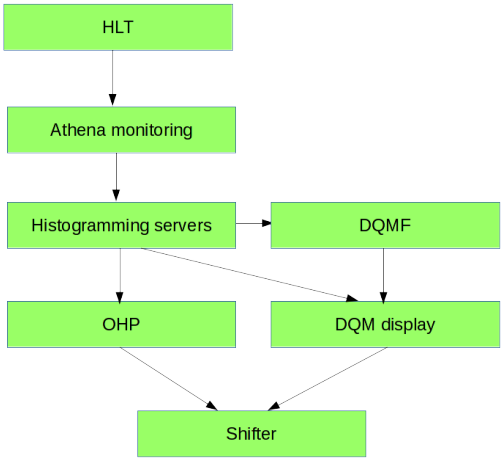

Figure 3.3: An overview of the components of the online monitoring in Point 1 for the ID. The entire reconstruction and monitoring runs alongside the ATLAS trigger and DAQ software during regular runs with the `OHP` (Online Histogram Presenter) and `DQMD` (Data Quality Monitoring Display) tools used by the shifter to view the output.

The monitoring runs within dedicated `ATHENA` jobs, which do full reconstruction of ID data. During the 2012 run this was done in jobs which provided output for all the ID detectors. The histograms produced by the ID monitoring are checked by the ID shifter.

Two machines were used for this purpose, each with eight cores and 24 Gb RAM, running eight reconstruction processes in parallel. The total number of jobs was limited by CPU and network utilisation. The reconstruction only runs the ID reconstruction and tracking. The sampled events come from the `express`, `JetTauEtmiss` and `Egamma` streams. An additional set of jobs is used to provide monitoring of the detector's noise occupancy; this is best done with empty events, sampled from the so-called ID monitoring stream, which outputs these empty events at a fixed rate. Finally, a dedicated job is

used to produce detailed output of the current status of the Pixel detector, producing output for each individual module.

For the physics stream monitoring there is a dedicated gatherer application that merges the histograms from each job to provide the final histograms displayed to the shifter, with the total gathered statistics.

The shifter gets information from the monitoring through two applications, `OHP` [18] and `DQMD` [19]. The `OHP` application produces customised views of the monitoring histograms, giving an easy overview to the shifter and gathering related histograms together. The `DQMD` application displays histograms and the result of automatic tests that are run on the histograms.

The online rate for running `ATHENA` reconstruction and monitoring is about 1 Hz per process on the monitoring machines, giving a total of 8 Hz sampling rate for the physics stream monitoring jobs. The total rate was limited by the processing power of the machines and network usage. This results in a restriction in the statistics that are available. For noise occupancy monitoring the event processing speed is much higher, since reconstructing empty events is much faster.

3.1.2 Offline monitoring

During offline processing the monitoring runs after reconstructing the RAW detector information to produce ESDs or after reconstruction of ESDs to AODs [20]. In contrast to the online mode all gathered events are available at this stage. The monitoring output of the offline monitoring is the authoritative view on DQ as it provides a full view of the run.

Offline reconstruction monitoring is done in two passes. The first pass, where only the `express` stream is processed and the bulk pass where all streams are processed. The first pass starts immediately after data taking and the results are used for initial data quality assessment and to check for changes in detector conditions and calibration, which is done in the so-called calibration loop. Following the calibration loop the bulk processing starts.

The most important part of the calibration loop for the ID global monitoring is the beamspot determination [21], which determines the extent of the luminous region where collisions happen. After the beamspot position has been determined, it is used in the bulk processing as a de-facto measurement in track reconstruction, ensuring that all tracks have their origin in the luminous region.

In the bulk processing the ID global monitoring is run on the `express` stream as well as the `JetTauEtmiss` physics stream, chosen due to the large number of events therein with high track multiplicity. The monitoring runs on one physics stream only in order to limit the use of computer resources at Tier-0.

At the end of processing the output of the monitoring is assessed by DQ shifters to ensure there are no problematic data to be used by physics

analyses. Any such problematic issues are then recorded in a dedicated database. Each issue is stored in the form of a "defect" along with the associated time duration, in terms of LBs [22], and details to describe what was observed.

The defects themselves are prespecified problematic conditions. These describe specific problems for data quality, e.g. regions with low tracking efficiency or a bug in software affecting reconstruction. A defect can be set as intolerable or tolerable, which determines if a LB with a given defect is suitable to be used by physics analyses.

3.2 Monitored quantities

The ID global monitoring checks quantities related to the tracking in the ID. This is complementary to the ID alignment monitoring, which monitors the efficiency and tracking residuals, and the ID performance monitoring, which checks for the reconstruction and properties of some basic resonances, using ID and muon tracks.

The track collection monitored is the complete collection of primary tracks, i.e. tracks reconstructed by the inside-out Pixel and SCT seeded tracking, see section 2.6. A $p_{\mathrm{T}} > 0.5\,\mathrm{GeV}$ selection is made, to only keep tracks that traverse the whole ID detector. In addition, during 2012, Pixel tracklets were reconstructed in the high-η region where only Pixels provide coverage, to be combined with muon spectrometer hits to form muon tracks in the high η regions.

3.2.1 Hits on Track

The number of hits associated to each reconstructed track are monitored for all primary ID tracks. Examples of such distributions are shown in figure 3.4, showing the number of hits in each subdetector for all ID tracks. This is also broken down by the η and ϕ parameters of the track to allow potentially problematic regions to be localised.

The number of hits are checked as a function of η-ϕ as well as an average over the primary tracking regions in η, covering the barrel, end-caps and the transition region between the two. This provides a good check of the hits in the various regions. Examples of these distributions are shown in figure 3.5, showing the $\eta - \phi$ distribution of hits and dead modules for the Pixel and SCT detectors. If a detector is suffering from inefficiencies or the number of disabled modules across a particle trajectory goes up this would be visible in these plots.

Additionally, hitmaps are produced in the x-y and z-r coordinate frames, see figure 3.6. These show the accumulated number of hits associated to a track in the detector and is a useful tool for visual inspection of the run. These make it possible to check that combined track reconstruction worked

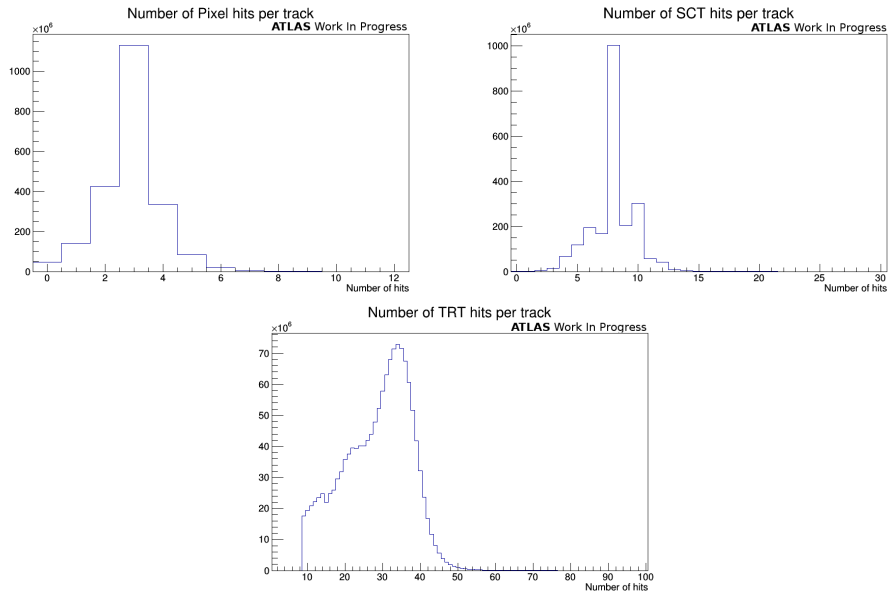

Figure 3.4: Number of hits per track in each subdetector. Disabled modules a track passes by are counted as hits.

during cosmic runs or to see if any parts of the detector are not working properly. While useful in the early stages of the first LHC run, producing these plots is quite demanding on computing resources, so these plots were disabled to conserve CPU time and memory.

These distributions do not provide specific information on the nature of problems but can be useful in spotting potentially problematic regions. The primary purpose is to spot generally problems and possibly assist other combined performance groups in identifying and understanding problems. One example of this is shown in the bottom left plot of figure 3.5, where in the upper left corner a disabled SCT endcap quadrant is visible (disabled due to a dead cooling loop, in 2012). In figure 3.6, where hits from TRT only tracks are shown, it can be seen that part of the detector hits are not being associated with tracks, around $\phi_0 = 0$. As there was no drop in occupancy in the TRT around that region the tracking was investigated and a problem was found in associating hits to the track in that region due to ϕ_0 coordinate not wrapping around at $\phi_0 = 0$ correctly.

Within the online environment the number of Pixel and SCT modules that are either in error or are disabled are also tracked in bins of η and ϕ to identify potential regions where problematic modules align. These maps are updated at the start of each LB in order to minimize the time needed to access the conditions DataBase (DB); this should not cause problems as conditions are stable during a LB. Examples of such plots are shown in fig-

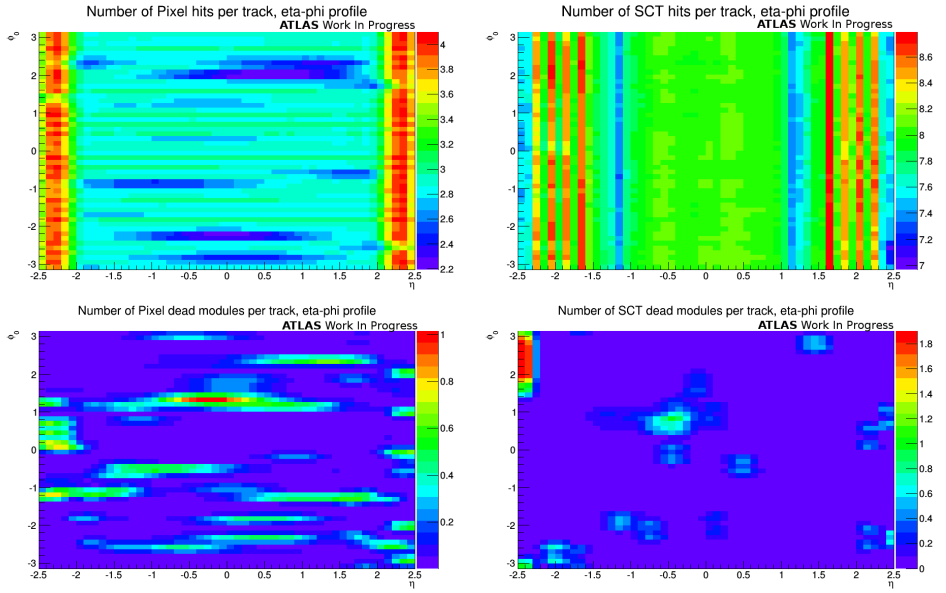

Figure 3.5: The distribution of the number of hits per track in η and ϕ. Shown here is the number of Pixel hits (top left) and SCT hits (top right). Also shown is the average number of dead Pixel (bottom left) and SCT (bottom right) modules traversed by each track. As an example a quarter disk of dead SCT modules can be seen in the top left corner in the bottom right plot. The average number of hits depends on the η of the track, with variations due to modules with errors or low efficiency. The filled entries in the disabled module plots correspond to disabled modules in the Pixel and SCT, with different sizes due to the positioning of each module.

ure 3.7. These plots allow us to check whether disabled modules or modules in error have an effect on tracking during the run. These checks are important since as the run progresses modules can go into an error state. This is especially true in high luminosity collisions where the rate of data and the effect of radiation on the electronics can cause problems in the electronics. This leads to modules slowly being disabled, but with no geometric correlation, save for the fact that the innermost layers of the ID are more affected. It is important to note that this check does not rely on the tracking at all; rather, it makes assumptions about the tracks, that they are straight and originate at the center of the detector, with a set longitudinal spread around the interaction point, Δz_0. With a correctly set parameter this can give a good approximation of the effects on the tracking, at least for high-p_{T} tracks. While this was only available online during the 2012 run, the monitoring has been updated since then to produce these plots also in offline monitoring in a similar manner.

The number of holes in the track are also monitored, that is to say

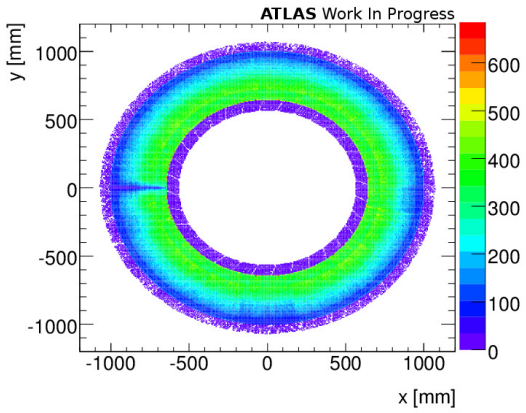

Figure 3.6: The x and y coordinates of hits associated to a track in the ID. Shown is an example of TRT only hits for a collisions run with a problem where TRT hits at $\phi = \pm\pi$ are not associated to a track, due to a bug in track reconstruction where ϕ is not wrapped around $\pm\pi$.

active modules in the detector that did not produce a hit, but where the extrapolated track assumes a hit should be in place. A limited number of such holes are allowed in each track fit, else the fit can fail.

3.2.2 Track distributions

The track parameter distributions are also checked, in particular the η-ϕ distribution of the tracks to spot possible defects due to detector effects; this is done with various sets of cuts. The quality criteria are fairly loose, focusing on each detector in turn. This allows to see if a given detector causes problems to the tracking. Examples of these distributions are shown in figure 3.8, top. Of note is the b-layer which is explicitly checked to ensure there are no inefficient regions, see figure 3.9. This is of particular importance as several algorithms for physics object reconstruction explicitly assume that the b-layer is working at full efficiency.

These distributions are also produced as fractional displays of the total number of tracks showing the fraction of tracks satisfying each selection criterion, allowing to easily spot any deficiencies relative to the expected number of tracks.

In addition, for the forward Pixel tracklets the distribution of η-ϕ is checked separately, shown as example in figure 3.10.

The number of hits in each subdetector as well as the total number of tracks as a function of BCID is also displayed, which is useful for looking at the response of each detector when there are beams, shown in figure 3.11. This allows for a very low level check of the detector response to the colliding bunches, and is useful when there is a smaller number of colliding bunches

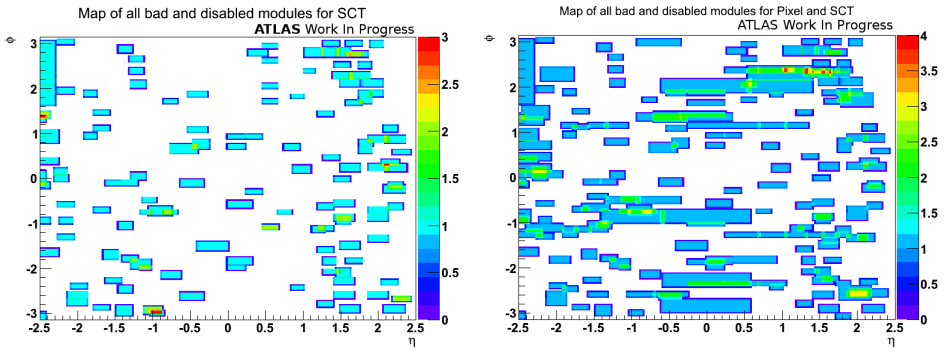

Figure 3.7: Number of modules in error or disabled along a straight track. The x- and y-axis show the ϕ and η parameters of the tracks and the value of each bin the number of problematic modules traversed. On the left is a plot of disabled SCT modules and on the right the number of modules in error and disabled modules for Pixel and SCT combined. Disabled modules are seen as rectangular regions, the size varying due to the different angular size of modules. The borders around the regions are due to modules covering only a fraction of the bin area. The information comes directly from the Conditions DB.

in the machine, in the earlier parts of the run and during commissioning.

Additionally, graphs of the total number of tracks as a function of LB which is used to check for the stability of the number of tracks in time. The average number of tracks per event is also shown as a function of LB. These plots are shown for illustration in figure 3.12. This has two prominent features, one being that the plot itself follows the decreasing luminosity envelope for the run as well as having kinks due to changes in the trigger menu during the run.

3.2.3 Synchronisation

A number of plots is also produced to check the synchronisation of RODs in the ID. This is an error condition when one of the RODs goes busy. This can have large effects on the tracking in certain conditions as the data from these RODs will be lost; these plots detect whether the run contains such conditions. An example of such a plot can be seen in figure 3.13. During online running this information is also automatically checked by the DAQ software, but these plots provide an offline record.

3.2.4 Granularity in time

Within the `ATHENA` monitoring framework the default setting is to produce all the above distributions using data from the entire run, but it is also possible to make the distributions from limited time intervals. This is very

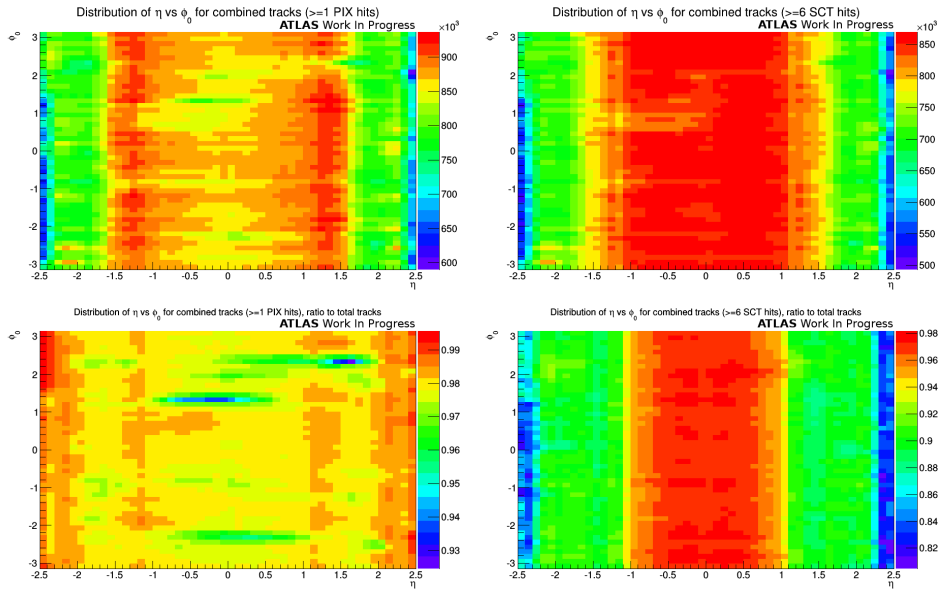

Figure 3.8: The distribution of tracks in η and ϕ. Shown here is the selection of at least one Pixel hit (left) and at least six SCT hits (right). At the top is the number of tracks passing these criteria and at the bottom the ratio of these tracks to the total number in each bin.

important since detector problems commonly affect only parts of the run, either because they are temporary or fixed. The lowest possible interval for such distributions is 10 LBs intervals, which corresponds to at most ten minutes of data-taking. It is possible that this interval is smaller, since LBs switch when detector conditions change. It is also possible to produce distributions per LB, but this is avoided, due to the heavy impact on the size of the monitoring output as well as the limited statistics available in a single LB.

During online running a different approach is used, where histograms are built from data of the last ten LBs. This is a compromise between getting the statistics needed to get enough information about the detector condition and not losing out the current conditions due to the high number of previously accumulated events. This is a specially developed class that wraps the histogram classes and allows to make such histograms for arbitrary LB ranges, at the cost of higher memory usage and an extra delay at the beginning of each LB as the histogram is rebuilt from the buffers.

This splitting into different LB ranges is done for the tracking η-ϕ distributions as well as the number of hits per track. The data quality framework only provides 10 LB granularity, smaller intervals would result in very large storage requirements. However, the number of LBs rejected is usually re-

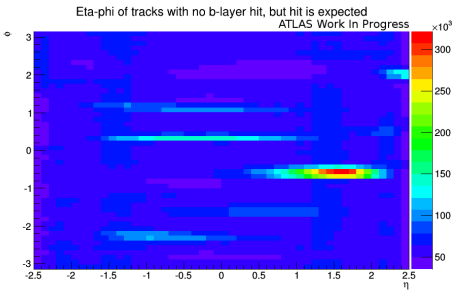

Figure 3.9: Number of tracks with a missing b-layer hit, when a hit is expected. If a module is disabled it does not show up. As a b-layer hit is a requirement for many algorithms used to reconstruct physics objects, this in an important check.

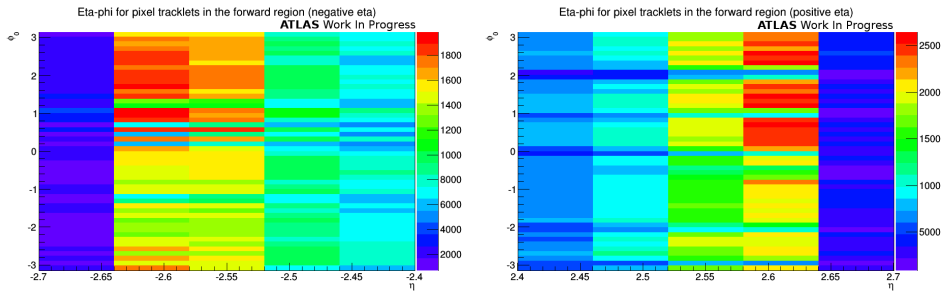

Figure 3.10: Distribution of forward Pixel tracks in η and ϕ, in the end cap side A on the left and end cap side C on the right.

duced using feedback from the subdetectors where the extent of the problem in time can be identified.

3.3 Data Quality

The following defects are defined for the ID global monitoring, with further details given in the rest of the chapter:

ID_NOTRACKS **INTOLERABLE**
Significant loss of tracking coverage throughout or in a region of the ID.

ID_OUTOFTIMETRACKS **INTOLERABLE**
Fake tracks formed by out-of-time pileup hits in the SCT.

ID_TRACKBUG **INTOLERABLE**
Problem in the tracking caused by a software bug.

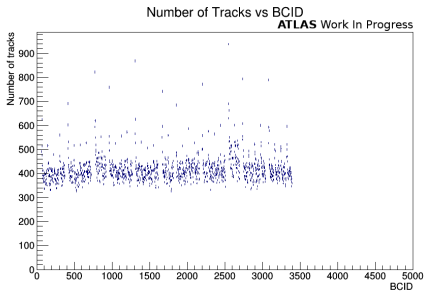

Figure 3.11: The average number of tracks per event by BCID number. This plot includes events from the entire run. These plots are also available showing the number of hits in each subdetector.

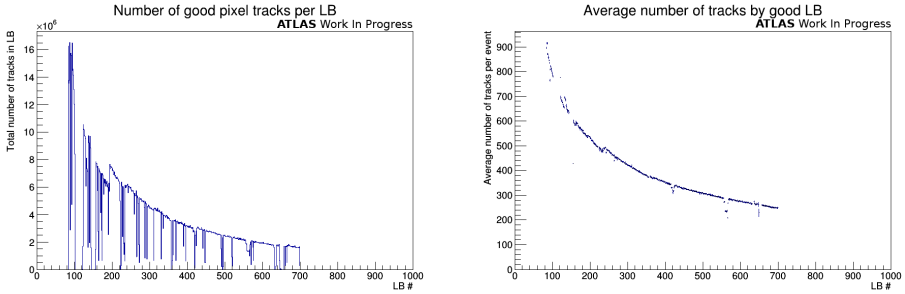

Figure 3.12: The figure on the left shows the number of tracks in each event satisfying various criteria by LB. The figure on the right shows the average number of tracks per event split by LB. The luminosity profile of the run can be seen in these plots as well as jumps arising from changing trigger conditions. Gaps arise due to times when the detector is busy and not taking data.

ID_VERTEXBUG **INTOLERABLE**
Problem in the vertexing caused by a software bug.

ID_BLAYER_EFFICIENCY **INTOLERABLE**
Tracking affected by low efficiency in the Pixel b-layer

ID_PIXEL_TRACKCOVERAGE TOLERABLE
Small loss of tracking efficiency due to modules in the Pixel.

ID_SCT_TRACKCOVERAGE TOLERABLE
Small loss of tracking efficiency due to modules in the SCT.

ID_TRT_TRACKCOVERAGE TOLERABLE
Small loss of tracking efficiency due to modules in the TRT.

The defects in bold are those that are set as intolerable, meaning that LBs where these defects are set are not used in physics analyses. The other

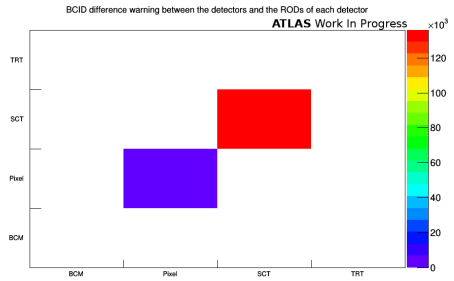

Figure 3.13: Synchronisation between the RODs in each detector. Each ROD in detector has a counter of which BCID it is looking at. Under certain conditions it is possible that a ROD fails to update this counter and therefore not in the same state as the rest, this is referred to as a desynchronisation. Each entry denotes desynchronisation in one event. Diagonal entries mean one of the the detector RODs is not synchronised with the rest, while off-diagonal entries mean that the RODs of two detectors are desynchronised, the figure showing desynchronisation of Pixel and SCT RODs.

defects are there for book keeping and tracking abnormalities in the data that might prove to be a problem later on.

The combined output of the DQ assessment is the so-called Good Run List (GRL). This is a selection of LBs that are suitable for use by physics analyses, i.e. not containing any intolerable defects. As analyses can have different requirements from the detectors and physics objects it is possible to construct specific GRLs for each physics. In the 2010 and 2011 runs there were many GRLs produced, while in the 2012 run the different GRLs were collapsed into a common physics GRL.

The GRL is specific to each processing of the same data, as different kinds of defects can be expected to be fixed after a reprocessing of the data. After each reprocessing a new evaluation of the data is done in order to check for improvements or catch possible regressions.

In addition to the GRLs used by physics analyses a “tight” GRL is also defined, where even smaller defects are also excluded. This is done to provide a possible way for analyses to check if they are affected by smaller issues in DQ that were not foreseen to have an effect. Defects such as smaller differences in track coverage are found in this GRL, e.g. LBs marked with the ID_PIXEL_TRACKCOVERAGE detect are excluded from the tight GRL.

ROD busy issues

The cabling from the detector modules to the RODs is different between the ID subdetectors. This means that the effect of a problematic ROD on the tracking can vary depending on which detector it corresponds to.

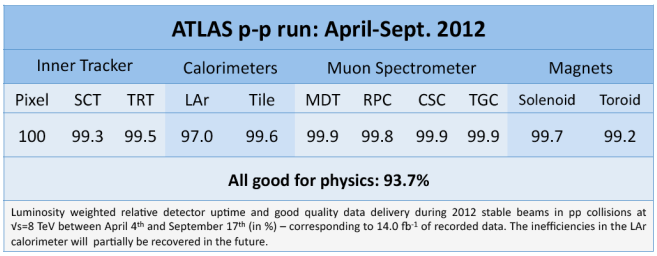

ATLAS p-p run: April-Sept. 2012										
Inner Tracker			Calorimeters		Muon Spectrometer				Magnets	
Pixel	SCT	TRT	LAr	Tile	MDT	RPC	CSC	TGC	Solenoid	Toroid
100	99.3	99.5	97.0	99.6	99.9	99.8	99.9	99.9	99.7	99.2
All good for physics: 93.7%										

Luminosity weighted relative detector uptime and good quality data delivery during 2012 stable beams in pp collisions at $\sqrt{s}$=8 TeV between April 4th and September 17th (in %) – corresponding to 14.0 fb^{-1} of recorded data. The inefficiencies in the LAr calorimeter will partially be recovered in the future.

Figure 3.14: A summary of the performance of the ATLAS detector DQ throughout the 2012 LHC run. Shown is the percentage of integrated luminosity excluded from the GRL due to problems spotted by the DQ process of each subdetector.

For the Pixel detector the modules belonging to each ROD all belong to the same layer. A loss of one ROD will result in a number of tracks with a missing hit, but only in one layer. At the same time this also means that a possible loss of a b-layer ROD can cause significant disturbance by compromising accurate vertexing for the affected tracks.

In the SCT barrel the RODs are arranged in a radial layout, meaning that each ROD covers the same η-ϕ region across all the layers in the barrel. The result of this is that a ROD busy results in many modules along the track path being disabled. While the tracking can handle disabled modules along a track, the tracking will fail when such a high number of disabled modules is present.

Disabled modules

Typically, modules that are disabled will have little effect on the tracking, as the tracking algorithms take this into account. In cases where many such modules align however this can be problematic as the tracking needs a certain number of hits to be able to perform.

To establish this issue the η-ϕ map of tracks is used. In cases where such alignments take place it is possible to get a situation where tracks cannot be reconstructed at all, either due to track seeding being unable to construct seeds or the track fit failing due to a large number of disabled modules. This is identified as a region in η-ϕ where there is a significant deficiency of tracks compared to other regions. This is recorded as the `ID_NOTRACKS` defect.

In most cases however, the disabled modules are picked up by the tracking as dead modules without this having an effect on the number of reconstructed tracks. In this case the effects, if any, on the tracking are minor, as this is a design consideration for the tracking algorithms. In cases where this amounts to more than 10% of tracks missing this is recorded as the `ID_PIXEL_TRACKCOVERAGE`, `ID_SCT_TRACKCOVERAGE` and `ID_TRT_TRACKCOVERAGE` defects; depending on which subsystem is responsible for the performance

degradation.

One important aspect of this is the need to be able to decide during data-taking in Point 1 (P1) whether detector conditions can cause a problem and therefore the run should be stopped to fix problems in the run. This function will be served by the disabled and error module maps.

B-layer issues

Issues arising in the Pixel b-layer have strong implications for the reconstruction and identification of many physics objects. Many algorithms rely on the presence of b-layer hits, when one is expected, to reject fake objects. This is particularly true for the b-tagging and electron identification. The primary responsibility for assessing the impact of such effects on DQ lies with dedicated groups and monitoring tools for each reconstruction object.

However, it is possible that inefficiencies in the b-layer to overlap with other inefficiencies in the sub-detector causing problem to the tracking. This is checked by comparing the $\eta - \phi$ distributions of tracks to the $\eta - \phi$ distribution of tracks lacking b-layer hits, to see if regions of problematic b-layer modules are potentially causing losses in the tracking.

A more severe issue is whether there are losses due to inefficient b-layer modules that are not masked (potentially leading to efficiency loss in other CP groups). A b-layer hit is required in order to reject possible fake objects. This was unfortunately not spotted in the 2012 run, but steps have been taken to cover such cases.

Software issues

Defects related to software issues are also taken out in the GRL, though these can be corrected in reprocessings. These issues are rooted in bugs in the vertexing and tracking and can cause large scale problems for physics analysis. However only a small fraction of the data collected are affected by such issues. These issues are tracked using the `ID_TRACKBUG` or `ID_VERTEXBUG`.

Beamspot issues

Defects related to beamspot determination are also taken out from the GRL as they have a significant effect on the reconstruction of other physics objects. This is mostly affecting LBs where there is a smaller number of vertices due to low luminosity or large movements in the beamspot due to Van de Meer scans for example. Typically such data is not suitable for physics analysis and therefore excluded.

Calibration and timing

Additionally, there are cases where the calibration of TRT is problematic, meaning that no hits get associated to the track.

For earlier runs when the bunch spacing was first reduced to 50 ns the hits in the detector can also come from earlier bunch crossings. The results in reconstructed tracks that are fake, forming from hits that do not belong to the same collision. Such occurrences are tracked using the `ID_OUTOFTIMETRACKS` defect. The issue itself is fixed by tightening the timing selection for hits used in track reconstruction. As this issue can be fixed by changing the settings of track reconstruction this issue is fixed after a reprocessing.

3.3.1 Performance during the 2011 and 2010 runs

The amount of data lost during 2012 due to problems spotted by the ID monitoring is summarised in table 3.14. The primary reason for lost data is the SCT RODs going busy which result in certain LB where tracking is severely affected in certain regions. These losses occur in the barrel where due to the detector readout geometry a ROD corresponds to a roughly rectangular sector in η-ϕ coordinates across all layers of the SCT.

A summary of data that was rejected from the GRL due to defects related to the tracking can be found in table 3.1 showing the percentage of luminosity lost in each data period for the 2011 and 2012 p-p collision runs as well as the 2011 Pb-Pb run and 2013 p-Pb run.

3.4 Conclusions and outlook

The monitoring ran successfully throughout the first LHC run and was able to spot problems as they arose and monitoring the development of others. It was important both during the start of running, with focus on detector performance and feedback, as well as during the later part of the run, moving focus to combined performance effects.

It provides an interface between the ID detectors and the Combined Performance (CP) groups as well as combined performance during the early stages of the LHC run.

In online monitoring the main limiting factor for discovering problems in the tracking was the statistics collected, as the monitoring samples only a fraction of recorded events. Additionally, a larger number of machines is foreseen to be used in the next run, as well as improvements in the tracking CPU time use should improve on the monitoring rate.

Additionally, the monitoring needs to have as up-to-date information on the detector conditions as possible. To this end a solution was found by sourcing the information about module status and errors directly from

Year	Period	Good data [%]	Year	Period	Good data [%]
	A	98.4			
	B	98.1		B	95.4
	C	92.0			
	D	98.6		D	99.4
	E	96.4		E	100.0
2012			**2011**	F	98.7
8 TeV	G	99.1	**7 TeV**	G	99.1
	H	99.5		H	98.4
	I	97.9		I	99.9
	J	97.1		J	100.0
				K	99.8
	L	96.9		L	95.8
				M	98.4
Overall		**98.1**	**Overall**		**97.5**
	A1	100.0		N	98.5
	A2	99.0			
	A3	97.8			
2013	A4	96.0	**2011**		
p-Pb	B1	100.0	**Pb-Pb**		
	B2	100.0			
	B3	78.3			
	B4	98.9			
Overall		**98.0**	**Overall**		**98.5**

Table 3.1: Summary of data lost due to defects in the data ralated to tracking and the ID detectors in the 7 TeV run and 8 TeV run. Missing entries correspond to periods in each year that do not contain physics data and therefore not taken into account for DQ assessment.

`ATHENA` which limits the statistics needed since we are not relying on reconstructed tracks. This is in the form of the η-ϕ disabled and error module maps.

With respect to DQ the ID monitoring package was part of the DQ assessment for the ID. This meant the weekly review of the runs, including both initial assessment of collected data, re-assessment of the bulk processing and follow-up of potential problems as well as assessment after data reprocessing campaigns.

Preparations for the start of the LHC Run-II in 2015 have started, with the ID monitoring already fully integrated and ready for data taking in the next run as well as cosmic data taking during detector commissioning. Testing as part of the ATLAS readiness milestones has also begun. This

includes updates to the new version of the software packages for the new ATLAS release and updates to take into account the experiences of the past year.

Chapter 4

Minimum bias physics

Minimum bias physics deals with soft QCD events that result from the dominant part of the proton-proton cross-section. These events have very high cross-section but cannot be described by perturbative QCD. These soft interactions are of four different kinds; elastic, single diffractive, double diffractive and inelastic. The total cross-section, σ_{mb} is the sum of these contributions:

$$\sigma_{\text{mb}} = \sigma_{\text{elastic}} + \sigma_{\text{sd}} + \sigma_{\text{dd}} + \sigma_{\text{inelastic}} \tag{4.1}$$

The elastic cross-section covers processes where the protons do not break up in their interaction. The diffractive components cover processes where either one (single) or both (double) protons are scattered into a low-mass state. The defining characteristic of the diffractive component is a large separation between the resulting outgoing particles, particularly in η. Finally, the inelastic component contains events where both protons break up and interactions between coloured particles take place. For the diffractive and elastic components a large number of events are not recorded as they fall outside the acceptance of the detector, in order to correct for this model-dependent assumptions about the kinematics of these events are needed.

This is the total cross-section, but for the measurement in an experiment these cross-sections must also include a correction for the acceptance of the detector itself, since at least some particles must be present in the event to be able to trigger the detector. As, by definition, the minimum bias events are those that trigger the detector and are recorded the events are defined with respect to the detector recording them.

The ATLAS minimum bias analysis [23] relies on particle level observables alone without attempting to correct the components above, resulting in a mixture of the different processes within the sample. At the same time a large fraction of the diffractive components is not seen in the detector as no observable particles are produced. As the distributions are defined by particle level observables alone the distributions can be reproduced using Monte-Carlo generators using the efficiencies of the trigger and tracking,

allowing new tunes of Monte-Carlo software to be compared against the distributions of the analysis.

This results in the most useful information for tuning MC and as input to theory, but is not as useful for making comparisons to other experiments which produce distributions with full corrections for the missing components.

The observables from minimum bias analyses carry large importance in the field of MC tuning. In addition, minimum bias events are very similar to pileup events in the high luminosity LHC conditions. For this reason understanding such events is important for all other ATLAS analyses. Due to the soft nature of these QCD events is also not possible to describe them by perturbation theory, requiring phenomenological approximations which are parametrised in the Monte Carlo (MC) generators. Measurements of the properties of such events are therefore important for producing the best possible tuning of these free parameters at the LHC energy scale.

The distributions considered in this analysis are the track multiplicity

$$\frac{1}{N_{\text{ev}}} \cdot \frac{dN_{\text{ev}}}{dn_{ch}},$$

the track p_{T} spectrum

$$\frac{1}{N_{\text{ev}}} \cdot \frac{1}{2\pi p_{\text{T}}} \cdot \frac{d^2 n_{\text{ch}}}{d\eta dp_{\text{T}}},$$

the track eta distribution

$$\frac{1}{N_{\text{ev}}} \cdot \frac{dN_{\text{ev}}}{d\eta}$$

and the mean p_{T} of tracks in each event versus the track multiplicity ($< p_{\text{T}} >$ vs n_{ch}). N_{ev} refers to the total number of events accepted by the analysis and n_{ch} is the number of charged particles in each event. Only primary charged particles are considered, i.e. particles originating from the primary vertex.

4.1 Cross check analysis

For the minimum bias analysis a full cross check analysis was done alongside the main analysis. Here we refer to the nominal analysis as Analysis-I and the cross-check as Analysis-II. The cross-check analysis uses the same inputs as the main analysis but is done with independently developed code and procedures. The goal is to check the validity of the selection, corrections and systematic error determination for the most inclusive phase space considered in the paper, see section 4.1.1 for the definition.

The data considered in the analysis consists of six early 7 TeV runs[1]. In addition to this run selection additional selection criteria are used to ensure the good quality of data used in the analysis:

[1] 152166, 152214, 152221, 152345, 152409, 152441, 152508

- Good DQ for all ID detectors and successful beamspot determination
- `L1_MBTS_1` trigger fired
- At least one vertex with at least two **selected** tracks, see section 4.1.1.
- Pileup suppression, no additional primary vertices with four or more tracks.

The `L1_MBTS_1` trigger uses the MBTS, two plastic scintillator end-caps placed on each side of the LAr barrel, see section 2.4. It requires at least one hit on either side of the detector. This gives minimal requirements on the activity in the detector for selected events. The other selections ensure that an interaction took place in the event and suppress events with substantial pileup vertex contributions. The number of events accepted after each of these selections is shown in table 4.1.

4.1.1 Phase space

The primary phase space of the analysis ($n_{\text{sel}} \geq 2$, $p_{\text{T}} \geq 100\,\text{MeV}$ and $|\eta| \leq 2.5$, was fully cross checked. The following track selection criteria apply, where the selection used in the primary phase space is highlighted:

- $p_{\text{T}} > 100\,\text{MeV}$
- b-layer hit, if active sensor crossed
- At least one hit in the Pixel detector
- At least **2**, 4, 6 SCT hits for the $p_{\text{T}} > \mathbf{100}$, 200 and 300 MeV phase spaces respectively
- $|d_0| < 1.5\,\text{mm}$
- $|z_0 \sin\theta| < 1.5\,\text{mm}$
- χ^2 fit probability > 0.01 for tracks with $p_{\text{T}} > 10\,\text{GeV}$

These selectons ensure that primary tracks are kept, rejecting secondary tracks and fake tracks arising from random hit combinatorics. The p_{T} requirement splits the analysis into multiple phase spaces, the cross-check analysis is applied to the most inclusive phase-space, $p_{\text{T}} > 100\,\text{MeV}$. The last selection is done in order to reject tracks with spurious transverse momentum measurement, an effect of the large extrapolation distance between the Pixel and SCT endcaps. The number of tracks selected after these criteria is denoted n_{sel}. For certain studies an alternative selection is used, including all the above criteria except the requirements on d_0 and z_0. Instead, the transverse distance of the track to the beamspot at the point of closest

approach is used and the selection is $|d_0^{\mathrm{BS}}| < 1.8\,\mathrm{mm}$. The number of tracks passing this set of requirements is referred to as $n_{\mathrm{sel}}^{\mathrm{BS}}$. The uncorrected distributions for η, p_{T} and n_{ch}, after this selection are shown in figure 4.1, which are in perfect agreement between the two analyses. The number of tracks kept after these selections can be found in table 4.1.

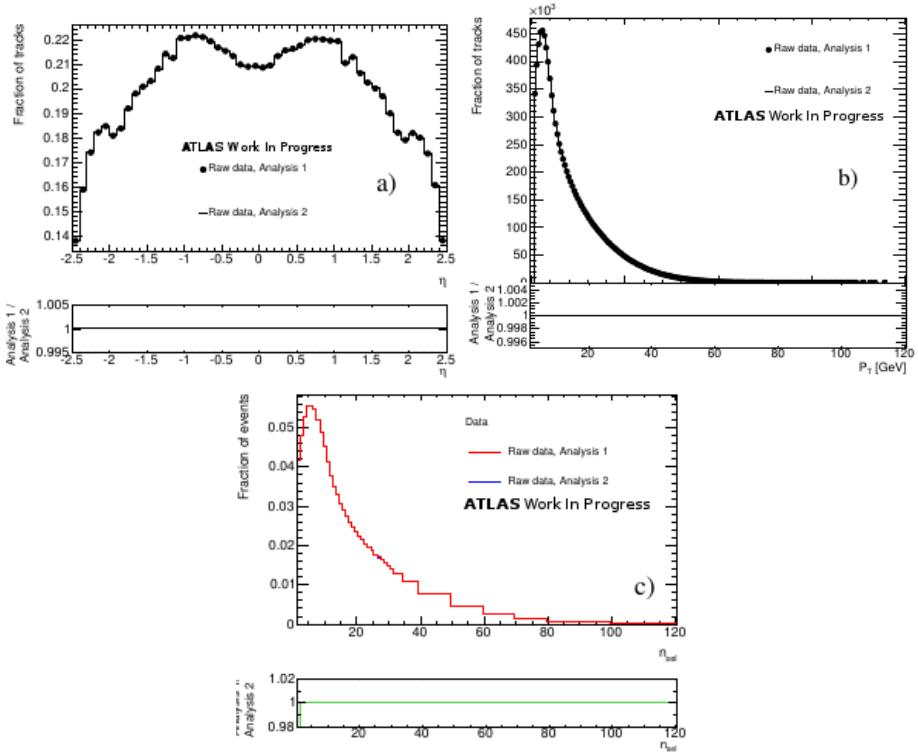

Figure 4.1: The raw distributions of η (a), p_{T} (b) and n_{ch} (c). At this level the two analyses are in perfect agreement.

4.2 Corrections to particle level

At this stage the tracks are selected and the distributions can be made. However, these are not the "true" distributions, rather they are convoluted with detector efficiency and detector effects on observables. These uncorrected distributions are referred to as raw or track level distributions. The distributions after correcting for detector effects are referred to as particle level distributions. Such deconvolution is very important to allow comparison with generator outputs and results from other experiments.

	Run number						
Selection	**152166**	**152214**	**152221**	**152345**	**152409**	**152441**	**152508**
Total events	675766	344531	1487570	1421215	5589888	4902686	1096648
Data quality	514612	250450	1442202	1088865	4733210	4484642	334055
Trigger	437273	212751	1242202	958609	4171423	3978804	295432
Vertexing	389466	188873	1122051	862073	3736987	3576501	264862
Track selection	386669	187438	1113639	855910	3708987	3550540	262889
Total tracks	17508795	8465356	50360637	38830614	168141336	160908202	11902114
Selected tracks	8072503	3899575	23218783	17870135	77243070	74023616	5481758

Table 4.1: The number of events selected after each selection step as well as the number of selected tracks. The numbers are broken down by run number. The same number of events and tracks are accepted by both Analysis-I and Analysis-II.

The corrections applied per-event can be calculated as:

$$w_{\text{ev}}(n_{\text{BS}}^{\text{sel}}) = \frac{1}{\epsilon^{\text{vertexing}}(n_{\text{BS}}^{\text{sel}}) \cdot \epsilon^{\text{trigger}}(n_{\text{BS}}^{\text{sel}})} \tag{4.2}$$

The terms in the denominator account for inefficiencies in the trigger ($\epsilon^{\text{trigger}}$) and vertexing ($\epsilon^{\text{vertexing}}$). These are taken from studies done for the analysis and are used in both Analysis-I and Analysis-II.

The trigger efficiency is determined using a control trigger, which is a random filled bunch trigger at L1, see section 2.7, and a requirement of four hits in the Pixel and SCT detectors. This provides a looser sample with which to gauge the trigger efficiency.

The vertexing efficiency is measured by looking at the ratio of triggered events with a vertex to the total number of triggered events. For this to work it is important to remove the contribution of beam background events, which would skew the efficiency calculation. Additionally, in the case of $n_{\text{sel}}^{\text{BS}} = 2$ an additional correction is applied based on Δz_0^{BS}, the longitudinal separation of the track perigees. The distribution used for the correction is shown in figure 4.2.

Trigger and vertexing corrections are applied as an event wide weight, and the efficiencies are plotted in figure 4.3 as a function of the number of selected tracks.

The tracking efficiency correction is applied per track as a function of p_{T} and η, as shown in figure 4.4. The weight applied for each track can be expressed as:

$$w_{\text{trk}}(p_{\text{T}}, \eta) = \frac{(1 - f^{\text{nonpri}}(p_{\text{T}}))(1 - f^{\text{okr}}(p_{\text{T}}, \eta))}{\epsilon^{\text{tracking}}(p_{\text{T}}, \eta)} \tag{4.3}$$

The factors in the numerator correct for contamination from non-primary tracks (f^{nonpri}) and tracks that are outside the kinematic range of the analysis (f^{okr}), while in the denominator is the tracking efficiency ($\epsilon^{\text{tracking}}$).

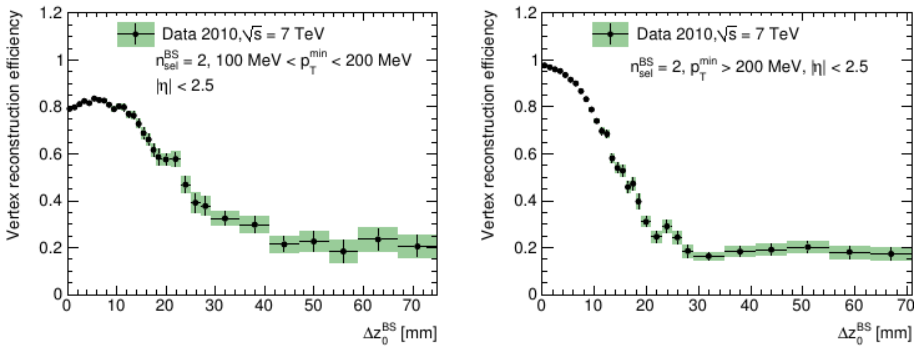

Figure 4.2: The vertex reconstruction efficiency as a function of Δz_0^{BS} for events with $n_{\mathrm{sel}}^{\mathrm{BS}} = 2$. Two cases are considered based on the lowest track p_{T} in the event; events with $p_{\mathrm{T}}^{\mathrm{min}} \leq 200\,\mathrm{MeV}$ (left) and $p_{\mathrm{T}}^{\mathrm{min}} > 200\,\mathrm{MeV}$ (right).

The tracking efficiency is estimated from MC, by checking the reconstruction efficiency of charged particles in bins of p_{T} and η. As the tracking efficiency is determined using MC, excellent agreement between the data and MC simulation is needed to obtain valid results. Some examples of the level of agreement can be found in figures 4.5 and 4.6, showing the high degree of accuracy of the MC simulation across the full pseudorapidity and transverse momentum range considered in the analysis. The procedure for matching reconstructed tracks to truth tracks is to give a match if the true and reconstructed tracks are found within $\Delta R < 0.15$ and the two share at least one Pixel hit. For the tracking efficiency the dependence on two different estimates of the material distribution uncertainty is also shown in figure 4.4. The tracking efficiency correction accounts also for non-primary tracks as well as tracks falling outside the kinematic range of the analysis.

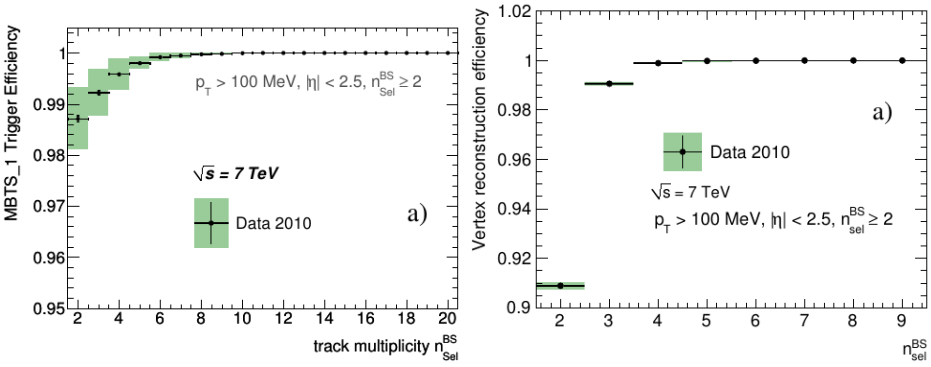

Figure 4.3: A plot of the trigger (left) and vertexing (right) efficiency as a function of the number of selected tracks ($n_{\mathrm{sel}}^{\mathrm{BS}}$). This efficiency is used in both analysis-I and analysis-II as an input for the trigger and vertexing corrections.

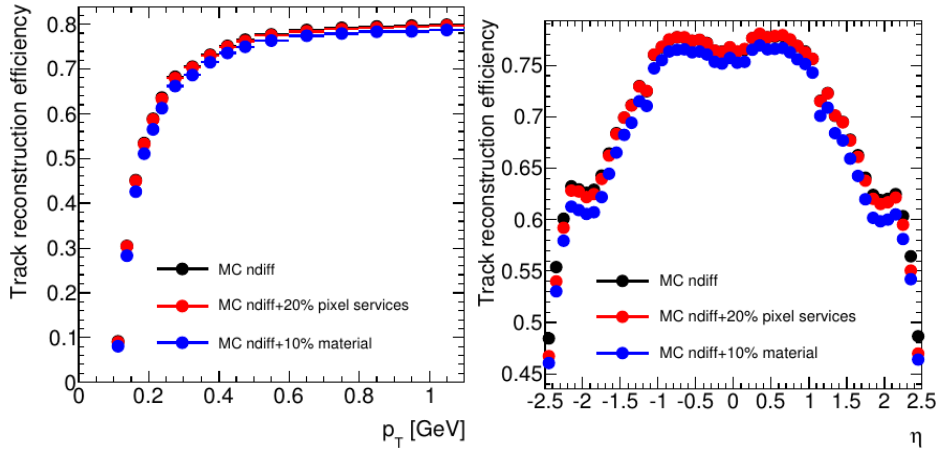

Figure 4.4: A plot of the tracking efficiency as a function of p_{T} (left) and η (right). Additionally, the effect of two material uncertainties are shown for comparison to the nominal distribution, a 10% increase in the material budget and a 20% increase in the Pixel service budget.

4.3 Bayesian unfolding

All the correction procedures used so far rely on weights. In this sense only the relative weights of each bin in the histogram are altered and migration from one bin to another is not handled. In the final step of the correction an unfolding procedure is used, where such bin migrations are properly taken into account. The procedure used in the paper is the so-called Iterative Bayesian Unfolding [24].

The starting point of the procedure is the migration matrix, which describes the probability of a given observed state to be produced from each true state. Using this matrix as a starting point together with Bayes' theorem, it is possible to produce an unfolding matrix, which can revert the observed distribution back to particle level. As this is a Bayesian method, there is a prior involved, in the form of a best guess of the true distribution of the data.

In order to get past this unwanted dependence on a prior, the procedure is modified to be iterative. With each iteration the effects of the choice of prior become less important. The iterations repeat until some termination condition is met, typically a test on the amount of change due to the unfolding. In the case of this analysis the chosen test was that the χ^2 difference between the distributions produced by successive unfolding iterations should be smaller than the number of bins in the unfolding.

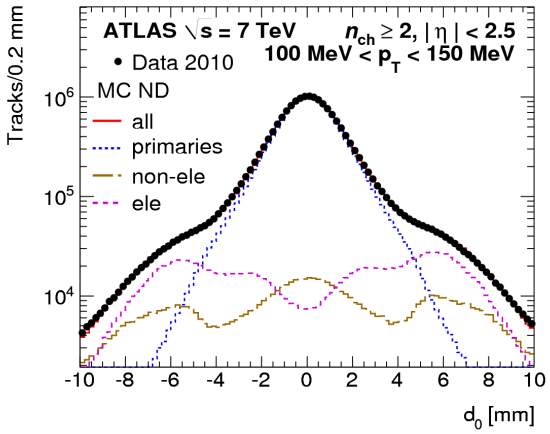

Figure 4.5: A view of the track d_0 distribution, along with the contributions from different sources, taken from MC. The contributions are split up into primary particles (dashed blue) and non-primary particles, electrons (brown dashed) and non-electrons (pink dashed). Excellent agreement between the data and MC simulation is found as well as good understanding of the components of the distribution.

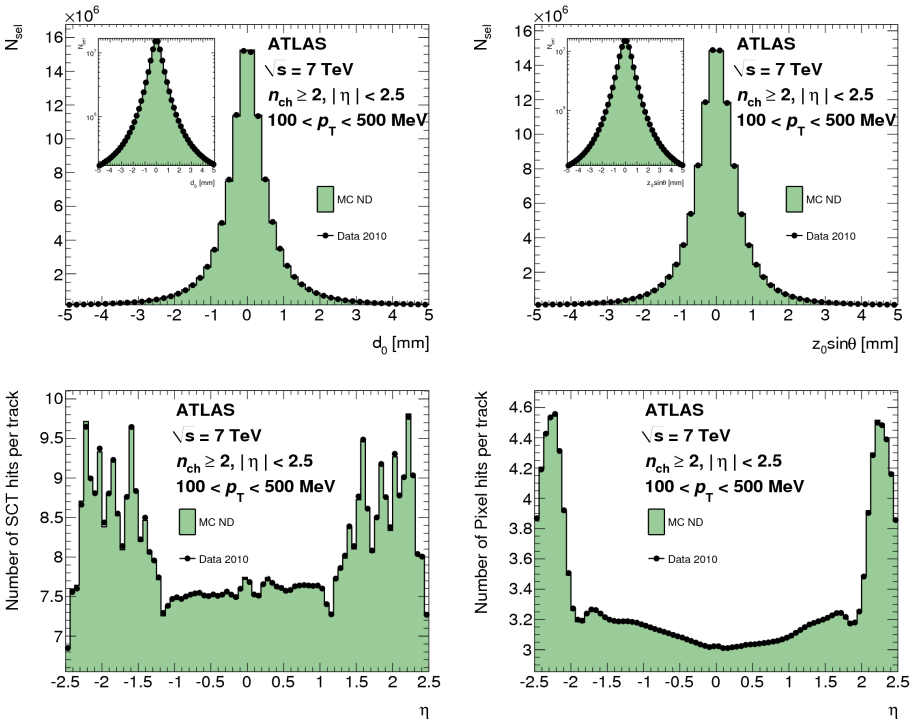

Figure 4.6: Comparison of the data and MC for d_0, z_0 and the number of Pixel and SCT hits; showing very good agreement between data and MC.

4.3.1 n_{ch} unfolding

The unfolding procedure is applied to the n_{ch} spectrum to account for migration between different n_{ch} bins due to the tracking efficiency. This allows to correctly take into account tracks that were missed in reconstruction. The migration matrix is populated by minimum bias MC samples. An efficiency correction is applied to the n_{ch} distribution at the end of the unfolding procedure to account for the fact that events with $n_{\mathrm{sel}} < 2$ fall outside the analysis phase space and therefore cannot be accounted for by the unfolding procedure. This correction,$w_{0/1\mathrm{bin}}$, is the probability of losing all or all-but-one tracks in the event due to tracking inefficiency.

$$w_{0/1\mathrm{bin}} = \frac{1}{1-(1-\epsilon_{\mathrm{trk}})^{n_{\mathrm{sel}}} - n_{\mathrm{sel}}\epsilon_{\mathrm{trk}}(1-\epsilon_{\mathrm{trk}})^{n_{\mathrm{sel}}-1}} \tag{4.4}$$

4.3.2 Transverse momentum unfolding

For the transverse momentum of the tracks a Bayesian unfolding procedure was used, correcting the momentum of the tracks back to particle-level. The procedure uses the migration matrix to migrate entries from their respective bins to the particle-level spectrum. The matrix is populated by minimum bias MC samples as well as single particle MC samples with high p_{T} particles, in order to populate the high-p_{T} bins. The migration matrix used in the procedure is the same that is used by Analysis-I for the final result, though the determination of the matrix is also cross-checked. See figure 4.7 for a visualisation of the matrix contents.

An initial "guess" of the spectrum is neededd and for this the spectrum from a minimum bias `Pythia` MC sample is used. In order to preserve the total number of tracks after unfolding the distribution each column of the unfolding matrix is normalised before the unfolding step.

In order to assess the effect of the prior distribution and correct for any bias this may introduce, the unfolding procedure is repeated with a flat prior distribution. This check results in a 2% uncertainty.

4.4 Cross check results

A comparison of the n_{ch}, p_{T}, η and $< p_{\mathrm{T}} >$ distributions coming from Analysis-II and Analysis-I is shown in figures 4.8. Good agreement is found between the two analyses, with agreement within 0.001% level for the n_{ch} distribution and better than 0.5% across most bins in the other distributions. In all distributions the unfolding procedure was also explicitly checked and found to be in agreement between the two analyses. This level of agreement was found to be satisfactory to rule out any possible issues in the analysis and the complex correction procedures used.

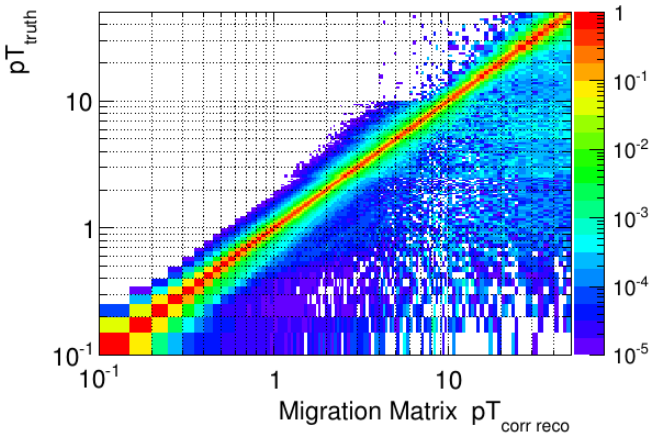

Figure 4.7: A plot of the migration matrix used for the iterative unfolding of the p_{T} spectrum. The reconstructed p_{T} after all corrections is plotted on the x-axis and the true p_{T} on the y-axis.

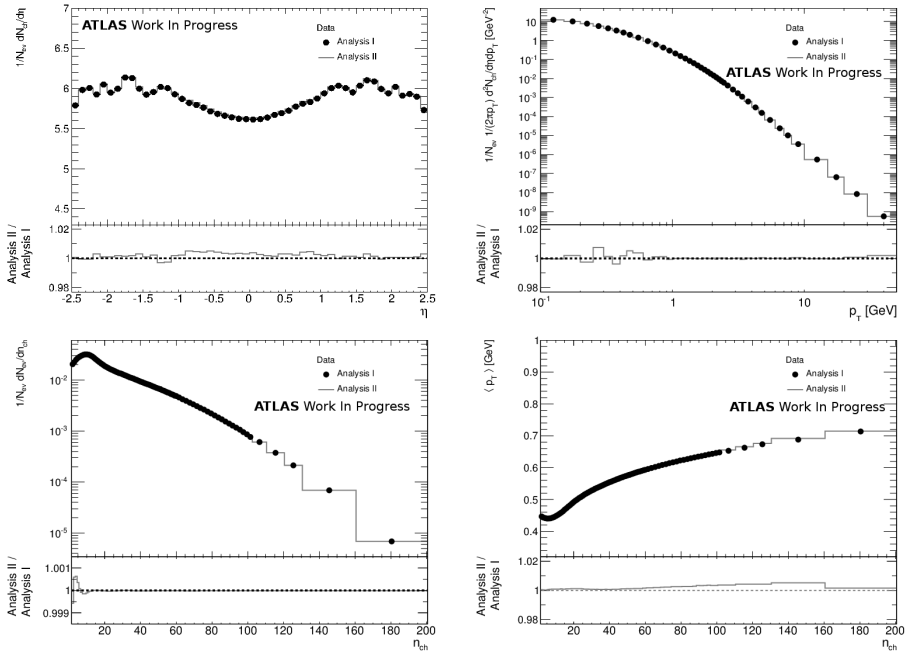

Figure 4.8: Comparison of the distributions produced by Analysis-I and Analysis-II, with a ratio of the two in the lower part. Good agreement is found between the two analyses, in all cases disagreements are below 0.5%.

4.5 Systematic uncertainties

The effect of the dominant systematic uncertainties is also checked in Analysis-II. The estimated systematic uncertainties for Analysis-I and Analysis-II are plotted in figure 4.9 and the good agreement between the two is shown.

4.5.1 Systematic Uncertainties on the n_{ch} distribution

The systematic uncertainties checked on the n_{ch} distribution are the tracking efficiency and detector material uncertainty. Both systematic uncertainties are taken as inputs from dedicated tracking studies and used directly. The exact same distributions are also used by the primary analysis. The systematic uncertainties evaluation is done using a toy MC to remove tracks from the distribution to simulate the tracking efficiency when systematic effects are taken into account. The resulting distribution from this procedure is then put through the unfolding to produce a new distribution, the difference to the nominal distribution is taken as a systematic uncertainty. For the total number of events N_{ev} the same systematic uncertainties are checked, but the only contribution comes from events that might leave the analysis phase space due to systematic variations. The total effect on N_{ev} is at 0.3%.

4.5.2 p_{T} systematic uncertainties

For the p_{T} distribution, the effect of the mis-measurement of track p_{T} is studied. This applies to tracks with $p_{\mathrm{T}} \geq 10\,\mathrm{GeV}$. The estimation is performed by scaling the number of mis-measured tracks in MC to match the number found in data, which is known to be higher. The resulting distribution is then put through the unfolding procedure and the difference found to the nominal distribution is evaluated as a systematic uncertainty. The results are found to be compatible between the two analyses.

Additionally, the effect of the p_{T} resolution systematic is evaluated by introducing a Gaussian smearing to the track p_{T} in MC and taking this modified distribution through the unfolding procedure. Any differences to the final distribution are taken as a systematic uncertainty.

For the two unfolding procedures there is an additional systematic uncertainty related to the amount of non-closure observed, i.e. the disagreement between the true MC spectrum and the unfolded result of the observed p_{T} spectrum. The difference is used as a systematic uncertainty. One possible cause of the observed non-closure is that the unfolding of n_{ch} and p_{T} distributions is done separately, not taking into account correlations between the two variables.

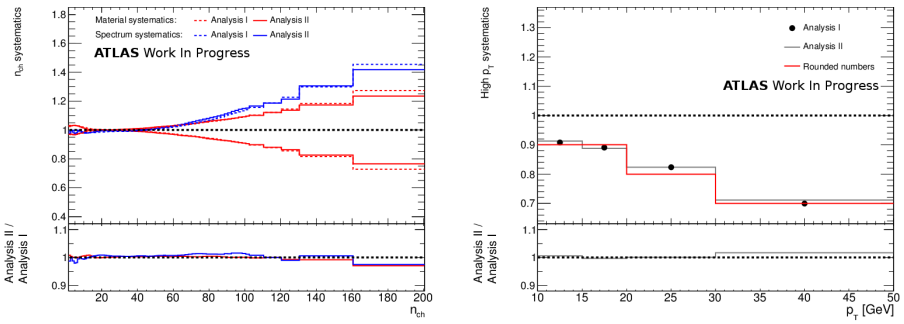

Figure 4.9: Comparison of the systematic uncertainties as estimated by Analysis-I and Analysis-II. Shown are the track multiplicity systematic uncertainties (left) and track p_{T} systematic uncertainties (right). The errors in the two analyses agree to better than 5%.

4.6 Results

Based on the results of the analysis a new tune was produced for `Pythia` 6, named the AMBTS1 tune [25]. This is a best fit of the `Pythia` 6 soft QCD parameters to the ATLAS data. The final results of the analysis can be found in figure 4.10, showing the distributions as well as a comparison to various generators and tunes, to check how they perform. In particular the AMBTS1 tune is also shown.

4.7 Minimum bias energy evolution

At the time of the minimum bias analysis the LHC had runs at CoM energies of 900 GeV, 2.36 TeV and 7 TeV. By analysing data at each of these energies it is possible to determine the evolution of Minimum Bias physics as a function of CoM energy. The evolution of the track multiplicity per unit η is shown in figure 4.11 for the central region, $\eta = 0$. The ATLAS AMBT1 tune is successful in describing the looser $p_{\mathrm{T}} > 500\,\mathrm{MeV}$ phase spaces, but cannot adequately describe the evolution for the most inclusive $p_{\mathrm{T}} > 100\,\mathrm{MeV}$ phase space. The looser phase spaces are adequately described by most considered tunes, though Phojet [26] and the `Pythia` 6 DW tune perform considerably worse, as shown in figure 4.11.

4.8 Conclusions

For the primary phase-space of the 7 TeV minimum bias analysis a full cross-check of the analysis procedure was carried out, showing very good agreement with the results produced by the primary analysis. This covered both the in-

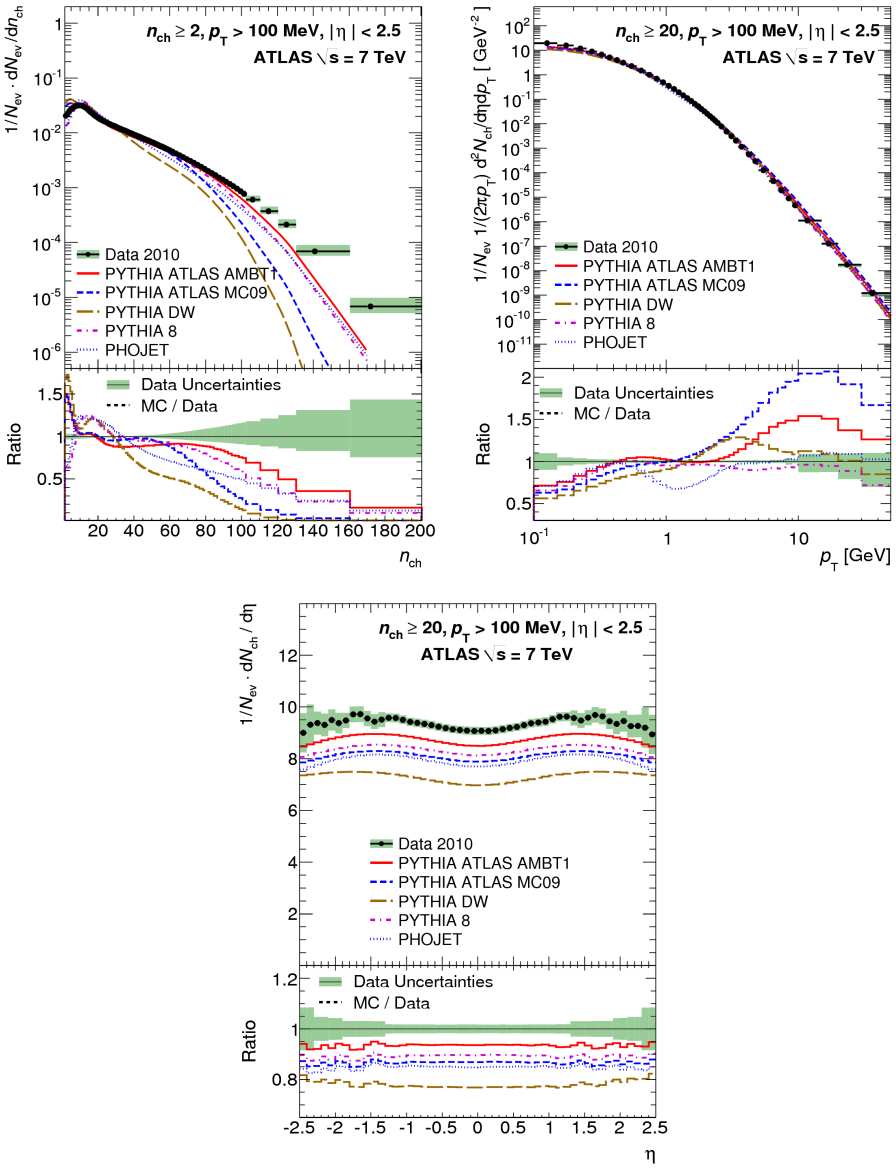

Figure 4.10: The final distributions produced by the analysis at particle level. Shown are the distributions along with the total error on the distribution. For comparison, also shown are the distributions that are predicted by various generators and generator tunes.

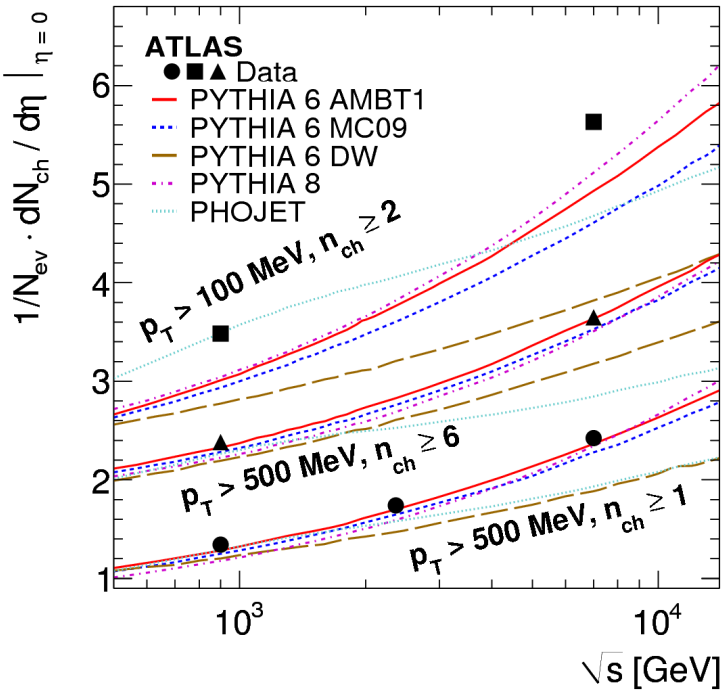

Figure 4.11: Evolution of the average number of tracks per unit pseudorapidity across different CoM energies. Shown here is the distribution at $\eta = 0$ for different phase spaces. Results from different generators and tunes are shown for comparison.

put and basic selection as well as corrections and determination of systematic uncertainties.

Chapter 5

Supersymmetry

5.1 Motivation

SUSY is an additional symmetry imposed on top of the SM, which helps avoid various problems present in the model [27]. It provides a solution to the hierarchy problem [28], the problem of Dark Matter (DM) in certain models [29, 30] as well as a way for the gauge couplings to unite [31]. The theory also features rich phenomenology at the center of mass energy of the LHC.

Due to these attractive features of the theory there is a large effort to find evidence in support of SUSY or to exclude parts of its parameter space using LHC data. One such ATLAS analysis is presented here. In many SUSY models taus are of particular interest as a signature. At the energy scale of the LHC, the production of taus can be significantly boosted with respect to the lighter lepton generations. Analyses targeting final states with taus provide an opportunity to look into such parts of the parameter space specifically. The tau based analysis presented here is interpreted in the context of the Gauge Mediated Symmetry Breaking (GMSB) model in particular, where such regions of parameter space are present.

5.2 SUSY models

The minimal model of SUSY with the most general parametrisation of symmetry breaking is the Minimal Supersymmetric Standard Model (MSSM). The model is minimal in the sense that there is only one set of superpartners for the SM particles. While SUSY in itself does only add few parameters to the SM, the symmetry breaking mechanism is not constrained. Including all possible breaking mechanisms in the model leads to 120 free parameters, making it unwieldy for experimental studies and phenomenology. To create more manageable models the symmetry breaking is constrained to one mechanism and some assumptions are made about the physics at the symmetry

Table 5.1: The parameters ranges of the GMSB grid studied in the analysis.

Parameter	Λ	$\tan\beta$	M_{mess}	N_5	c_{grav}	$\text{sgn}\,\mu$
Value	10 - 80 TeV	2 - 50	250 TeV	3	1	+

breaking scale, e.g. assumptions about the masses of sparticles.

One such model, investigated in the context of this analysis, is the GMSB model [32, 33, 34, 35, 36, 37]. The choice of symmetry breaking mechanism, as implied by the name, is gauge mediation and the Lightest Supersymmetric Particle (LSP) in this model is the gravitino ($\tilde{\text{G}}$). In gauge mediation it is assumed that symmetry breaking occurs in a hidden sector, i.e. through particles not interacting with the SM particles, and the symmetry breaking is communicated to the MSSM sparticles via gauge interactions at loop level. The parameter space consists of six free parameters:

M_{mess}: the mass of the messenger field that mediates symmetry breaking,

Λ: the effective scale at which symmetry breaking occurs,

N_5: the number of SU(5) multiplets involved in symmetry breaking,

c_{grav}: the coupling to gravity, which influences the mass of the gravitino,

$\tan\beta$: the ratio between the Vacuum Expectation Values (VEVs) of the two Higgs doublets and

$\text{sgn}\,\mu$: the sign of the Higgsino mass parameter, μ.

The first four of these parameters deal with the symmetry breaking mechanism and the last two are for the Higgs sector. The parameter Λ gives the overall mass scale of sparticles. The N_5 parameter affects the masses of the sparticles, with gauginos scaling linearly and scalars scaling as $\sqrt{N_5}$. Of particular importance is the $\tan\beta$ parameter, influencing which sparticle is the Next-to-Lightest Supersymmetric Particle (NLSP). Three NLSPs are possible in the parameter space looked at by the analysis; the lighter stau, the right-handed sleptons or all three being degenerate in mass. In the last case they all effectively act as NLSP; this is referred to as the coNLSP region. As it looks at final states with taus, this analysis is most sensitive in the stau region. A further region is present, for low Λ, where the lightest neutralino is the NLSP; however this region is already excluded by OPAL [38].

The parameter ranges for the GMSB grid used in this study are motivated by a study of the ATLAS discovery potential for the GMSB model [39] and can be found in table 5.1.

The splitting of masses between the up and down type quarks is driven by the $\tan\beta$ parameter, regardless of the specific model discussed. This

splitting is driven by electroweak symmetry breaking and is often called the "hyperfine" splitting. At large values of $\tan\beta$ the lightest stau mass is significantly pushed down. In the case of third generation squarks and sleptons the left- and right-handed helicity states are mixed, with larger values of $\tan\beta$ leading to stronger mixing between them. A typical mass spectrum of supersymmetric particles is shown in figure 5.2.

A very common symmetry added in addition to SUSY is R-parity. This is an additional discrete symmetry, conceptually similar to parity, that is even for SM particles and odd for SUSY particles. This results in sparticles always being produced in pairs, as well as requiring that a sparticle always decays to other sparticles and possibly SM particles. This symmetry, while ad-hoc, has the very important consequence of preventing proton decay from SUSY processes, as well as making the LSP a dark matter candidate, as it is stable.

5.3 Production And Decay Modes

In models where R-parity is conserved sparticles must be produced in pairs. At the LHC the dominant mode is expected to be the so-called strong production, where pairs of gluinos or squarks are produced, due to the strong couplings of the colliding partons. An example of such a process is shown in figure 5.1. Weak production modes, direct production of neutralinos or sleptons, are also present though with lower cross-sections.

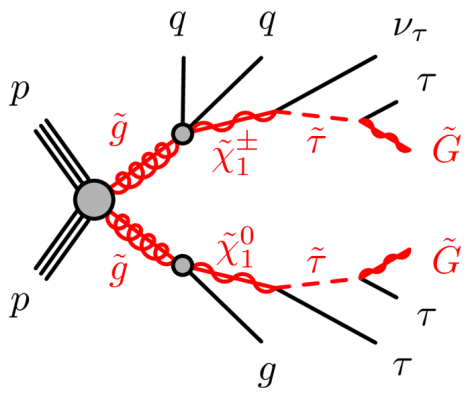

Figure 5.1: An example cascade decay chain in the GMSB model, with strongly produced sparticles and taus in the final state. The chain ends with a decay to gravitino.

The gluinos can only decay into squarks and do so via strong couplings. If kinematically allowed, the preferred decay mode for squarks is via gluino, otherwise they decay via weak couplings into neutralinos or charginos. All

of these decay modes result in the production of jets. The large mass difference between the strongly interacting sparticles and the weakly interacting gauginos and neutralinos means these jets have high energy, see figure 5.2.

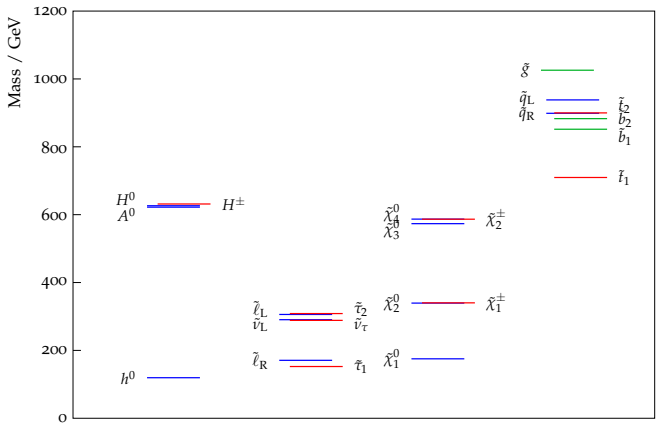

Figure 5.2: The sparticle spectrum of an example GMSB model used, $\Lambda = 50\,\text{GeV}$, $\tan\beta = 20$ and other parameters at $M_{\text{mess}} = 250\,\text{GeV}$, $N_5 = 3$, $c_{\text{grav}} = 1$, $\text{sgn}\,\mu = +$. In columns from left to right; Higgses, sleptons, gauginos and squarks/gluinos. Plots produced using the `PySLHA` [40] python package. The gravitino mass is of the order of eV and is not shown on the plot.

Charginos and neutralinos decay weakly into sleptons or lighter neutralinos until the LSP is reached. The decays of the sleptons typically take place via decay into neutralinos where such decays are kinematically allowed. In this part of the decay chain the production of leptons and gauge bosons is possible, depending on the sparticle mass hierarchy of the model.

Finally, since the LSP of GMSB models is the gravitino, all decays to the LSP happen through gravitational coupling. As this is far smaller than the SM couplings all branching ratios for decay to LSP are small, except for the NLSP where no other decay channels are open.

5.4 Monte Carlo Samples

The MC samples used in the analysis were produced centrally by the ATLAS collaboration. They form a set of all backgrounds that are expected to contribute in the Signal Region (SR).

Top

For top production both $t\bar{t}$ and single top production processes are considered. All primary samples are generated by the `MC@NLO` [41] generator with `HERWIG` [42] showers, except for the t-channel single top production where

the AcerMC [43] generator is used with Pythia [44] showers. The alternative generator for the t-channel is due to problems with unphysical jets from the HERWIG showers. A summary of the samples used can be found in table A.1.

An alternative set of samples generated with AcerMC is used to evaluate generator effects on the background estimate.

W + jets and Z + jets

For W + jets and Z + jets the samples used cover decays into leptons with a separate sample for decay into each lepton flavour. Additionally, the samples are split based on the number of additional associated partons produced, covering all cases from no partons to up to six partons. The samples are produced using Alpgen [45] to generate the process and Jimmy [46] for showering.

A summary of all the samples used can be found in table A.2 for W + jets and table A.3 for Z + jets.

Finally, contributions from Drell-Yan processes are also evaluated using the samples shown in table A.6, also procuced using Alpgen and Jimmy, and as their contribution is relatively small it is estimated directly from MC.

QCD

QCD samples are produced through the Pythia generator. The details of these samples can be found in table A.5. The samples are broken down by the energy range of the produced jets. $E_{\mathrm{T}}^{\mathrm{miss}}$ in such events is due to instrumental effects in jet reconstruction.

Dibosons

One final contribution that is checked is the contribution from diboson production. This contribution is taken as is from simulated data and is produced using the MC@NLO generator. The details of the samples used can be found in table A.4.

Signal samples

The signal samples used can be found in table A.7 and cover a grid in the GMSB parameter space spanned by the parameters $\tan\beta$ and Λ. A model grid refers to a set of model points where each point corresponds to a certain set of parameter values. A separate sample is produced for each model point. The values of the parameters used in the grid can be found in table 5.1. The sparticle mass spectra are produced using ISAJET [47] while the events themselves are produced using the HERWIG generator. The sample for each point in the grid contains 10k events.

5.5 Analysis channels

The analysis presented here is one of four channels in a common analysis. This analysis looks at final states with exactly one tau, high p_{T} jets and high $E_{\mathrm{T}}^{\mathrm{miss}}$ (referred to as the "one-tau" analysis. One further analysis channel looks at final states with two taus, high p_{T} jets and high $E_{\mathrm{T}}^{\mathrm{miss}}$ ("two-tau"). Finally, two analysis channels look at states with a tau and a muon ("tau + muon") or a tau and an electron ("tau + electron"). The result of these four channels are combined in the end to produce one common result for the entire analysis. What follows is the description of the procedures and results from the one-tau channel as well as the final statistical combination with the other three channels.

5.6 Event selection

The analysis uses the full 4.7 fb^{-1} 7 TeV CoM dataset from 2011. Events with sparticle production are characterized by a high $E_{\mathrm{T}}^{\mathrm{miss}}$, originating from the undetected heavy LSP, and associated high-p_{T} jets. The analysis therefore uses data from the `JetTauEtMiss` stream, which contains events triggered by $E_{\mathrm{T}}^{\mathrm{miss}}$, jet and tau signatures.

Trigger selection on 2011 collision data

The trigger chain `EF_j75_a4tc_EFFS_xe45_loose_noMu` is required to have fired for data taking periods B2–I (i.e. run numbers $\leq$ 186493), recording events with at least one jet above 75 GeV and $E_{\mathrm{T}}^{\mathrm{miss}}$ above 45 GeV. For periods J–M the $E_{\mathrm{T}}^{\mathrm{miss}}$ threshold has been raised to 55 GeV, represented by the trigger chain `EF_j75_a4tc_EFFS_xe55_noMu`. In both cases these were unprescaled triggers with the lowest available p_{T} and $E_{\mathrm{T}}^{\mathrm{miss}}$ thresholds. An explanation of these triggers can be found in section 2.7. The trigger requirement is only applied to data.

One of the background estimation techniques, the correction of the rate of the Z + jets background events, studies identified Z decays to muons, and for that purpose uses the muon stream with the trigger `EF_mu15_mu10_EFFS` for periods B2–I, and `EF_mu15_mu10_EFFS_medium` thereafter.

Baseline event selection

The analysis baseline event selection is to select only events which are suitable for the analysis. This means passing trigger requirements, data quality requirements and a selection of the physics objects required by the analysis. The physics objects referred to here are defined in section 2.6. The baseline event selection involves the following steps in the order given:

- A preselection of data from the GRL rejects p–p collision data with problematic detector conditions, as described in section 3.3. It ensures that only well reconstructed physics objects enter the analysis.

- For certain events the LAr calorimeter reports an error condition. Such error conditions act on single events only and do not compromise the whole LB or run. The luminosity calculation accounts for these and about 0.28% of the total integrated luminosity is lost after this selection.

- Select events with a primary vertex with at least four associated tracks. This ensures that a hard process took place in the event.

- While the trigger requirements apply only to data, kinematic selections are imposed to jet p_{T} and $E_{\mathrm{T}}^{\mathrm{miss}}$ in both data and MC events. At least two jets must be selected, one with $p_{\mathrm{T}} > 130\,\mathrm{GeV}$ and a second with $p_{\mathrm{T}} > 30\,\mathrm{GeV}$, as well as $E_{\mathrm{T}}^{\mathrm{miss}} > 130\,\mathrm{GeV}$. This selection means only events in the trigger plateau region are selected, where the trigger efficiency is close to 100%, see figure 5.3. For data taking periods L–M the last selection is raised to $E_{\mathrm{T}}^{\mathrm{miss}} > 150\,\mathrm{GeV}$.

- A veto for events containing muons or electrons is applied.

- Finally, events pass the selection if a tau-lepton is reconstructed with $p_{\mathrm{T}} > 20\,\mathrm{GeV}$ and being identified as a tau, using the "tight" jet rejection requirements and "tight" electron rejection requirements [15]. The presence of additional "loose" tau candidates disqualifies the event from selection.

- A veto of events where "bad" jets are found after overlap removal. These are jets which originate from beam background or detector effects and jets which have mismeasured energy. Additionally, events where jets or taus received large corrections due to the LAr hole treatment are rejected. The procedure is described in detail in [48].

The rejection of events with an additional tau candidate or events that contain muon or electron candidates ensures that the one-tau analysis channel is orthogonal to the two tau and tau plus muon/electron channels, making it possible to statistically combine the results of all four channels in a straightforward manner.

Background rejection and signal selection

After the events pass the trigger and baseline event selection, the following additional selections are applied to reject as much of the background as possible, while preserving the signal:

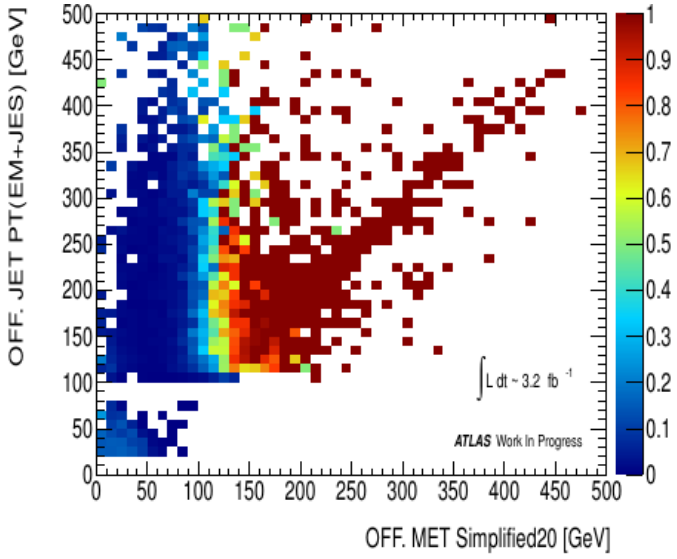

Figure 5.3: The efficiency of the trigger for the 2011 run as a function of $E_{\mathrm{T}}^{\mathrm{miss}}$ versus jet p_{T}. Of note is the plateau region, where the trigger efficiency becomes uniform; this trigger achieves almost 100% efficiency there.

- $\Delta\phi_{\mathrm{min}} > 0.3$,
- $E_{\mathrm{T}}^{\mathrm{miss}}/m_{\mathrm{eff}} > 0.3$,
- $m_{\mathrm{T}} > 110\,\mathrm{GeV}$,
- $H_{\mathrm{T}} > 775\,\mathrm{GeV}$.

These variables are introduced in section 2.6 and define the used SR in which the SUSY signal looked at is enhanced compared to background. This region is kept blind (i.e. the data in this region are not looked at) until the background estimation is finalised. This is done to avoid biasing the selection by looking at the data, which are subject to statistical fluctuations. This makes the background estimation even more crucial, as there is no comparison between data and MC in the SR until the final results are ready to be produced.

The first two selections are designed to reject QCD background. The m_{T} selection is designed to remove backgrounds containing a W boson decaying to a tau and a neutrino, which is the dominant non-QCD background in this analysis. The H_{T} selection is designed to suppress the remaining backgrounds, primarily W + jets, top, $Z \to \nu\nu$ and dibosons.

The H_{T} selection value is chosen by optimising the expected exclusion limit in the GMSB grid. This is done by varying the value of the H_{T} cut and calculating the expected limit on the model cross section for the GMSB

points with cross section $0.05\,\text{pb} < \sigma < 0.5\,\text{pb}$. Model points with cross sections in this range are close to the expected exclusion reach. The GMSB points used for the optimisation are listed in table 5.2. Figure 5.4 shows the optimisation results, yielding an optimal selection of $H_\text{T} > 775\,\text{GeV}$.

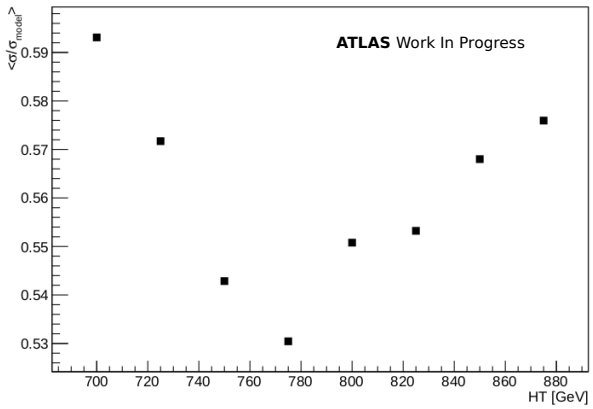

Figure 5.4: Optimisation of the H_T selection to define the signal region of the one-tau analysis. The y-axis shows the cross section which can be excluded at 95% CL_s relative to the cross section of the tested GMSB models, averaged over all models listed in table 5.2.

5.7 Control regions

In order to minimise the effect of uncertainties on the background estimation the number of events in each of the dominant background contributions is normalised to data. To do this Control Regions (CRs) are defined where each background component is enhanced. The techniques used to normalise each background source are outlined in section 5.8.

5.7.1 W + jets and top

The CRs for the W + jets and top backgrounds are defined by the baseline selection requirements, see section 5.6, and an additional selection on $m_\text{T} < 80\,\text{GeV}$, to keep only taus coming from W decays. Separation between top and W + jets is achieved via b-tagging. Events with b-tagged jets form the top CR and all others the W + jets CR. This criterion is effective in classifying these two contributions as shown in figure 5.6.

As the kinematics and simulation of fake taus is different from true taus (fake taus are typically misidentified jets) a second set of CRs is used to get Scale Factors (SFs) for processes involving fake taus. The region with

Sample	Λ [TeV]	$\tan\beta$	σ [pb]	Sample	Λ [TeV]	$\tan\beta$	σ [pb]
137934	40	2	0.39	142573	45	25	0.22
137935	40	5	0.42	142574	45	30	0.22
137936	40	10	0.43	142575	45	35	0.23
137937	40	15	0.43	142576	45	40	0.26
137938	40	20	0.44	137944	50	2	0.09
137939	40	25	0.44	137945	50	5	0.11
137940	40	30	0.45	137946	50	10	0.11
137941	40	36	0.48	137947	50	15	0.11
142568	45	2	0.18	137948	50	20	0.11
142569	45	5	0.21	137949	50	30	0.12
142570	45	10	0.21	137950	50	40	0.13
142571	45	15	0.21	137951	50	50	0.25
142572	45	20	0.22	137959	60	50	0.06

Table 5.2: GMSB points that are included in the optimisation of the H_{T} selection for the one-tau analysis.

$80\,\mathrm{GeV} < m_{\mathrm{T}} < 110\,\mathrm{GeV}$ is used. An additional selection on $H_{\mathrm{T}} < 775\,\mathrm{GeV}$ is made to ensure separation with the SR.

These CRs are summarised in figure 5.5, showing the separation between them and the SR.

5.7.2 Z + jets

In the case of the Z + jets estimation the SF is derived using $Z \to \mu\mu$ processes as well as data using di-muon triggers to normalise the MC to data. In defining this region a requirement is placed for two muons which have invariant mass within the Z mass window $66\,\mathrm{GeV} < M(\mu^+, \mu^-) < 116\,\mathrm{GeV}$. These muons are required to pass the baseline SUSY muon identification criteria.

5.8 Background estimation

The two primary backgrounds for this study are the W + jets and top production. These form a big contribution both because of their high cross-section but also due to the decay of Ws into neutrinos, giving a real $E_{\mathrm{T}}^{\mathrm{miss}}$ contribution.

The Z + jets background is also important in the study, particularly the decays $Z \to \nu\nu$ + jets, where one of the jets is misidentified as a tau and the neutrinos provide the $E_{\mathrm{T}}^{\mathrm{miss}}$ signature. This background contribution is estimated in the Z + jet CR

Multijet processes do not contribute much in the SR but need to be

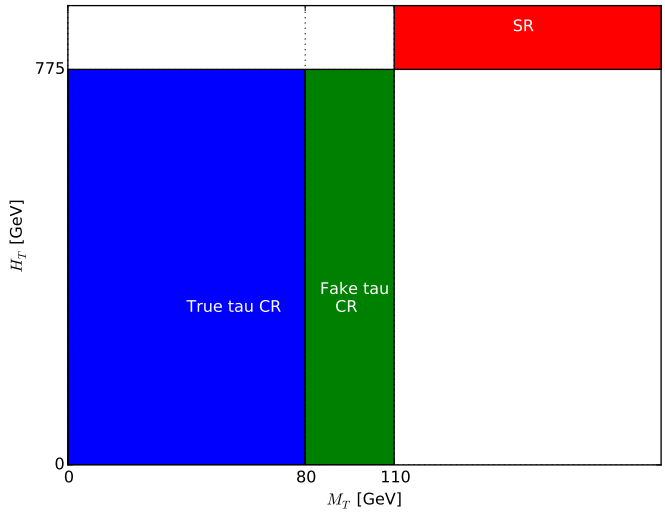

Figure 5.5: Plot of the defined CRs and SR for the analysis in the m_{T} and H_{T} space. A m_{T} selection splits the regions into true and fake tau dominated, while a H_{T} selection separates them from the SR. The CRs can be further split into W and top dominated, based on the b-tagged jet multiplicity in the event.

estimated as the uncertainty on the contamination is very large if MC is used alone. Diboson production and Drell-Yan processes are also considered, though of lesser importance in the final signal region.

5.8.1 Top background with a true tau estimate

In the case of the top background with true taus, the background estimation is done through a template fit. The variable used to split between the top and the W backgrounds is the number of b-tagged jets in the event, which is larger in the case of top, due to the $t \to W^{\pm}, b^{\mp}$. Templates of the number of b-tagged jets are produced from MC for top processes ($t\bar{t}$ and single top production) and a combined template for the other backgrounds using events from the true tau CR. Figure 5.6 shows plots of the templates used. These templates are then fitted to the b-tagged jet multiplicity from data events in the true tau CR. The fit results in a fraction of data events accounted for by each template, the resulting fit is shown in figure 5.7. The total number of events in the CR is then constrained by the data and the data/MC fraction gives the total number of events from top, from which a SF can be computed to correct the MC estimate for top. The fraction to all other events is not used further.

From the fit a SF of

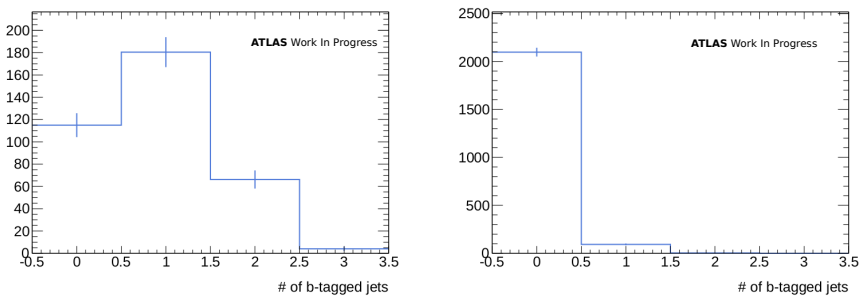

Figure 5.6: The multiplicity of b-tagged jets for samples with top production (right) and for all other contributions (left) in the top/W CR.

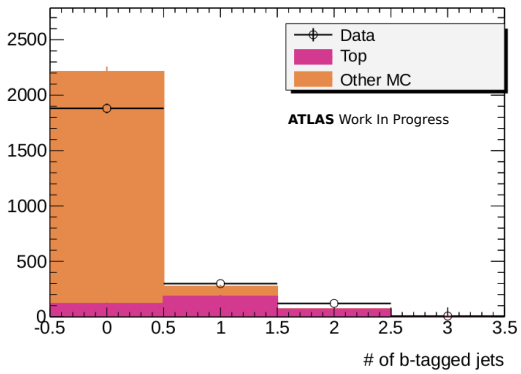

Figure 5.7: The multiplicity of b-tagged jets in data along with the final fit of the contributions from top and other sources.

Region	Scale Factor ($\omega_{\text{top}}^{\text{true}}$)
$\lvert\eta\rvert < 0.8$	1.46 ± 0.08
$0.8 < \lvert\eta\rvert < 1.6$	1.35 ± 0.13
$1.6 < \lvert\eta\rvert$	1.60 ± 0.25

Table 5.3: The true tau top SF obtained for the different regions in η.

$$\omega_{\text{top}}^{\text{true}} = 1.39 \pm 0.08^{\text{stat.}}\ {}^{+0.06}_{-0.08}\ ^{\text{syst.}}$$

is found.

To cross-check the stability of the method the process is repeated also using different slices of η and computing the SF in each slice. The results of this check are shown in table 5.3 and good agreement is found, within statistical uncertainties.

5.8.2 W + jets background with a true tau estimate

The W + jets background estimation uses the asymmetry in the charge of Ws produced in LHC. This asymmerty arises due to the p-p collisions in the LHC. As the colliding protons consist of two up and one anti-down valence quarks the production of W^+ through an up and anti-down quark interaction is more likely than W^- through down and anti-up; as in the former case one of the quarks can be a valence quark. This particular effect is only visible for W production. The production of top quarks is mainly in pairs, thus no such effect is present. This means that it is possible to estimate the W content in data by measuring this charge asymmetry. The final SF is determined by finding the value which results in identical asymmetry in data and MC.

First the ratio of positive to negative taus, r_{MC}, needs to be etracted in the W true tau CR from W + jets and WZ MC. These MC samples are used as these are the ones that contribute to this measurement. Additional contributions can come from single top production but this is a much smaller effect. With this ratio and the number of positively and negatively charged W candidate events from data, D^+ and D^- respectively, the number of true Ws can be estimated as:

$$N_W = N_W^+ + N_W^- = \frac{r_{\text{MC}} + 1}{r_{\text{MC}} - 1}\left(D^+ - D^-\right) \quad . \tag{5.1}$$

Contributions due to fake taus are naturally suppressed, since fake taus do not have a particular preference towards a certain charge, meaning that they cancel out once the subtraction is carried out.

The value of r_{MC} found in W + jets and WZ MC events in the W/top CR is:

$$r_{\mathrm{MC}} = 2.15 \pm 0.05 \quad ,$$

In the same CR from data:

$$D^{+} - D^{-} = 502.$$

These result in a SF for the true W contribution of:

$$\omega_{\mathrm{W}}^{\mathrm{true}} = 0.75 \pm 0.04^{\mathrm{stat}} \pm 0.03^{\mathrm{syst}} \quad .$$

5.8.3 Combined top and W estimation

For these two backgrounds a combined method is also considered, relying on the information about true and fake taus of the background categories in the two CRs. The SFs for true and fake taus are kept separate since these come from different sources (fake taus are typically misidentified jets), meaning that any possible mismodelling of the two in MC can be different. This results in four input variables and four variables to estimate the scale factors required to make the MC estimates match the data in the two CRs. This method of estimation is commonly referred to as the "matrix method".

$$\begin{pmatrix} N_{\mathrm{W,true}}^{\mathrm{WT1}} & N_{\mathrm{W,fake}}^{\mathrm{WT1}} & N_{\mathrm{top,true}}^{\mathrm{WT1}} & N_{\mathrm{top,fake}}^{\mathrm{WT1}} \\ N_{\mathrm{W,true}}^{\mathrm{WT2}} & N_{\mathrm{W,fake}}^{\mathrm{WT2}} & N_{\mathrm{top,true}}^{\mathrm{WT2}} & N_{\mathrm{top,fake}}^{\mathrm{WT2}} \\ N_{\mathrm{W,true}}^{\mathrm{WT3}} & N_{\mathrm{W,fake}}^{\mathrm{WT3}} & N_{\mathrm{top,true}}^{\mathrm{WT3}} & N_{\mathrm{top,fake}}^{\mathrm{WT3}} \\ N_{\mathrm{W,true}}^{\mathrm{WT4}} & N_{\mathrm{W,fake}}^{\mathrm{WT4}} & N_{\mathrm{top,true}}^{\mathrm{WT4}} & N_{\mathrm{top,fake}}^{\mathrm{WT4}} \end{pmatrix} \begin{pmatrix} \omega_{W}^{\mathrm{true}} \\ \omega_{W}^{\mathrm{fake}} \\ \omega_{\mathrm{top}}^{\mathrm{true}} \\ \omega_{\mathrm{top}}^{\mathrm{fake}} \end{pmatrix} = \begin{pmatrix} N_{\mathrm{data}}^{\mathrm{WT1}} - N_{\mathrm{Oth.MC}}^{\mathrm{WT1}} \\ N_{\mathrm{data}}^{\mathrm{WT2}} - N_{\mathrm{Oth.MC}}^{\mathrm{WT2}} \\ N_{\mathrm{data}}^{\mathrm{WT3}} - N_{\mathrm{Oth.MC}}^{\mathrm{WT3}} \\ N_{\mathrm{data}}^{\mathrm{WT4}} - N_{\mathrm{Oth.MC}}^{\mathrm{WT4}} \end{pmatrix} .$$

In order to correct for other contributions all MC samples that are not contributing to the estimated quantities are subtracted from MC. Where applicable SFs are applied to the MC estimates.

This allows us to estimate the vector $\vec{\omega}$, which contains the SFs for each CR with true and fake taus, by inverting the matrix.

$$\begin{pmatrix} \omega_{W}^{\mathrm{true}} \\ \omega_{W}^{\mathrm{fake}} \\ \omega_{\mathrm{top}}^{\mathrm{true}} \\ \omega_{\mathrm{top}}^{\mathrm{fake}} \end{pmatrix} = \begin{pmatrix} 0.91 \pm 0.03^{\mathrm{stat}} + 0.05^{\mathrm{syst}} \\ 0.32 \pm 0.28^{\mathrm{stat}} + 0.17^{\mathrm{syst}} \\ 1.32 \pm 0.10^{\mathrm{stat}} + 0.13^{\mathrm{syst}} \\ 1.92 \pm 0.41^{\mathrm{stat}} + 0.22^{\mathrm{syst}} \end{pmatrix} \quad . \tag{5.2}$$

This method provides a cross-check of the true tau W and top SF. In the case of the top the two results are in agreement within statistical uncertainties. As this is not the case for the true tau W the difference between

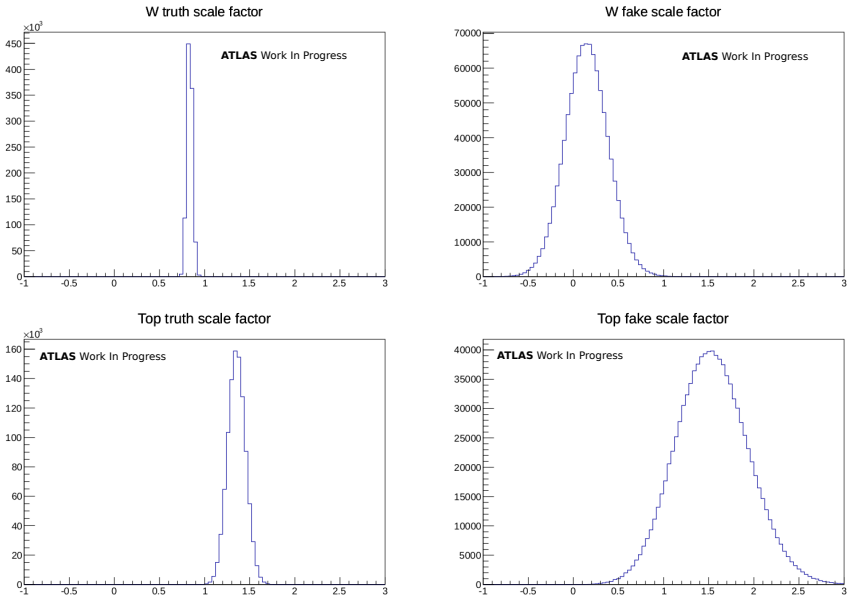

Figure 5.8: The scale factors obtained via the matrix method for the W + jets and top true and fake tau contributions. The distributions are obtained using toy MCs.

the two SFs is taken as an additional systematic uncertainty. For the fake tau SFs this is the only determination done. The error in the number of events in each region is also taken into account using toy MC. The output distributions where these uncertainties are taken into acount are shown in figure 5.8.

5.8.4 Z + jets

The presence of Z + jets as one of the backgrounds in the SR is also estimated from a data-driven technique. First it is studied that the main contribution of Z + jets to the signal region actually comes from events where the Z decays to a pair of neutrinos and contributes fully to the observed $E_{\mathrm{T}}^{\mathrm{miss}}$. However, $\mathrm{Z} \to \nu\nu$ decays can not be studied directly with high purity. Also, while Z + jets production with the Z boson decaying to ee or $\mu\mu$ has been measured by ATLAS, this analysis operates in a more extreme kinematic regime compared to the ATLAS results, so these can not be directly applied either. The Z + jets contribution is therefore estimated from the data by measuring the data/MC ratio from $\mathrm{Z} \to \mu\mu$ decays in a dedicated CR and scaling the number of all Z + jets events from MC in the SR with that factor.

$$Z_{\nu\nu}^{\mathrm{Data,SR}} = Z_{\nu\nu}^{\mathrm{MC,SR}} \frac{Z_{\mu^+\mu^-}^{\mathrm{Data,CR}}}{Z_{\mu^+\mu^-}^{\mathrm{MC,CR}}} \,. \tag{5.3}$$

Sensitivity to $Z \to \nu\nu$ decays is emulated by using a modified $E_T^{miss}*$ in the analysis where the transverse momenta of muons from the Z decay are made part of the missing energy vector:

$$E_T^{miss}* = \left|\left(\vec{E}_T^{miss} + \vec{p}_\mu + \vec{p}_\mu\right)_T\right| \tag{5.4}$$

For simplicity, in this analysis only the $\mu^+\mu^-$ channel is considered. The baseline event selection of section 5.6 is substantially altered to obtain a high statistics Z + jets control sample.

The selection starts from the `Muon` stream instead of `JetTauEtMiss` and requires the trigger: `EF_mu15_mu10_EFFS` for data taking periods B2–I and `EF_mu15_mu10_EFFS_medium` for periods J–M. After GRL and vertex requirements it selects only events with two opposite signed isolated muons with $|\eta| < 2.4$, $p_T > 20\,\text{GeV}$ and with invariant mass within the range $66\,\text{GeV} < M(\mu^+, \mu^-) < 116\,\text{GeV}$. To make the CR signal-like at least 2 jets are required with $p_T(\text{jet}_1) > 130\,\text{GeV}$ and $p_T(\text{jet}_2) > 30\,\text{GeV}$ and a high "missing" transverse energy $E_T^{miss}* > 130\,\text{GeV}$ (150 GeV for data taking periods L–M, to account for the different trigger plateau requirements). Figure 5.9 shows the data and MC contributions to the CR as function of the dimuon invariant mass for two different muon p_T selections. The MC predicts a very high Z purity but overestimates the number of events in the Z + jets control sample. A SF of 0.81 ± 0.01 is derived from these studies.

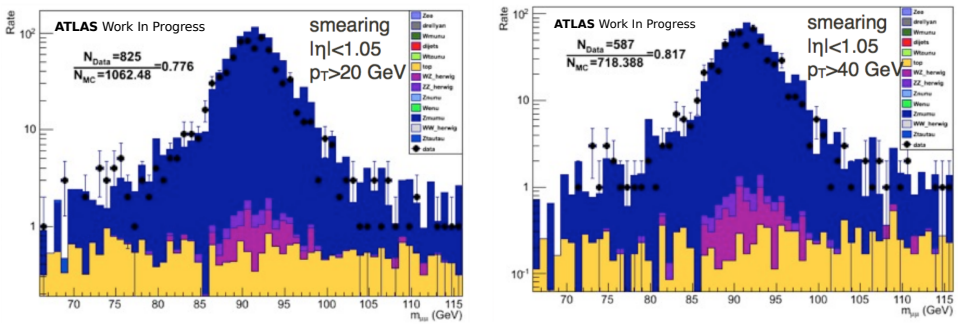

Figure 5.9: Di-muon invariant mass distribution for events from the Z + jets CR. The difference in numbers of event between data and MC gives rise to a scale factor. The right distribution tests the agreement for a more stringent requirement on the Z decay muons of $p_T > 40\,\text{GeV}$.

5.8.5 QCD estimation

The method used for QCD estimation is the so-called ABCD method, which allows a data-driven estimate of a background rate. Events are selected by a pair of cuts in a plane of two uncorrelated variables, such that both of the selections enhance the signal-to-background ratio.

Scaling	One-tau	Two-Tau	Tau + Muon	Tau + Electron
$\omega^{\mathrm{W}}_{\mathrm{true}}$	0.75 ± 0.04	0.74 ± 0.02	-	-
$\omega^{\mathrm{t}}_{\mathrm{true}}$	1.39 ± 0.08	1.17 ± 0.03	-	-
$\omega^{\mathrm{Z}}_{\mathrm{true}}$	0.81 ± 0.01	0.96 ± 0.38	-	-
$\omega^{\mathrm{W}}_{\mathrm{fake}}$	0.32 ± 0.28	0.65 ± 0.32	0.58 ± 0.02	0.61 ± 0.01
$\omega^{\mathrm{t}}_{\mathrm{fake}}$	1.92 ± 0.41	0.89 ± 0.23	0.84 ± 0.16	0.84 ± 0.14

Table 5.4: Comparison of the scale factors for W + jets, Z + jets and top background contributions derived by the different analyses.

	Extra Loose τ	Nominal τ
$\Delta\phi_{\mathrm{min}} < 0.3$	Control region A	Control region B
$\Delta\phi_{\mathrm{min}} > 0.3$	Control region C	Signal region D

Table 5.5: Definitions of QCD regions used in the ABCD method for the one-tau analysis.

The two variables used here are the tau identification tightness and $\Delta\phi_{\mathrm{min}}$ so that an event sample with high QCD contamination is separated into four regions, these are shown in table 5.5. Figure 5.10 shows a scatterplot of the tau BDT score against $\Delta\phi_{\mathrm{min}}$ for QCD MC after the m_{T}^{τ} selection, but skipping the QCD suppressing selection and final H_{T} selection. In this definition the regions A, B and C are QCD enriched with small signal contamination. Using the number of events in these regions it is possible to estimate the number of QCD events in region D. The tau identification becomes a background discriminator variable by adding an "extra loose tau" working point to the already defined nominal tau definition from section 2.6. An extra loose tau candidate has the nominal tau ID selection with the exception of the BDT identification; if the event features several such taus,

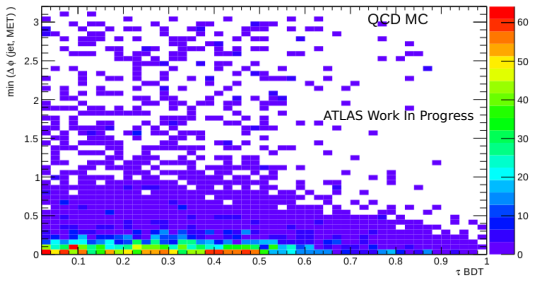

Figure 5.10: Plot of the variables used to define the ABCD regions and before the final H_{T} selection in the one-tau analysis for QCD MC. The two variables should be independent of each other in order for the ABCD method to work.

one of them is picked at random. An extra loose tau candidate is only picked as long as it does not overlap with the two leading jets in the event. These extra loose tau candidates are then used in place of the nominal taus in the event selection. The sample is split into events where an extra loose tau is identified but would not pass the nominal tau definition and events passing only the tighter nominal tau identification. The variable $\Delta\phi_{\text{min}}$, is sensitive to events where $E_{\text{T}}^{\text{miss}}$ originates largely from a single mis-measured jet instead of a real undetected particle.

Event selection for the ABCD method

The baseline event selection from section 5.6 is applied. To improve the statistical power of the method the $E_{\text{T}}^{\text{miss}}/m_{\text{eff}}$ selection and the final selection on H_{T} is not applied. An additional selection on $E_{\text{T}}^{\text{miss}}/m_{\text{eff}} < 0.3$ is made for region C, in order to reduce the non-QCD contamination, making the method less affected by uncertainties in non-QCD SFs.

A significant contamination from non-QCD events is observed in all CRs except for region A, as shown in figure 5.11.

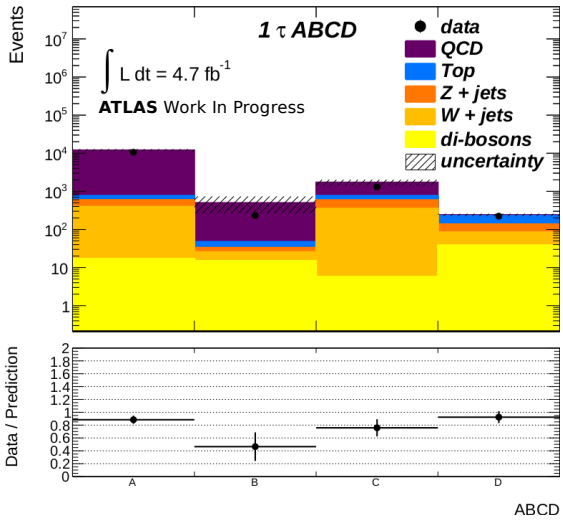

Figure 5.11: Summary of background composition in the four samples defined by extra loose/nominal tau ID and the $\Delta\phi_{\text{min}}$ selection for the ABCD method.

Figures 5.12 and 5.13 show the H_{T} and $E_{\text{T}}^{\text{miss}}/m_{\text{eff}}$ distributions in regions A-C.

Separating backgrounds inside the ABCD method

Other non-QCD backgrounds contribute to the observed number of events in the CRs A–C region, this effect needs to be corrected. Two methods are studied for this correction, labelled *subtraction method* and *likelihood method*. Details of these methods are presented in what follows.

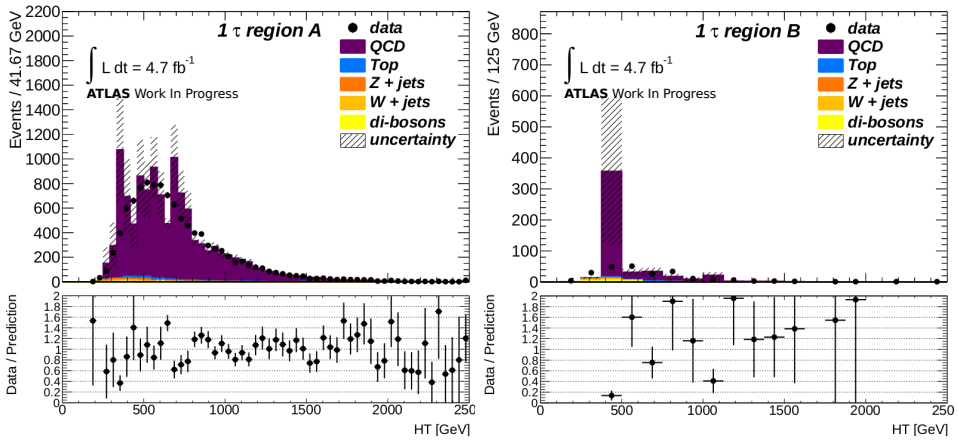

(a) A

(b) B

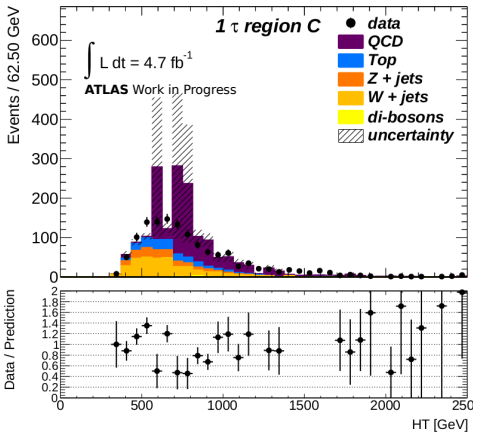

(c) C

Figure 5.12: m_{eff} distributions in regions A, B and C for the one-tau analysis, showing good agreement between data and MC, in the areas where it is possible to compare. Certain bins have large statistical unertainties due to the high weight of the events contributing to them.

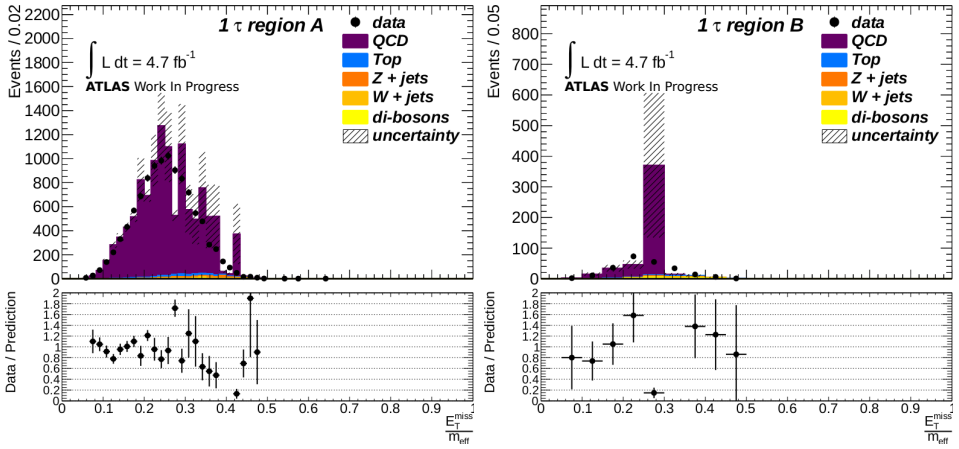

(a) A

(b) B

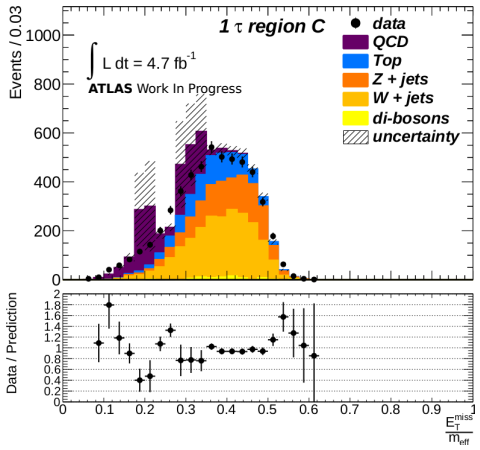

(c) C. No selection applied on $E_{\mathrm{T}}^{\mathrm{miss}}/m_{\mathrm{eff}}$

Figure 5.13: $E_{\mathrm{T}}^{\mathrm{miss}}/m_{\mathrm{eff}}$ distributions in regions A, B and C for the one-tau analysis, showing good agreement between data and MC, in the areas where it is possible to compare. Certain bins have large statistical unertainties due to the high weight of the events contributing to them.

- The *subtraction method* is a simple subtraction of the non-QCD MC from the data in the regions A–C, using the scale factors obtained for the top and vector boson backgrounds from the data-driven methods in the following sections. Scale factors for true and fake non-QCD contributions are dependent on the tau ID. The influence of the uncertainty of the SFs on the method is estimated by scaling the extra loose tau region and not applying the SFs to this region, and adding the difference of the results as an additional systematic uncertainty of the method.

- The other way incorporates the non-QCD background by additional terms in a *likelihood function method*. This way is more robust if the amount of background to be subtracted is comparable to the number of events observed in one or more of the regions.

Subtraction method as part of background treatment in the ABCD method

The subtraction

$$N_{\mathrm{A,B,C}}^{\mathrm{QCD}^*} = N_{\mathrm{A,B,C}}^{\mathrm{data}} - N_{\mathrm{A,B,C}}^{\mathrm{non-QCD}} \tag{5.5}$$

allows the number of QCD events in the signal region D, for $E_{\mathrm{T}}^{\mathrm{miss}}/m_{\mathrm{eff}} < 0.3$, to be estimated by

$$N_{\mathrm{D}}^{\mathrm{QCD}^*} = \frac{N_{\mathrm{B}}^{\mathrm{QCD}^*}}{N_{\mathrm{A}}^{\mathrm{QCD}^*}} N_{\mathrm{C}}^{\mathrm{QCD}^*} \tag{5.6}$$

To get the number of estimated QCD events in the signal region used in the real event selection this number has to be scaled by the ratio of events with $E_{\mathrm{T}}^{\mathrm{miss}}/m_{\mathrm{eff}} < 0.3$ and the final selection on H_{T} and $E_{\mathrm{T}}^{\mathrm{miss}}/m_{\mathrm{eff}} > 0.3$. This ratio may be taken from the QCD-dominated region A, provided that these variables are independent of tau ID and $\Delta\phi_{\mathrm{min}}$. This yields $N_{\mathrm{D}}^{\mathrm{QCD}^*} = 9.9 \pm 1.0^{\mathrm{stat}}$ and in the final signal region $N_{\mathrm{D,\ E_T^{miss}/m_{eff}>0.3\ \&\ H_T>775\,GeV}}^{\mathrm{QCD}^*} = N_{\mathrm{SR}}^{\mathrm{QCD}^*} = 0.13 \pm 0.03^{\mathrm{stat}}$ when the W, Z and top background scale factors are not yet applied to the regions A and C (extra loose tau). This result is consistent with the ratios from the other QCD-enriched regions, the statistically limited regions B (only one event passes $E_{\mathrm{T}}^{\mathrm{miss}}/m_{\mathrm{eff}} > 0.3$) and C. It is also consistent with result obtained when varying the tau definition, by using BDT "loose" taus as well as an even looser tau definition (tau candidates with basic kinematic selection, and charge $< |3|$ and $n_{tracks} < |6|$ with and without lepton vetoes, here labelled "extra loose").

The final QCD estimate is calculated from the extra loose regions, where non-QCD contributions have been scaled using the SFs obtained in sections 5.8.1-5.8.4. These include the W, Z and top SFs found in table 5.4,

as found by the other background estimation methods in the analysis. This yields $N_{\mathrm{SR}}^{\mathrm{QCD}^*} = 0.17 \pm 0.04^{\mathrm{stat}}$. The difference between the two numbers are taken as an additional systematic uncertainty on the method. Figure 5.14 shows the numbers of estimated QCD events in the SR from this method for different values of QCD reducing selections on $\Delta\phi_{\mathrm{min}}$ and $E_{\mathrm{T}}^{\mathrm{miss}}/m_{\mathrm{eff}}$.

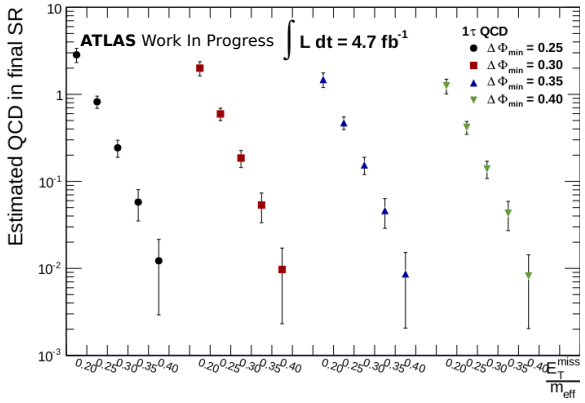

Figure 5.14: Shows number of QCD events estimated from the ABCD subtraction method in the final SR for different selection values on $\Delta\phi_{\mathrm{min}}$ and $E_{\mathrm{T}}^{\mathrm{miss}}/m_{\mathrm{eff}}$.

Likelihood method as part of background treatment in the ABCD method

The background correction via likelihood function works as follows: the predicted rates for the non-QCD background components are denoted here by $\mu_{\mathrm{D;A,B,C}}^{\mathrm{nQCD}}$ and are taken from MC with appropriate SFs applied, given in table 5.4 (no scaling of extra loose taus). A possible signal contribution in region D is denoted by μ. The signal leakage into the other regions is expressed in terms of $\mu_{\mathrm{A,B,C}}$ and a signal acceptance factor into this region taken from MC in a sample GMSB signal. Then there is the "unknown" QCD background which is completely data driven. Denoting the component in the search region D as μ^{QCD}, we describe the ABCD-relation between the other three components with two additional nuisance parameters τ_B and τ_C. The estimated rates in the 4 regions are thus described by:

$$
\begin{aligned}
\mu_A &= \mu_{\mathrm{A}} + \mu_A^{\mathrm{nQCD}} + \mu^{\mathrm{QCD}}\tau_B\tau_C \\
\mu_B &= \mu_{\mathrm{B}} + \mu_B^{\mathrm{nQCD}} + \mu^{\mathrm{QCD}}\tau_B \\
\mu_C &= \mu_{\mathrm{C}} + \mu_C^{\mathrm{nQCD}} + \mu^{\mathrm{QCD}}\tau_C \\
\mu_D &= \mu + \mu_D^{\mathrm{nQCD}} + \mu^{\mathrm{QCD}}
\end{aligned}
$$

The likelihood function is the product of the four likelihoods for the counting experiments in the four regions:

$$L(n_A, n_B, n_C, n_D|\mu, \theta_\mu) = \prod_{\mathrm{i=A,B,C,D}} \frac{e^{-\mu_\mathrm{i}} \mu_i^{\mathrm{n_i}}}{n_i!}$$

The maximum likelihood fit to data yields $\mu^{\mathrm{QCD}} = 9.9 \pm 1.0$. This yields an estimate of 0.13 ± 0.03 events in the region with $E_{\mathrm{T}}^{\mathrm{miss}}/m_{\mathrm{eff}} > 0.3$ and $H_{\mathrm{T}} > 775\,\mathrm{GeV}$ using the ratio of events in region A as for the subtraction method and no scaling of the extra loose tau region. This is the same result as the one obtained from the subtraction approach, which shows that the simple treatment (by subtraction) works well.

5.9 Events in SR after selection

The number of events after each selection, as outlined in section 5.6, for the SM backgrounds is shown in table 5.7, where the SFs obtained in section 5.8 have been applied. For comparison between MC and data the total sum of the MC output is compared to data at each step in the cutflow, shown in table 5.6.

After cut	SM	Data
τ (no overlap 2 τ)	3656 ± 256	3751
$\Delta\phi_{\mathrm{min}} > 0.3$	3028 ± 120	3370
$E_{\mathrm{T}}^{\mathrm{miss}}/m_{\mathrm{eff}} > 0.3$	2441 ± 99	2673
$m_{\mathrm{T}}^{\tau} > 110\,\mathrm{GeV}$	178 ± 22	184
$H_{\mathrm{T}} > 775\,\mathrm{GeV}$	1.31 ± 0.37	4

Table 5.6: Cut-flow for the kinematic selections defining the SR of the one-tau analysis after the baseline selection. Shown errors are statistical only. The sum of all Standard Model background processes is compared to the data. The value of 1.31 ± 0.37 expected events is composed of the predicted events from the corrected top quark, W + jets and Z + jets MC and the events for QCD background estimated from the data.

After cut	Top	W + jets	Z + jets	Di-boson	QCD	Drell-Yan
1 τ (no overlap 2 τ)	890 ± 55	2045 ± 114	243 ± 15	9.0 ± 1.0	456 ± 222	4.1 ± 1.2
$\Delta\phi_{\mathrm{min}} > 0.3$	834 ± 50	1951 ± 107	205 ± 14	7.8 ± 0.9	28 ± 10	2.2 ± 0.9
$E_{\mathrm{T}}^{\mathrm{miss}}/m_{\mathrm{eff}} > 0.3$	680 ± 41	1593 ± 89	157 ± 13	5.8 ± 0.6	3.7 ± 3.6	1.5 ± 0.8
$m_{\mathrm{T}}^{\tau} > 110\,\mathrm{GeV}$	90 ± 14	34 ± 15	52 ± 8	1.5 ± 0.3	< 3.5	< 0.36
$H_{\mathrm{T}} > 775\,\mathrm{GeV}$	0.61 ± 0.25	0.30 ± 0.16	0.22 ± 0.22	< 0.05	0.17 ± 0.04	< 0.36

Table 5.7: Number of events after each step in the kinematic selection defining the SR of the one-tau analysis after the baseline event selection. All numbers are from MC with scale factors applied to top, W + jets and Z + jets except for the final estimate of QCD events, which is from section 5.8.5. The uncertainties are statistical only.

5.10 Systematic uncertainties

Systematic uncertainties play an important effect on the results of the analysis as they influence the estimated number of events in the SR. In this section a description of the sources of uncertainties and their treatment is presented and the effect they have on the result of the analysis can be found in table 5.8.

Each of the following uncertainty sources affects the properties of physics objects used in the analysis or the weight given to individual events. For each of these uncertainty sources the relevant MC objects are modified, e.g. the energy of jets lowered to account for uncertainty in the energy scale, and then the analysis repeats with these new objects. This also includes the SF determination as well as the full selection. The difference of this estimate to the nominal one is taken as the effect of the systematic.

5.10.1 Tau systematic uncertainties

The systematic uncertainties considered for taus in the analysis are the tau energy scale [49] and the tau identification efficiency. These systematic uncertainties are dependent on the p_{T} of the tau as well as the η range in which it is located. They also depend on the identification used. The evaluation of these systematic uncertainties was done by the ATLAS tau working group centrally for all analyses.

5.10.2 b-tagging systematic uncertainties

Systematic uncertainties due to b-jet identification are also considered, as these affect the uncertainty on the top and $\mathrm{W}+\mathrm{jets}$ SFs. For this uncertainty three components are considered, the uncertainty on the scale factor for b-jets and light jets as well light jet misidentification. A fourth source of uncertainty, the scale factor due to c-quarks was not considered, as it was found to be negligible in comparison.

5.10.3 Jet systematic uncertainties

For jets the systematic uncertainties considered are the uncertainty on the JES, as well as the Jet Energy Resolution (JER) [50]. The JER uncertainty is applied as an additional Gaussian smearing on the jet energy, making the energy resolution in MC match what is observed in data.

5.10.4 $E_{\mathrm{T}}^{\mathrm{miss}}$ systematic uncertainties

As the $E_{\mathrm{T}}^{\mathrm{miss}}$ is a composite quantity, the uncertaintes on all input terms have to be considered, see section 2.6. In the case of this analysis these are terms affecting the soft $E_{\mathrm{T}}^{\mathrm{miss}}$ terms as well as the jets. As with the

jet systematic uncertainties the soft energy systematic uncertainties include the uncertainty on the energy scale as well as the enery resolution. The tau systematic uncertainties need not be considered as they are not used in the $E_{\mathrm{T}}^{\mathrm{miss}}$ determination. When the variation is done the $E_{\mathrm{T}}^{\mathrm{miss}}$ needs to be recalculated taking the updated objects into account.

5.10.5 Other systematic uncertainties

Other uncertainties considered are due to the pileup reweighting procedure, additional uncertainties from generators for top and dibosons as well as from the methods used to estimate the background contributions in the SR. The pileup reweighting uncertainty is evaluated by making a 10% downwards scaling of the spectrum of number of interactions per event (μ). This is a common procedure used in the SUSY WG for the evaluation of this uncertainty and is found to be sufficient to cover the possible error due to the μ uncertainty.

The generator uncertainties studied cover the effect of the MC shape on the extrapolation from the CRs to SR. To study this settings of the generators used are varied; such as the renormalisation and factorisation scales. Due to the many different setting combinations that need to be checked to evaluate generator uncertainties these studies are done on generator level only. The assumption is that the differences seen at generator level will translate correctly to reconstruction level. As such, samples with different generator settings are produced and the effect of each on the final count is evaluated.

The final extra systematic uncertainty is due to the difference in the results on the true tau W SFs determined by the charge subtraction and matrix methods, outlined in 5.8.2 and 5.8.3 respectively. The difference is considered as an additional error on the true tau W SF itself.

5.10.6 Effects of uncertainties on the analysis

A complete summary of the uncertainties from statistics as well as systematic uncertainties can be found in table 5.8. This includes all evaluated uncertainties and their combination, taking into account the correlation between uncertainties where applicable.

5.11 Results

In table 5.9 the number of events passing the SR selection for each of the relevant MC samples as well as all uncertainties can be seen. These numbers are normalised to the luminosity found in the data. The total expected number of events is found to be $1.31 \pm 0.37^{\mathrm{stat}} \pm 0.65^{\mathrm{syst}}$, while 4 events are observed in the data. No statistically significant excess above the standard

Systematic	QCD	W + jets (true)	W + jets (fake)	Top (true)	Top (fake)	Z + jets	di-boson
JER	0.33	<0.002	1.1	-0.06	0.14	0.23	<0.002
JES ⇑	0.16	0.03	1.4	0.02	0.15	0.23	-0.33
JES ⇓	-0.09	-0.22	-0.90	-0.04	-0.10	<0.002	<0.002
TES ⇑	0.03	<0.002	0.07	-0.007	0.13	0.23	<0.002
TES ⇓	0.06	<0.002	0.20	-0.13	-0.10	<0.002	<0.002
Tau ID	0.07	0.06	-0.01	0.06	0.07	0.06	0.07
Pile-up	0.01	<0.002	0.20	-0.02	-0.05	<0.002	<0.002
STES ⇑	0.01	<0.002	<0.002	<0.002	<0.002	<0.002	<0.002
STES ⇓	-0.06	<0.002	<0.002	<0.002	<0.002	<0.002	<0.002
STR ⇑	0.04	<0.002	<0.002	<0.002	<0.002	<0.002	<0.002
STR ⇓	-0.01	<0.002	<0.002	<0.002	<0.002	<0.002	<0.002
Bjet ⇑	-0.02	0.05	0.33	-0.10	-0.08	0.02	<0.002
Bjet ⇓	0.04	-0.05	-0.07	0.09	0.08	-0.02	<0.002
Bjet (L) ⇑	0.01	-0.01	0.01	-0.02	-0.04	-0.004	-0.003
Bjet (L) ⇓	0.01	0.01	-0.06	-0.003	0.04	0.004	0.003
Method	0.50	0.21	—	—	—	—	—
Gen. DiBosons	—	<0.002	<0.002	<0.002	<0.002	0.05	0.04
Gen. $t\bar{t}$	—	—	—	0.15	0.15	—	—
Theory/Extr.	—	0.30	0.27	0.26	0.26	—	—
Total syst.	0.63	0.39	1.65	0.33	0.40	0.57	0.34
Stat.	0.21	0.70	1.13	0.38	0.81	1.0	—

Table 5.8: Overview of all systematic and statistical uncertainties for the one-tau channel. The uncertainties are presented in relative variations of the predicted number of background events. A statistical uncertainty is only listed for the channels which are found to contribute to the signal region.

model expectation is found. For comparison purposes the number of events accepted by the analysis in some selected signal points can be seen in table 5.10. These points are selected as they lie close to the border of expected exclusion limit.

The limits on the parameters of GMSB model are produced using the profile likelihood method [51] and the CL_S criterion [52]. The exclusion reach of this study at the 95% CL over the $\tan\beta$-Λ plane of the GMSB model (see section 5.2) is shown in figure 5.15. Models with $\Lambda < 45\,\text{TeV}$ (corresponding to gluino masses up to about 1000 GeV) for $40 > \tan\beta > 20$ are excluded. For lower values of $\tan\beta$ models with $\Lambda < 35\,\text{TeV}$ (gluino masses up to about 800 GeV) are excluded. As expected the exclusion is strongest for larger values of $\tan\beta$ where the stau is the NLSP. The results after the statistical combination with the two-tau, tau+muon and tau+electron channels, as well as the individual limits of each analysis are shown in figure 5.16. This leads to stronger exclusion of gluino masses up to about 1300 GeV for $40 > \tan\beta > 20$ and progressively worse for lower values, down to 1000 GeV. These results presented the best ATLAS limits for the GMSB model at the

top	$0.61 \pm 0.35^{\text{stat}} \pm 0.22^{\text{syst}}$
W + jets	$0.128 \pm 0.234^{\text{stat}} \pm 0.20^{\text{syst}}$
Z + jets	$0.22 \pm 0.22^{\text{stat}} \pm 0.13^{\text{syst}}$
QCD	$0.17 \pm 0.04^{\text{stat}} \pm 0.11^{\text{syst}}$
Drell-Yan	< 0.36
Diboson	< 0.05
Total	$1.31 \pm 0.37^{\text{stat}} \pm 0.65^{\text{syst}}$

Table 5.9: Number of expected event in the one-tau analysis SR from all contributing SM processes along with the statistical and systematic uncertainties. This leads to a final estimate of $1.31 \pm 0.37^{\text{stat}} \pm 0.65^{\text{syst}}$.

Λ	$\tan\beta$	Expected events	Stat. uncertainty	Cross section uncertainty	Syst. uncertainty
45	20	5.35	0.11	0.19	0.11
45	40	7.46	0.10	0.19	0.17
50	20	2.36	0.13	0.23	0.11
50	40	3.67	0.11	0.22	0.08
60	20	0.37	0.20	0.25	0.10
60	40	0.81	0.13	0.23	0.13

Table 5.10: Signal prediction and uncertainties in the one-tau analysis for six selected reference points from the GMSB grid around the expected exclusion contour. Λ values are in TeV. Uncertainties are relative.

time of publication.

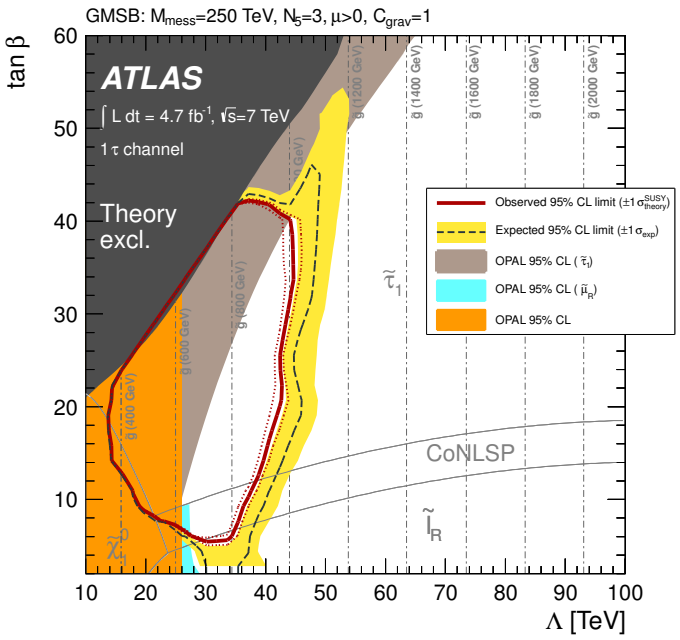

Figure 5.15: Exclusion contour of the one-tau analysis over the $\tan\beta - \Lambda$ parameter plane of the GMSB model. At the top of the plot the fixed parameters are displayed. The dashed vertical lines show the mass of gluinos in the model. The dark area corresponds to the region of parameter space excluded by theory, while the coloured regions correspond to the parameter space excluded by OPAL results.

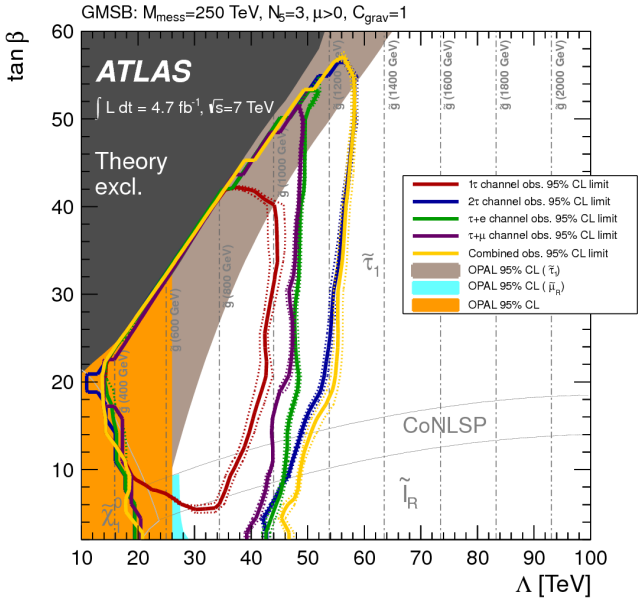

Figure 5.16: Exclusion contour of all channels in the analysis as well as the combined limit. The dashed vertical lines show the mass of gluinos in the model. The dark area corresponds to the region of parameter space excluded by theory, while the coloured regions correspond to the parameter space excluded by OPAL results.

Chapter 6

Conclusions

The work presented in the thesis covers many different levels of results from the ATLAS experiment at the LHC, each of them important to the working of the experiment and its physics goals.

The Inner Detector Global monitoring package was used throughout Run I to spot issues in the detector as they arose. The input from this package was important for checking the performance of the Inner Detector and excluding problematic data from physics analyses. All data in Run I passed through this monitoring and it forms part of the basis for monitoring the ID in Run II, the preparations for which have already started.

The measurements of minimum bias event spectra were crucial in enabling the tuning of MC generators as well as getting a better understanding of the type of event that form the pileup in the detector. These two factors are vital for making searches for new physics possible even under the effects of very high pileup during the increased luminosity at the end of Run I.

Chapter 5 presented a search for supersymmetry using events with tau leptons performed on the full 2011 dataset, comprising 4.7 fb recorded at 7 TeV CoM energy. No signal above the Standard Model expectation was observed. The result was used to set limits on the GMSB model parameters which translates to lower limits on the sparticle masses. A followup paper was produced presenting the analysis of the full 2012 8 TeV dataset of 20.1 fb. This search included additional interpretations; the mSUGRA, nGM and bRPV models. SUSY is still a hypothetical model after Run I, no experiment has as of yet evidence of supersymmetry.

As run I has come to its end the focus has shifted towards Run II of the LHC. This will not only bring an increase in CoM energy to 13 TeV, but also an increase in luminosity, with 100 fb^{-1} of data expected. This means a far greater physics reach but also challenges in understanding the detector. Run II is expected to start in Spring 2015.

Appendix A

List of samples considered in the SUSY study

A list of all the samples considered in the study presented, along with their identification number for ATLAS and their cross-section and number of events present in the samples.

Sample ID	Name	Generator	NNLO [pb]	No. of events
105200	$t\bar{t}$ semileptonic (T1)	MCAtNLOJimmy	90.57	14983835
105204	$t\bar{t}$ full hadronic	MCAtNLOJimmy	76.23	1199034
117360	t-channel $t \to e\nu$	AcerMCPythia	6.97	999295
117361	t-channel $t \to \mu\nu$	AcerMCPythia	6.97	999948
117362	t-channel $t \to \tau\nu$	AcerMCPythia	6.97	998995
108343	s-channel $t \to e\nu$	MCAtNLOJimmy	0.50	299948
108344	s-channel $t \to \mu\nu$	MCAtNLOJimmy	0.50	299998
108345	s-channel $t \to \tau\nu$	MCAtNLOJimmy	0.50	299899
108346	single top Wt	MCAtNLOJimmy	15.74	899694

Table A.1: Used $t\bar{t}$ and single t MC samples with their corresponding sample ID, event generator, NLO cross section and number of generated events.

Sample ID	Name	Generator	NNLO [pb]	# events
107680	WenuNp0	AlpgenJimmy	8288.88	3458883
107681	WenuNp1	AlpgenJimmy	1561.14	2499645
107682	WenuNp2	AlpgenJimmy	452.24	3768632
107683	WenuNp3	AlpgenJimmy	121.82	1008947
107684	WenuNp4	AlpgenJimmy	30.71	250000
107685	WenuNp5	AlpgenJimmy	8.36	69999
144022	WenuNp6_pt20	AlpgenJimmy	1.85	145000
144196	WenuNp1_susyfilt	AlpgenJimmy	8.83	180899
144197	WenuNp2_susyfilt	AlpgenJimmy	7.47	134998
144198	WenuNp3_susyfilt	AlpgenJimmy	4.15	139999
144199	WenuNp4_susyfilt	AlpgenJimmy	1.73	75000
107690	WmunuNp0	AlpgenJimmy	8284.22	3462942
107691	WmunuNp1	AlpgenJimmy	1560.55	2498593
107692	WmunuNp2	AlpgenJimmy	451.79	3768737
107693	WmunuNp3	AlpgenJimmy	121.71	1008446
107694	WmunuNp4	AlpgenJimmy	30.74	254950
107695	WmunuNp5	AlpgenJimmy	8.37	70000
144023	WmunuNp6_pt20	AlpgenJimmy	1.85	145000
144200	WmunuNp1_susyfilt	AlpgenJimmy	8.46	171000
144201	WmunuNp2_susyfilt	AlpgenJimmy	7.34	139900
144202	WmunuNp3_susyfilt	AlpgenJimmy	4.09	139899
144203	WmunuNp4_susyfilt	AlpgenJimmy	1.73	70000
107700	WtaunuNp0	AlpgenJimmy	8283.50	3418296
107701	WtaunuNp1	AlpgenJimmy	1559.36	2499194
107702	WtaunuNp2	AlpgenJimmy	451.63	3750986
107703	WtaunuNp3	AlpgenJimmy	121.84	1009946
107704	WtaunuNp4	AlpgenJimmy	30.72	249998
107705	WtaunuNp5	AlpgenJimmy	8.37	65000
144024	WtaunuNp6_pt20	AlpgenJimmy	1.85	150000
144204	WtaunuNp1_susyfilt	AlpgenJimmy	13.08	265000
144205	WtaunuNp2_susyfilt	AlpgenJimmy	11.06	204999
144206	WtaunuNp3_susyfilt	AlpgenJimmy	6.09	209900
144207	WtaunuNp4_susyfilt	AlpgenJimmy	2.52	104999

Table A.2: Used W + jets MC samples with their corresponding sample ID, event generator, LO cross section, and section, k-factor, NNLO cross section and number of generated events. Samples marked "susyfilt" have been produced with a truth level filter requiring one jet of at least 100 GeV p_{T} and at least 100 GeV of missing transverse energy.

Sample ID	Name	Generator	NNLO [pb]	# events
107650	ZeeN0p	AlpgenJimmy	832.61	6618284
107651	ZeeN1p	AlpgenJimmy	167.31	1334897
107652	ZeeN2p	AlpgenJimmy	50.55	2004195
107653	ZeeN3p	AlpgenJimmy	14.00	549949
107654	ZeeN4p	AlpgenJimmy	3.53	149948
107655	ZeeN5p	AlpgenJimmy	0.95	50000
107660	ZmumuN0p	AlpgenJimmy	832.61	6615230
107661	ZmumuN1p	AlpgenJimmy	167.31	1334296
107662	ZmumuN2p	AlpgenJimmy	50.55	1999941
107663	ZmumuN3p	AlpgenJimmy	14.00	549896
107664	ZmumuN4p	AlpgenJimmy	3.53	150000
107665	ZmumuN5p	AlpgenJimmy	0.95	50000
107670	ZtautauN0p	AlpgenJimmy	832.61	10613179
107671	ZtautauN1p	AlpgenJimmy	167.31	3334137
107672	ZtautauN2p	AlpgenJimmy	50.55	1004847
107673	ZtautauN3p	AlpgenJimmy	14.00	509847
107674	ZtautauN4p	AlpgenJimmy	3.53	144999
107675	ZtautauN5p	AlpgenJimmy	0.95	45000
107710	ZnunuNp0	AlpgenJimmy	49.93	54949
107711	ZnunuNp1	AlpgenJimmy	569.09	909848
107712	ZnunuNp2	AlpgenJimmy	247.68	169899
107713	ZnunuNp3	AlpgenJimmy	75.45	144999
107714	ZnunuNp4	AlpgenJimmy	19.55	309899
107715	ZnunuNp5	AlpgenJimmy	5.42	189998

Table A.3: Used Z + jets MC samples with their corresponding sample ID, event generator, LO cross section, k-factor, NNLO cross section, and number of generated events.

Sample ID	Generator	Final state	NLO [pb]	No. of events
105921	McAtNlo_JIMMY	$W^{\pm} \to e\nu e\nu$	0.51	199949
105922	McAtNlo_JIMMY	$W^{\pm} \to e\nu\mu\nu$	0.51	200000
105923	McAtNlo_JIMMY	$W^{\pm} \to e\nu\tau\nu$	0.51	200000
105924	McAtNlo_JIMMY	$W^{\pm} \to \mu\nu\mu\nu$	0.51	199000
105925	McAtNlo_JIMMY	$W^{\pm} \to \mu\nu e\nu$	0.51	199949
105926	McAtNlo_JIMMY	$W^{\pm} \to \mu\nu\tau\nu$	0.51	200000
105927	McAtNlo_JIMMY	$W^{\pm} \to \tau\nu\tau\nu$	0.51	499676
105928	McAtNlo_JIMMY	$W^{\pm} \to \tau\nu e\nu$	0.51	199950
105929	McAtNlo_JIMMY	$W^{\pm} \to \tau\nu\mu\nu$	0.51	200000
105930	McAtNlo_JIMMY	$ZZ \to \ell\ell q\bar{q}$	0.270	25000
105931	McAtNlo_JIMMY	$ZZ \to \ell\ell\ell\ell$	0.026	99999
105932	McAtNlo_JIMMY	$ZZ \to \ell\ell\nu\nu$	0.077	99999
106036	McAtNlo_JIMMY	$ZZ \to 2\ell 2\tau$	1.695	25000
106037	McAtNlo_JIMMY	$ZZ \to 4\tau$	0.164	25000
113192	McAtNlo_JIMMY	$ZZ \to \tau\tau\nu\nu$	0.514	24950
113193	McAtNlo_JIMMY	$ZZ \to \tau\tau q\bar{q}$	0.928	25000
105940	McAtNlo_JIMMY	$W^{+}Z \to \ell\nu q\bar{q}$	0.090	100000
105941	McAtNlo_JIMMY	$W^{+}Z \to \ell\nu\ell\ell$	0.28	100000
105942	McAtNlo_JIMMY	$W^{+}Z \to q\bar{q}'\ell\ell$	0.086	25000
106024	McAtNlo_JIMMY	$W^{+}Z \to \tau\nu\ell\ell$	0.082	25000
106025	McAtNlo_JIMMY	$W^{+}Z \to \ell\nu\tau\tau$	0.043	199950
106026	McAtNlo_JIMMY	$W^{+}Z \to \tau\nu\tau\tau$	0.047	25000
113190	McAtNlo_JIMMY	$W^{+}Z \to q\bar{q}'\tau\tau$	0.045	25000
105970	McAtNlo_JIMMY	$W^{-}Z \to \ell\nu q\bar{q}$	0.0234	200000
105971	McAtNlo_JIMMY	$W^{-}Z \to \ell\nu\ell\ell$	0.0129	25000
105972	McAtNlo_JIMMY	$W^{-}Z \to q\bar{q}'\ell\ell$	0.0065	25000
106027	McAtNlo_JIMMY	$W^{-}Z \to \tau\nu\ell\ell$	0.2568	199949
106028	McAtNlo_JIMMY	$W^{-}Z \to \ell\nu\tau\tau$	0.1397	200000
106029	McAtNlo_JIMMY	$W^{-}Z \to \tau\nu\tau\tau$	0.0386	200000
113191	McAtNlo_JIMMY	$W^{-}Z \to q\bar{q}'\tau\tau$	0.1348	199950

Table A.4: Used diboson MC samples with their corresponding sample ID, event generator, final state, NLO cross section, and number of generated events.

Sample ID	Name	Generator	LO [pb]	No. of events
105009	J0	Pythia	12030000000	999997
105010	J1	Pythia	807266000	999993
105011	J2	Pythia	48048000	999999
105012	J3	Pythia	2192900	999992
105013	J4	Pythia	87701	989992
105014	J5	Pythia	2350.1	999987
105015	J6	Pythia	33.61	999974
105016	J7	Pythia	0.13744	998955
105017	J8	Pythia	0.000006	998948

Table A.5: Used dijet MC samples with their corresponding sample ID, event generator, cross section and number of generated events.

Sample ID	Name	Generator	NNLO [pb]	# events
116250	ZeeNp0Mll10to40	AlpgenJimmy	3798.37	994949
116251	ZeeNp1Mll10to40	AlpgenJimmy	105.58	299998
116252	ZeeNp2Mll10to40	AlpgenJimmy	51.22	999946
116253	ZeeNp3Mll10to40	AlpgenJimmy	10.38	149998
116254	ZeeNp4Mll10to40	AlpgenJimmy	2.30	40000
116255	ZeeNp5Mll10to40	AlpgenJimmy	0.57	10000
116260	ZmumuNp0Mll10to40	AlpgenJimmy	3798.62	999849
116261	ZmumuNp1Mll10to40	AlpgenJimmy	105.42	300000
116262	ZmumuNp2Mll10to40	AlpgenJimmy	51.14	999995
116263	ZmumuNp3Mll10to40	AlpgenJimmy	10.37	150000
116264	ZmumuNp4Mll10to40	AlpgenJimmy	2.33	39999
116265	ZmumuNp5Mll10to40	AlpgenJimmy	0.57	10000
116270	ZtautauNp0Mll10to40	AlpgenJimmy	3798.49	999649
116271	ZtautauNp1Mll10to40	AlpgenJimmy	105.54	299999
116272	ZtautauNp2Mll10to40	AlpgenJimmy	51.33	498899
116273	ZtautauNp3Mll10to40	AlpgenJimmy	10.38	150000
116274	ZtautauNp4Mll10to40	AlpgenJimmy	2.28	39999
116275	ZtautauNp5Mll10to40	AlpgenJimmy	0.57	10000

Table A.6: Used Drell-Yan MC samples with their corresponding sample ID, event generator, LO cross section, k-factor, NNLO cross section and number of generated events.

Sample	Λ [TeV]	$\tan\beta$	σ [pb]
137915	10	2	552.595
137916	10	5	552.996
137917	10	10	552.960
137918	10	15	552.166
137919	10	20	661.116
137920	10	21	659.621
143061	12	21	312.079
143055	15	2	106.275
143056	15	5	109.792
143057	15	10	102.78
143058	15	15	100.390
143059	15	20	99.823
143060	15	23	100.555
137921	20	2	21.666
137922	20	5	22.427
137923	20	10	21.964
137924	20	15	21.795
137925	20	20	21.846
137926	20	27	22.994
137927	30	2	2.212
137928	30	5	2.344
137929	30	10	2.339
137930	30	15	2.337
137931	30	20	2.346
137932	30	30	2.458
137933	30	36	3.207
142558	35	2	0.882
142559	35	5	0.951
142560	35	10	0.956
142561	35	15	0.958
142562	35	20	0.963
142563	35	25	0.974
142564	35	30	1.000
142565	35	35	1.073
142566	35	40	1.546
142567	35	42	2.962
137934	40	2	0.389
137935	40	5	0.427
137936	40	10	0.433
137937	40	15	0.434
137938	40	20	0.436
137939	40	25	0.442
137940	40	30	0.452
137941	40	36	0.484
137942	40	40	0.546
137943	40	46	1.814
142568	45	2	0.184
142569	45	5	0.208
142570	45	10	0.213
142571	45	15	0.214
142572	45	20	0.215
142573	45	25	0.218
142574	45	30	0.223
142575	45	35	0.233
142576	45	40	0.256
142577	45	50	1.327
137944	50	2	0.093
137945	50	5	0.109
137946	50	10	0.112
137947	50	15	0.113
137948	50	20	0.114
137949	50	30	0.118
137950	50	40	0.133
137951	50	50	0.248
137952	60	2	0.028
137953	60	5	0.035
137954	60	10	0.037
137955	60	15	0.038
137956	60	20	0.038
137957	60	30	0.040
137958	60	40	0.044
137959	60	50	0.060
137960	70	2	0.011
137961	70	5	0.014
137962	70	10	0.015
137963	70	15	0.015
137964	70	20	0.016
137965	70	30	0.016
137966	70	40	0.018
137967	70	50	0.022
137968	80	2	0.0046
137969	80	5	0.0063
137970	80	10	0.0070
137971	80	15	0.0072
137972	80	20	0.0073
137973	80	30	0.0076
137974	80	40	0.0084
137975	80	50	0.0101

Table A.7: List of MC samples for SUSY signal. All samples are generated using Herwig++. Four out of six parameters defining the GMSB points are the same for all samples: $M_{\text{mess}} = 250$ TeV, $N_5 = 3$, sign(μ) = +, and C_{grav}. The parameters Λ and $\tan\beta$ are varied as shown in the table.

Appendix B

Event displays from Supersymmetry analysis

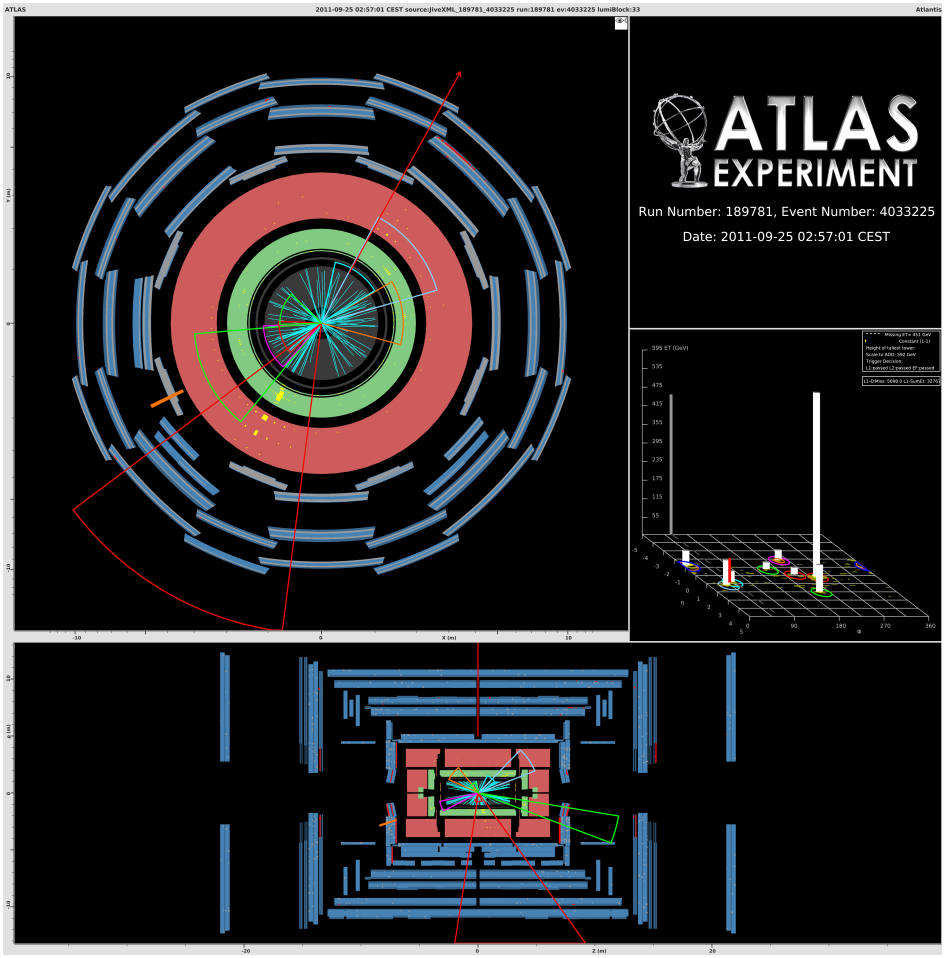

Figure B.1: Event selected in the SR of the supersymmetry with taus analysis. The $p_{mathrmT}$ of the leading and sub-leading jets are 592 GeV (red) and 86 GeV (green) respectively. The selected tau p_{T} is 32 GeV (orange spike in prolongation of jet axis). $E_{\mathrm{T}}^{\mathrm{miss}}$ is 478 GeV (red arrow).

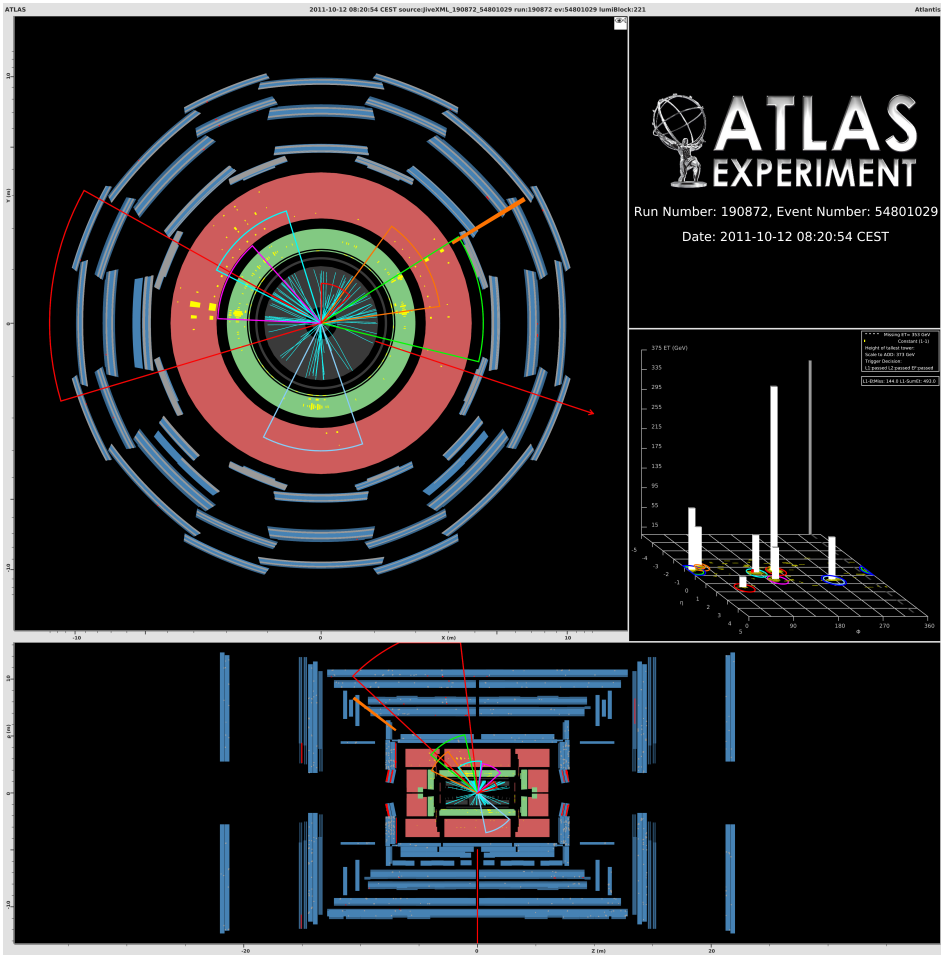

Figure B.2: Event selected in the SR of the supersymmetry with taus analysis. The $p_{mathrmT}$ of the leading and sub-leading jets are 372 GeV (red) and 124 GeV (green) respectively. The selected tau p_{T} is 66 GeV (orange spike in prolongation of jet axis). $E_{\mathrm{T}}^{\mathrm{miss}}$ is 324 GeV (red arrow).

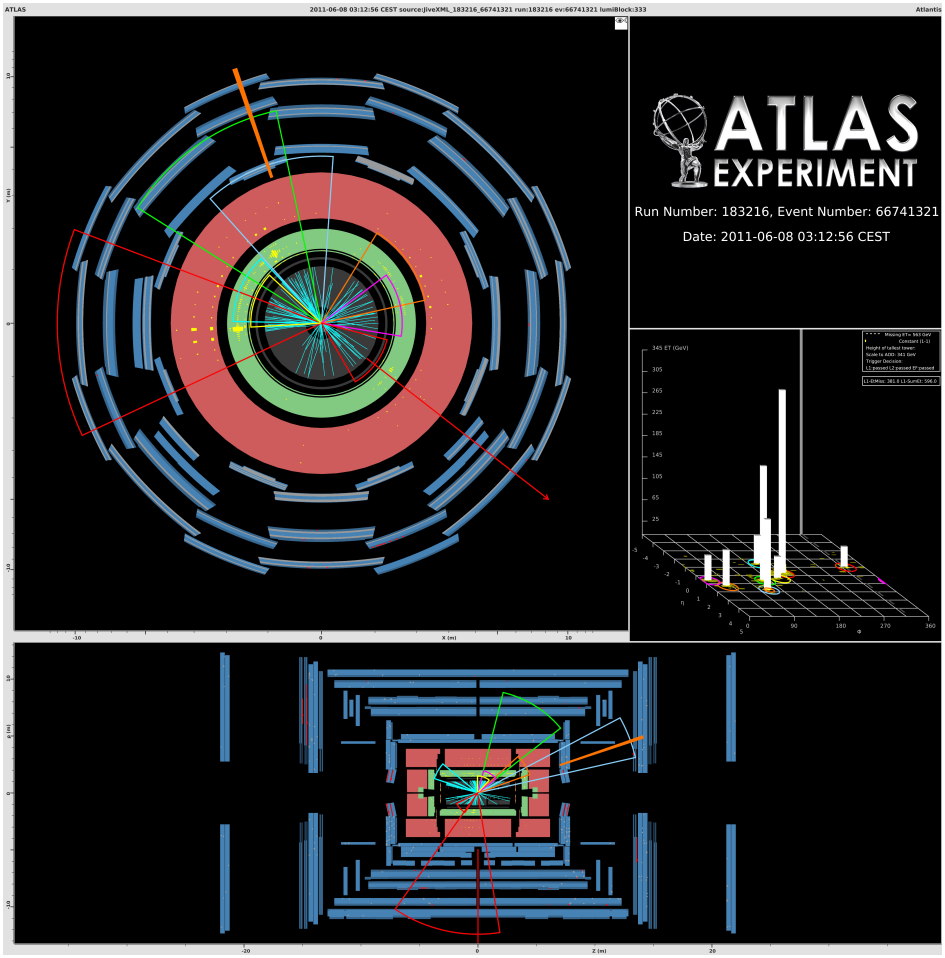

Figure B.3: Event selected in the SR of the supersymmetry with taus analysis. The $p_{mathrmT}$ of the leading and sub-leading jets are 341 GeV (red) and 212 GeV (green) respectively. The selected tau p_{T} is 109 GeV (orange spike in prolongation of jet axis). $E_{\mathrm{T}}^{\mathrm{miss}}$ is 507 GeV (red arrow).

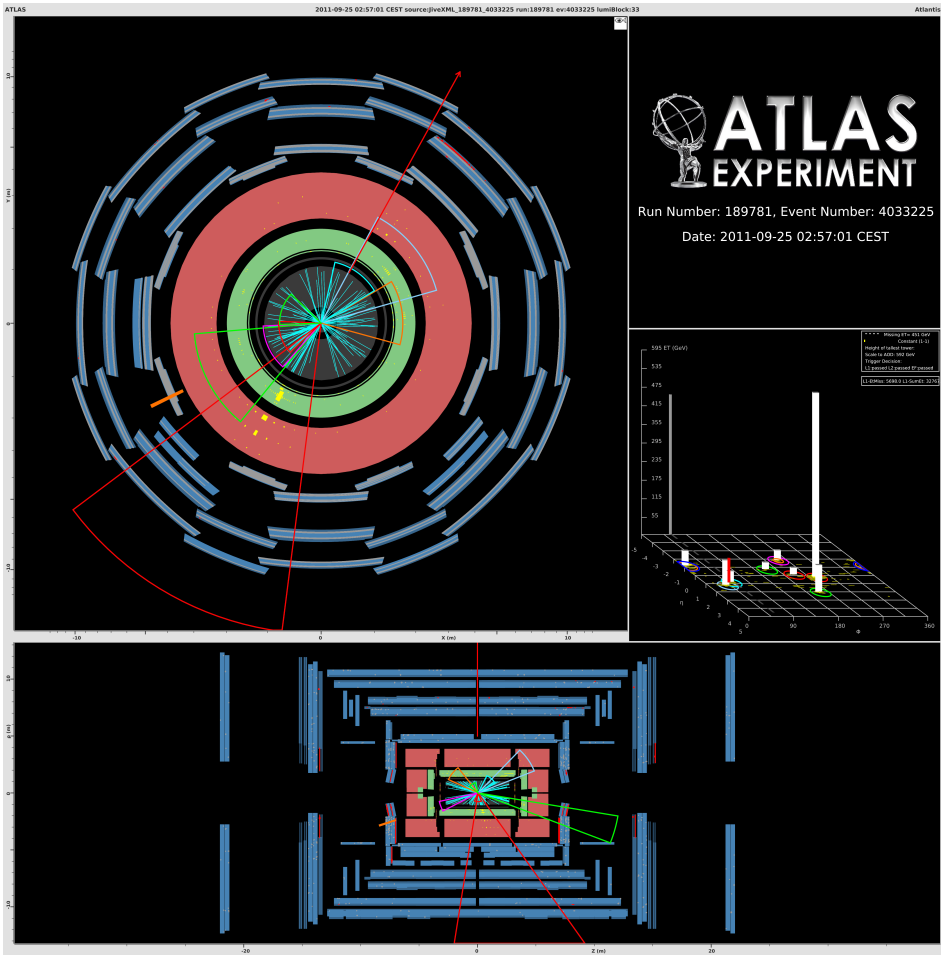

Figure B.4: Event selected in the SR of the supersymmetry with taus analysis. The $p_{mathrmT}$ of the leading and sub-leading jets are 386 GeV (red) and 188 GeV (green) respectively. The selected tau p_{T} is 266 GeV (orange spike in prolongation of jet axis). $E_{\mathrm{T}}^{\mathrm{miss}}$ is 300 GeV (red arrow).

Bibliography

[1] ATLAS Collaboration. Search for Supersymmetry in Events with Large Missing Transverse Momentum, Jets, and at Least One Tau Lepton in 21 fb^{-1} of $\sqrt{s} = 8$ TeV Proton-Proton Collision Data with the ATLAS Detector. Technical Report ATLAS-CONF-2013-026, CERN, Geneva, Mar 2013.

[2] ATLAS Collaboration. Search for supersymmetry in events with large missing transverse momentum, jets, and at least one tau lepton in 20 fb^{-1} of $\sqrt{s} = 8$ tev proton-proton collision data with the atlas detector. *Journal of High Energy Physics*, 2014(9), 2014.

[3] ATLAS Collaboration. The ATLAS Experiment at the CERN Large Hadron Collider. *Journal of Instrumentation*, 3(08):S08003, 2008.

[4] O. S. Brüning et al. *LHC Design Report*. CERN, Geneva, 2004.

[5] Picture courtesy of CERN.

[6] J. J. Goodson. Search for supersymmetry in states with large missing transverse momentum and three leptons including a z-boson. May 2012. Presented 17 Apr 2012.

[7] T. Cornelissen et al. Concepts, Design and Implementation of the ATLAS New Tracking (NEWT). Technical Report ATL-SOFT-PUB-2007-007, CERN, Geneva, Mar 2007.

[8] ATLAS Collaboration. Performance of the ATLAS Inner Detector Track and Vertex Reconstruction in the High Pile-Up LHC Environment. Technical Report ATLAS-CONF-2012-042, CERN, Geneva, Mar 2012.

[9] Performance of primary vertex reconstruction in proton-proton collisions at $\sqrt{s}$ =7 TeV in the ATLAS experiment. Technical Report ATLAS-CONF-2010-069, CERN, Geneva, Jul 2010.

[10] Gavin P. Salam. Towards Jetography. *European Physical Journal C*, 67:637, 2010. 88 pages, 27 figures, an extended version of lectures given at the CTEQ/MCNET school, Debrecen, Hungary, August 2008.

[11] ATLAS Collaboration. Jet energy measurement with the ATLAS detector in proton-proton collisions at $\sqrt{s} = 7$ TeV. *Eur.Phys.J.*, C73:2304, 2013.

[12] ATLAS Collaboration. Commissioning of the ATLAS high-performance b-tagging algorithms in the 7 TeV collision data. Technical Report ATLAS-CONF-2011-102, CERN, Geneva, Jul 2011.

[13] G. Piacquadio and C. Weiser. A new inclusive secondary vertex algorithm for b-jet tagging in atlas. *Journal of Physics: Conference Series*, 119(3):032032, 2008.

[14] Particle Data Group. Review of particle physics. *Phys. Rev. D*, 86:010001, Jul 2012.

[15] ATLAS Collaboration. Performance of the Reconstruction and Identification of Hadronic Tau Decays in ATLAS with 2011 Data. Technical Report ATLAS-CONF-2012-142, CERN, Geneva, Oct 2012.

[16] ATLAS Collaboration. Performance of Missing Transverse Momentum Reconstruction in Proton-Proton Collisions at 7 TeV with ATLAS. *Eur.Phys.J.*, C72:1844, 2012.

[17] R. Brun and F. Rademakers. Root - an object oriented data analysis framework. pages 81–86, September 1996.

[18] P. Adragna A. Dotti and R. A. Vitillo. The Online Histogram Presenter for the ATLAS experiment: a modular system for histogram visualization. Technical Report ATL-DAQ-PUB-2009-009, CERN, Geneva, Sep 2009.

[19] Y. Ilchenko et al. Data Quality Monitoring Display for ATLAS experiment. May 2009. Poster at CHEP 2009 conference.

[20] J. Adelman et al. ATLAS offline data quality monitoring. *Journal of Physics: Conference Series*, 219(4):042018, 2010.

[21] ATLAS Collaboration. Characterization of Interaction-Point Beam Parameters Using the pp Event-Vertex Distribution Reconstructed in the ATLAS Detector at the LHC. Technical Report ATLAS-CONF-2010-027, CERN, Geneva, May 2010.

[22] T. Golling et al. The ATLAS Data Quality Defect Database System. *Eur.Phys.J.*, C72:1960, 2012.

[23] ATLAS Collaboration. Charged-particle multiplicities in pp interactions measured with the atlas detector at the lhc. *New J. Phys.*, 13(arXiv:1012.5104. CERN-PH-EP-2010-079):053033. 70 p, Dec 2010.

Comments: 57 pages plus author list (82 pages total), 19 figures (85 independent .eps files), 10 tables.

[24] G. D'Agostini. A multidimensional unfolding method based on Bayes' theorem. *Nucl. Instr. Meth. in Physics Research Section A*, 362(2–3):487 – 498, 1995.

[25] ATLAS Collaboration. Charged particle multiplicities in p p interactions at $\sqrt{s} = 0.9$ and 7 TeV in a diffractive limited phase-space measured with the ATLAS detector at the LHC and new PYTHIA6 tune. Technical Report ATLAS-CONF-2010-031, CERN, Geneva, Jul 2010.

[26] R. Engel F. W. Bopp and J. Ranft. Rapidity gaps and the PHOJET Monte Carlo. pages 729–741, 1998.

[27] H. Miyazawa. Baryon Number Changing Currents. *Prog. Theor. Phys.*, 36 (6):1266–1276, 1966.

[28] S. Dimopoulos and H. Georgi. Softly Broken Supersymmetry and SU(5). *Nucl. Phys.*, B193:150, 1981.

[29] H. Goldberg. Constraint on the photino mass from cosmology. *Phys. Rev. Lett.*, 50:1419, 1983.

[30] J.R. Ellis, J.S. Hagelin, D.V. Nanopoulos, K.A. Olive, and M. Srednicki. Supersymmetric relics from the big bang. *Nucl. Phys.*, B238:453–476, 1984.

[31] S. Dimopoulos, S. Raby, and Frank Wilczek. Supersymmetry and the Scale of Unification. *Phys. Rev.*, D24:1681–1683, 1981.

[32] Michael Dine and Willy Fischler. A Phenomenological Model of Particle Physics Based on Supersymmetry. *Phys. Lett.*, B110:227, 1982.

[33] Luis Alvarez-Gaume, Mark Claudson, and Mark B. Wise. Low-Energy Supersymmetry. *Nucl. Phys.*, B207:96, 1982.

[34] Chiara R. Nappi and Burt A. Ovrut. Supersymmetric Extension of the SU(3) x SU(2) x U(1) Model. *Phys. Lett.*, B113:175, 1982.

[35] Michael Dine and Ann E. Nelson. Dynamical supersymmetry breaking at low-energies. *Phys. Rev.*, D48:1277–1287, 1993.

[36] Michael Dine, Ann E. Nelson, and Yuri Shirman. Low-energy dynamical supersymmetry breaking simplified. *Phys. Rev.*, D51:1362–1370, 1995.

[37] Michael Dine, Ann E. Nelson, Yosef Nir, and Yuri Shirman. New tools for low-energy dynamical supersymmetry breaking. *Phys. Rev.*, D53:2658–2669, 1996.

[38] G. Abbiendi et al. Search for chargino and neutralino production at $\sqrt{s}$ = 192 GeV to 209 GeV at LEP. *Eur.Phys.J.*, C35:1–20, 2004.

[39] ATLAS Collaboration. Expected performance of the ATLAS detector in GMSB models with tau final states. Technical Report ATL-PHYS-PUB-2009-089, CERN, Geneva, Nov 2009.

[40] Andy Buckley. PySLHA. `http://www.insectnation.org/projects/pyslha`. Accessed: 2012-08-20.

[41] S. Frixione and B. R. Webber. Matching NLO QCD computations and parton shower simulations. *JHEP*, 06:029, 2002.

[42] G. Corcella et al. HERWIG 6: An event generator for hadron emission reactions with interfering gluons (including supersymmetric processes). *JHEP*, 0101:010, 2001.

[43] B. P. Kersevan and E. Richter-Was. The Monte Carlo event generator AcerMC version 2.0 with interfaces to PYTHIA 6.2 and HERWIG 6.5. 2004.

[44] S. Mrenna T. Sjostrand and P. Z. Skands. PYTHIA 6.4 Physics and Manual. *JHEP*, 0605:026, 2006.

[45] M. L. Mangano et al. ALPGEN, a generator for hard multiparton processes in hadronic collisions. *JHEP*, 0307:001, 2003.

[46] J. R. Forshaw J. M. Butterworth and M. H. Seymour. Multiparton interactions in photoproduction at HERA. *Z.Phys.*, C72:637–646, 1996.

[47] S. D. Protopopescu H. Baer, F. E. Paige and X. Tata. ISAJET 7.48: A Monte Carlo event generator for p p, anti-p, p, and e+ e- reactions. 1999.

[48] ATLAS Collaboration. Selection of jets produced in proton-proton collisions with the ATLAS detector using 2011 data. Technical Report ATLAS-CONF-2012-020, CERN, Geneva, Mar 2012.

[49] Determination of the tau energy scale and the associated systematic uncertainty in proton-proton collisions at sqrts = 7 TeV with the ATLAS detector at the LHC in 2011. Technical Report ATLAS-CONF-2012-054, CERN, Geneva, Jun 2012.

[50] Jet energy scale and its systematic uncertainty in proton-proton collisions at sqrt(s)=7 TeV with ATLAS 2011 data. Technical Report ATLAS-CONF-2013-004, CERN, Geneva, Jan 2013.

[51] Glen Cowan, Kyle Cranmer, Eilam Gross, and Ofer Vitells. Asymptotic formulae for likelihood-based tests of new physics. *Eur.Phys.J.*, C71:1554, 2011.

[52] A. L. Read. Presentation of search results: the cl s technique. *Journal of Physics G: Nuclear and Particle Physics*, 28(10):2693, 2002.

Acronyms

AOD Analysis Object Data . . . 21
ATLAS A Toroidal LHC ApparatuS
BCID Bunch Crossing IDentification . . . 25
BDT Boosted Desicion Tree . . . 17
CP Combined Performance . . . 39
CR Control Region . . . 67
CSC Cathode Strip Chambers . . . 11
CoM Center of Mass . . . 1
DAQ Data AQuisition . . . 20
DB DataBase . . . 29
DM Dark Matter . . . 59
DQ Data Quality . . . 23
EF Event Filter . . . 19
EMES Electro-Magnetic Energy Scale . . . 11
ESD Event Summary Data . . . 21
fCal Forward Calorimeter . . . 8
GMSB Gauge Mediated Symmetry Breaking . . . 59
GRL Good Run List . . . 36
HEC Hadronic Endcap Calorimeter . . . 8
HLT High Level Trigger . . . 19
ID Inner Detector . . . 4
IP Impact Parameter . . . 17
JER Jet Energy Resolution . . . 82
JES Jet Energy Scale . . . 11
L1 Level one . . . 12
L2 Level two . . . 19

LAr	Liquid Argon Calorimeter . . . 8
LB	Luminosity Block . . . 21
LEP	Large Electron Positron Collider . . . 3
LHC	Large Hadron Collider . . . 1
LSP	Lightest Supersymmetric Particle . . . 60
MBTS	Minimum Bias Trigger Scintillator . . . 20
MC	Monte Carlo . . . 44
MDT	Monitored Drift Tubes . . . 11
MSSM	Minimal Supersymmetric Standard Model . . . 59
MS	Muon Spectrometer
NLSP	Next-to-Lightest Supersymmetric Particle . . . 60
P1	Point 1 . . . 38
PMT	PhotoMultiplier Tube . . . 10
QCD	Quantum Chromodynamics . . . 11
ROD	Read Out Driver . . . 24
RPC	Resistive Plate Chambers . . . 11
SCT	SemiConductor Tracker . . . 6
SF	Scale Factor . . . 67
SM	Standard Model . . . 1
SR	Signal Region . . . 62
SUSY	Supersymmetry . . . 13
TES	Tau Energy Scale . . . 16
TGC	Thin Gap Chambers . . . 11
TRT	Transition Radiation Tracker . . . 6
VEV	Vacuum Expectation Value . . . 60

List of Figures

List of Tables